JAEA-Research
2008-100

JAEA-Research

Design Study of 500 keV H^- Accelerator for ITER NB System

Mieko KASHIWAGI and Takashi INOUE

Plasma Heating Technology Group
Fusion Research and Development Directorate

February 2009

Japan Atomic Energy Agency

日本原子力研究開発機構

本レポートは独立行政法人日本原子力研究開発機構が不定期に発行する成果報告書です。
本レポートの入手並びに著作権利用に関するお問い合わせは、下記あてにお問い合わせ下さい。
なお、本レポートの全文は日本原子力研究開発機構ホームページ（http://www.jaea.go.jp）
より発信されています。

独立行政法人日本原子力研究開発機構　研究技術情報部　研究技術情報課
〒319-1195　茨城県那珂郡東海村白方白根 2 番地 4
電話 029-282-6387, Fax 029-282-5920, E-mail:ird-support@jaea.go.jp

This report is issued irregularly by Japan Atomic Energy Agency
Inquiries about availability and/or copyright of this report should be addressed to
Intellectual Resources Section, Intellectual Resources Department,
Japan Atomic Energy Agency
2-4 Shirakata Shirane, Tokai-mura, Naka-gun, Ibaraki-ken 319-1195 Japan
Tel +81-29-282-6387, Fax +81-29-282-5920, E-mail:ird-support@jaea.go.jp

JAEA-Research 2008-100

Design Study of 500 keV H^- Accelerator for ITER NB System

Mieko KASHIWAGI and Takashi INOUE

Division of Fusion Energy Technology
Fusion Research and Development Directorate
Japan Atomic Energy Agency
Naka-shi, Ibaraki-ken

(Received December 8, 2008)

In the neutral beam (NB) system for heating and current drive of ITER, detailed designs of a five stage Multi Aperture and Multi Grid (MAMuG) accelerator to produce 1 MeV 40 A D^- and 870 keV 46 A H^- ion beams are ongoing. However, it was expected that shinethrough power from the 870 keV H^0 beam was above tolerable level for the maximum plasma density prior to any H mode. Therefore, it was required to reduce the beam energy to 500 keV with maintaining high beam current. The objective of this study is to identify necessary modifications from the original five stage accelerator to a three stage accelerator to produce 500 keV H^- ion beam through the physics design based on a beam optics, a beamlet steering and a stripping loss of negative ions. In the beam optics study utilizing a 2D beam analysis code, necessary modifications in aperture diameter, grid thickness and grid spacing were proposed. In a 3D multi beamlets analysis, aperture offsets in the ESG (Electron Suppression Grid) to compensate beamlet deflections and another aperture offset in the GRG (GRounded Grid) to steer the beamlets to a focal point were designed. In a 3D gas flow analysis, it was confirmed that stripping loss of negative ions was not changed and gas density around the beam source satisfied a design requirement for high voltage holding in a modified accelerator configuration proposed in the beam optics study. Finally, the items for modification were summarized.

Keywords: Neutral Beam Injection, Negative Ion Accelerator, Beamlet Steering

ITER用中性粒子入射加熱装置に向けた500 keV水素負イオン加速器設計

日本原子力研究開発機構
核融合研究開発部門　核融合エネルギー工学研究開発ユニット
柏木　美恵子、井上　多加志

(2008年12月 8日　受理)

ITERの加熱・電流駆動に用いられる中性粒子入射（NB）装置では、1 MeV、 40 Aの重水素負イオン（D^-）、または870 keV、 46 Aの水素負イオン（H^-）のイオンビームを生成する多孔多段の５段加速器の設計が進められてきた。しかし、ITER運転初期の低密度水素プラズマに対してはビームの突き抜けが予想されるため、ビームエネルギーを500 keVに下げつつ大電流のH^-イオンビームを生成する加速器の検討が必要となった。本研究の目的は、元の５段加速器から 500 keV H^-イオンビームを生成する３段加速器へ変更する際に必要な改造項目を明確にし、かつその物理設計を実施することである。２次元ビーム解析コードを用いたビーム光学研究において、電極孔径、電極厚み、電極間ギャップを最適化し、改造項目を明らかにした。3 次元マルチビームレット解析において、ビームレット同士の空間電荷反発と磁場によるビーム偏向を補正するための孔ずれ付き電子抑制電極、またビームレットを集束するための孔ずれ付き接地電極を設計した。３次元ガス解析において、ビーム光学研究で提案した改造を適用した場合に、負イオンの中性化損失は殆ど変化せず、イオン源周りのガス圧は高電圧保持の設計要求値を満足することを確認した。最後に、加速器の改造項目をまとめた。

那珂核融合研究所（駐在）：〒311-0193　茨城県那珂市向山801－1

Contents

目次

Table lists

Figure lists

This is a blank page.

1. Introduction

In the ITER neutral beam (NB) system for plasma heating and current drive, a five stage Multi Aperture Multi Grid (MAMuG) accelerator capable of accelerating 1 MeV 40 A D^- and 870 keV 46 A H^- has been designed. However, so as to suppress the shinethrough in the initial H^- operation of ITER, it was required to reduce the beam energy to 500 keV maintaining the high H^- ion beam current. The JAEA has started physics design of 500 keV H^- accelerator. The targets of this study are to design a 500 keV H^- accelerator and to identify the necessary modifications from the original five stage MAMuG accelerator to the 500 keV H^- accelerator suitable for the shinethrough mitigation maintaining the injection power as high as possible.

In Chapter 2, the original design of the five stage MAMuG accelerator is reviewed. In Chapter 3, the basic design of the 500 H^- keV accelerator is defined. In Chapter 4, the accelerator structure is examined and optimized based on the beam optics in the two dimensional beam analysis. In Chapter 5, compensation of beamlet deflections due to its space charge repulsion and magnetic field, and beamlet steering for focussing are analyzed in three dimensional beam calculations. In Chapter 6, gas flow and stripping loss are evaluated in the JAEA gas flow code. In Chapter 7, the items regarding the modifications of accelerator structure are summarized.

2. Review of five stage MAMuG accelerator to produce 1 MeV 40 A D^- and 870 keV 46 A H^- ion beams

Figure 2.1 shows the original five stage MAMuG accelerator capable of accelerating 1 MeV 40 A D^- and 870 keV 46 A H^- [2.1)]. The extractor consists of a plasma grid (PG) and an extraction grid (EXG). The accelerator has four acceleration grids named A1G, A2G, A3G, A4G and a grounded grid (GRG). Each grid consists of four segments, which are lined up in longitudinal direction. In each segment, 320 apertures are drilled to accelerate each beamlet through them. And hence in total, 1280 beamlets are accelerated.

Figure 2.2 shows the detailed configuration around one aperture in the accelerator. Diameters of the aperture are 14 mm in the plasma grid and 11 mm in the extraction grid. The extraction gap distance between the plasma grid and the extraction grid is 6 mm. The voltage applied between the plasma grid and the extraction grid is 12 kV at the maximum. So-called "electron suppression grid (ESG)" is attached to the backside of the extraction grid. The grid in the accelerator is 20 mm in the thickness and 16 mm in the diameter. The acceleration voltage is applied to each grid equally. Therefore, 200 kV is applied to each grid for 1 MeV beam acceleration. The acceleration gap distance between each acceleration grids is shortened progressively toward downstream such as 86 mm, 77 mm, 68 mm, 59 mm and 50 mm.

In the integrated design of NB power supply system [2.2)], the capable beam current at top of the accelerator was designed to be 66 A, which takes into account a safety margin of 5 % in the power supply current. In order to produce 1 MeV, 40 A D^- ion beam or 870 keV, 46 A H^- ion beams, it was estimated that the negative ion currents extracted from the plasma grid were 59.4 A (300 A/m^2) D^- and 62.8 A (320 A/m^2) H^-, respectively.

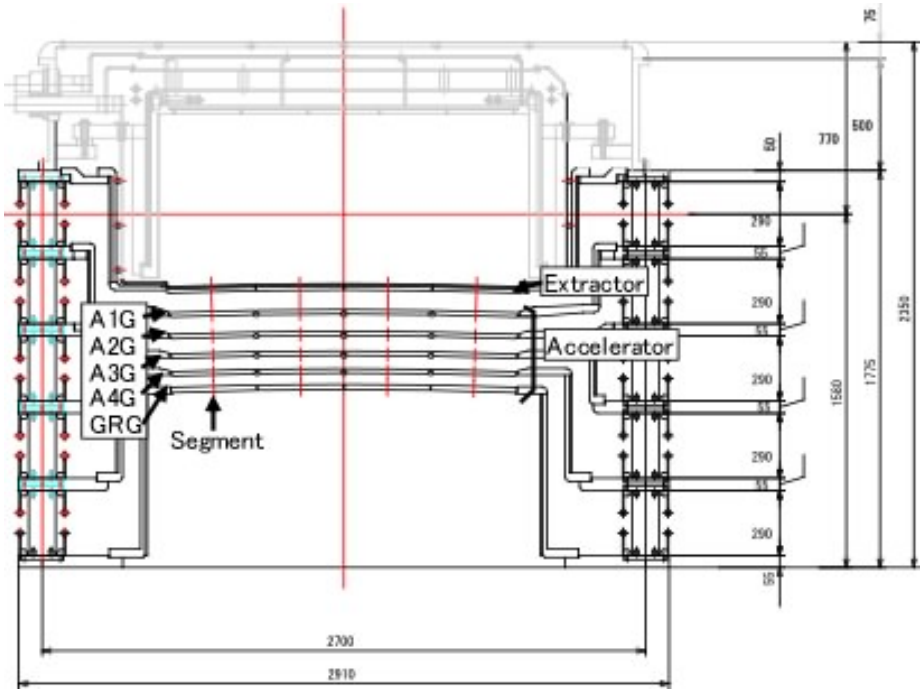

(a)

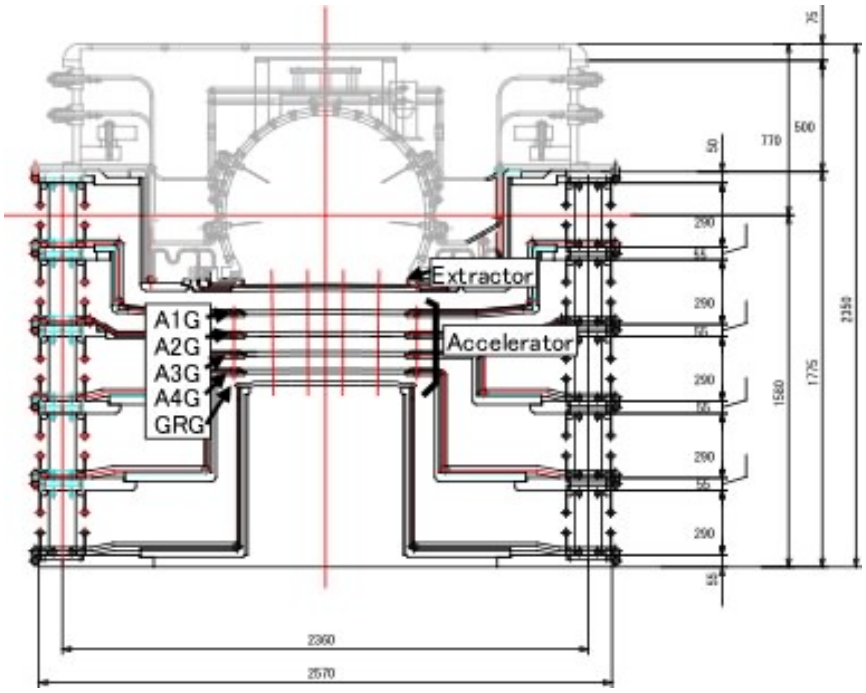

(b)

Fig.2.1. The five stage MAMuG accelerator to accelerate 1 MeV 40 A D^- and 870 keV 46 A H^- ion beams.

(a) Longitudinal direction and (b) horizontal direction. The ion beams are accelerated from top to bottom in the figure.

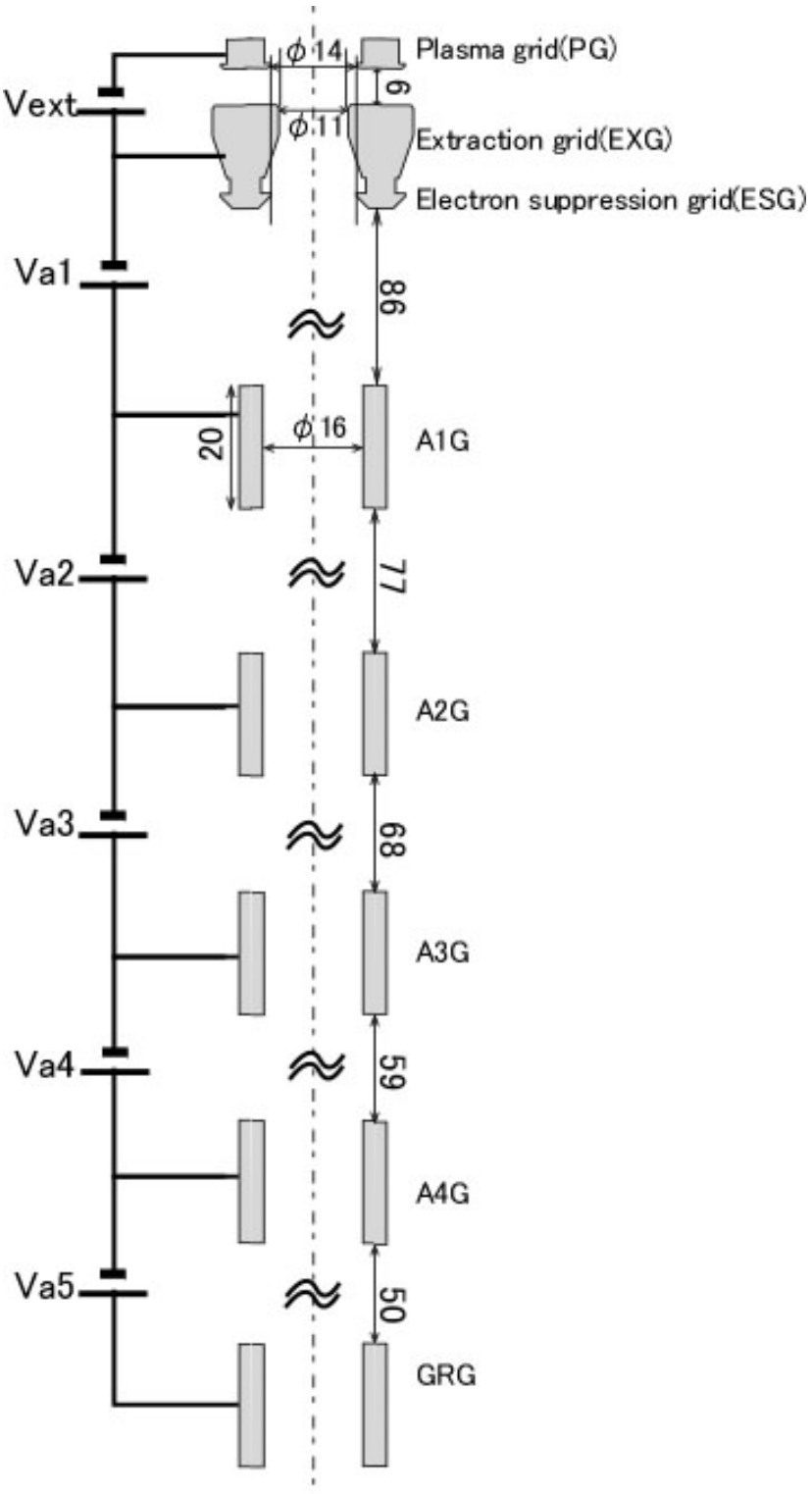

Fig.2.2. Accelerator structure around one aperture in the five stage MAMuG accelerator.

3. Basic design of accelerator to produce 500 keV H^- ion beam

So as to produce 500 keV H^- ion beam, number of acceleration grid can be reduced from five to three because the capable acceleration voltage in each acceleration grid was designed to 200 kV as shown in Chapter 2. The accelerator with shorter gaps is also desirable to reduce/suppress stripping loss of negative ions in the accelerator and also to obtain higher H^- ion beam current. Therefore, the three stage MAMuG accelerator was designed in this study. The A4G and GRG in the original five stage MAMuG accelerator are removed. The acceleration grids are named A1G, A2G and GRG. The ion beam current at the plasma grid is defined to be the maximum current in the power supply capability due to requirement from the ITER organization [3.1)].

The beam energy and current in this study were defined as follows.

- H^- ion beam energy : 500 keV
- H^- ion beam current : 66 A (maximum current in power supply capability. See Section 2).

It was estimated that the H^- ion current density which is extracted from the plasma grid was 335 A/m^2. Here, the total current of 66 A was divided by the total extraction area of 1280 apertures, 1970 cm^2. Note that the H^- current density of 335 A/m^2 is higher than those in the existing negative ion sources. In the MeV Test Facility (MTF) to demonstrate the ITER class high power beam acceleration [3.2)], it was estimated that the extracted H^- current density was 260 A/m^2 at 1 MeV under the optimum beam optics. In JT-60U negative ion source [3.3)], the required D^- current density at the plasma grid was estimated to 280 A/m^2 H^- at 500 keV under the optimum beam optics.

4. Optimization of the grid structure based on the beam optics study

4.1 Introduction of beam optics study

Based on the basic design of the accelerator as described in Chapter 3, the structure of the three stage 500 keV H^- accelerator with 335 A/m^2 H^- was examined by utilizing the two dimensional beam trajectory analysis code, BEAMORBT [4.1)]. The diameter of aperture, the gap length between grids and the thickness of acceleration grid were optimized through analyses of beam optics such as the beam trajectory and the Root Mean Square (RMS) divergence angle.

4.2 Two dimensional beam trajectory analysis

The two dimensional beam trajectory analysis code, the BEAMORBT, was developed to calculate the positive ion beam trajectory, and hence, the current analyses have been done assuming that the negative ions are accelerated based on an identical physics to that of positive ions. Thus the emitter surface of positive ions is defined according to the Child-Langmuir law. The space charge made by the beam particles is included in the calculation of beam trajectory. The BEAMORBT was applied to the design of the negative ion accelerators for the MTF [4.2)], JT-60U [4.3)] and ITER [4.4)].

When the BEAMORBT is applied to calculation of negative ion trajectory, it is necessary to pay attentions the following matters.

- The emitter surface of negative ions is defined according to the Child-Langmuir law, simply utilizing the emitter surface obtained in the analysis of positive ions.
- It is assumed that the negative ions distribute uniformly in the aperture and the space charge given by electrons is negligibly small. The space charge effect is proportional to the production of current and mass. It was confirmed experimentally that the extracted negative ion current and electron current was comparable [4.5)]. Then, the space charge effect by electron is expected to be small, that is, about one-fortieth of that by negative ion.
- Negative ions, extracted from aperture edge in the plasma grid, were neglected in the analyses in order to get better representation of core beams rather than beam halo formed by the ions extracted from edge region of aperture and then accelerated in fringe field.
- The effect of stripping within the accelerator (reducing space charge with distance) is not taken into account.

It is regarded from these matters that the absolute values of calculated divergence angle by the BEAMORBT will be smaller than the measured ones.

As example of the beam optics study, the divergence angles in a five stage MAMuG accelerator of the MTF are shown in Fig.4.1. The beam energy was 750 keV. The divergence angles were measured by a beam optical measurement [4.6], where H_α light intensity from the beam path was detected by a CCD camera. The beamlets were extracted from aperture array in a lattice pattern of 3 × 3. Then, 3 x 3 beamlets were superimposed to three columns in a view of the CCD camera. The divergence angle was analyzed in each superimposed beamlets as represented "left", "center" and "right" according to the image appeared in the monitor as shown in Fig.4.1. The divergence angle was defined by assumption of point light source at plasma grid. The distance between the plasma grid and CCD camera is about 2.5 m. The minimum divergence angle was about 5 mrad at Vext = 5.5 - 5.7 kV. The beam current density measured by a calorimeter was 134 A/m^2. Taking into account of the stripping loss of H^- ions in the accelerator, the H^- current density at the plasma grid was estimated to be 200 A/m^2.

In a numerical study by utilizing the BEAMORBT, the H^- ion beam trajectories with the current density of 200 A/m^2 at the plasma grid were analyzed. The calculated divergence angle became also minimum at Vext = 5.5 kV. The curve of divergence angle in the BEAMORBT showed good agreements with that in the measurement. However, the absolute value of divergence angle in the BEAMORBT was 3 mrad and smaller than those in the beam optical measurement. The smaller divergence in the numerical results will be caused by the assumptions in application of 2D beam analysis as expressed upper. The divergence angle in the measurement might be overestimated by the assumption of a point light source at the plasma grid.

4.3 Results

4.3.1 Extraction gap distance

Figure 4.2 (a) shows RMS divergence angle of H^- ion beams as a function of extraction voltage, Vext. In the right axis, the accelerated H^- ion current from one aperture is shown. If all H^- ions are accelerated without loss at the grid, the accelerated H^- ion current will be about 515 mA. The extraction gap distance was the original one, 6 mm. It looks that the minimum divergence angle was obtained at Vext = 7.5 kV. However, the beam current decreased gradually at Vext < 7.8 kV due to loss of the H^- ion beam at the extraction grid.

Figure 4.2 (b) shows the beam trajectory at Vext = 7.8 kV. The beam trajectory passed very close to the extraction grid. The beam expanded inside the aperture in the extraction grid due to weak electric field and space charge effect, which was larger at the low energy. Then, peripheral part of the beam was intercepted and lost in the extraction grid at Vext < 7.8 kV. When the extraction voltage was increased, the beam trajectory was much squeezed in the extraction gap and then emerged to the accelerator without interception at the extraction grid, but expanded considerably in the accelerator. As the results, the beam divergence angle became larger. These results show that there was no optimum beam optics in this configuration of extractor and accelerator. In the present design, it seems that the extraction gap distance was too long to extract such high density H^- ion beam.

Figure 4.3 (a) shows the RMS divergence angle and the accelerated H^- ion current as a function of Vext at a shorter extraction gap distance of 5 mm, which made the electric field strengthen. The minimum divergence angle was obtained at 7.0 kV without the beam loss.

Figure 4.3 (b) shows the beam trajectory at Vext = 7.0 kV. The beam was departed from the extraction grid surface. Thus the beam interception at the extraction grid can be suppressed by using shorter extraction gap of 5 mm.

4.3.2 Diameter of aperture in the extraction grid

Figure 4.4 shows the RMS divergence angle and H^- ion beam current as a function of diameter of aperture in the extraction grid. Referring to the results of section 4.3.1, the extraction gap distance was 5 mm and the extraction voltage was 7 kV. In case (1) shown in Fig.4.4, the diameter of aperture in the electron suppression grid was kept to be 14 mm as in the original. The beam current decreased with increase of the aperture diameter in the extraction grid. This was caused by the expansion of beam in the extraction grid and interception at the electron suppression grid as discussed in Chapter 3. In case (2) shown in Fig.4.4, the diameter of aperture in the electron suppression grid was changed in proportional to the increase of the diameter of aperture in the extraction grid. When the diameters of aperture in the extraction grid were 11 mm in the original and 14 mm, the diameter of aperture in the electron suppression grid were 14 mm in the original and 17 mm, respectively. The beam current was maintained when the diameter of aperture in the extraction grid was varied. The minimum divergence angle was obtained at 14 mm in diameter of the extraction grid, which was same as the diameter of aperture in the plasma grid.

Figure 4.5 shows the beam trajectories at 11, 14 and 16 mm in the diameter of aperture in the extraction grid. Each diameter of aperture in the electron suppression grid was 14 mm in original, 17 mm and 19 mm, respectively. The reasons of bad beam optics in small diameter as 11 mm could be considered as follows. The beam that was extracted from the aperture of 14 mm in diameter in the plasma grid was much squeezed in the smaller aperture in the extraction grid. Then, the beam expanded downstream of the extractor. The beam also passed in the fringe field around aperture of the extraction grid and was diverged. When the diameter was large such as 16 mm, the beam was divergent by the weaker electric field. It is shown that the optimum beam optics was obtained when the diameters of aperture in the extraction grid was the same as that in the plasma grid.

Figure 4.6 shows the grid structure of original and proposed here.

Note the following two comments. One is that it is expected that the stripping loss of negative ions increases in the extraction grid with the larger aperture. This is discussed in Chapter 6. Another one is that it is expected that the displacement in aperture offset for compensation of beamlet repulsion will be limited about 1 mm because pitches between neighbouring apertures are 20 mm and 22 mm in each direction. This is discussed in Chapter 5.

4.3.3 Acceleration gap distance

Figure 4.7 shows the RMS divergence angle as a function of 1st acceleration gap distance between ESG and A1G. The 1st acceleration gap distance was changed from the original gap distance of 86 mm. The gap distance between A1G and A2G (2nd acceleration gap) and A2G and GRG (3rd acceleration gap) were kept in the original ones of 77 and 68 mm. The divergence angle became smallest around the original gap of 86 mm in gentle sloop of the divergence angle curve. The minimum divergence angle was obtained at 88 mm. Thus from this figure, the optimum beam optics can be obtained in the range of 88 mm ± 2 mm in the 1st acceleration gap distance.

Figure 4.8 shows beam trajectories at the 1st acceleration gap distance of 80, 86 and 90 mm. At 80 mm, the beam was squeezed by strong electric field. When the beam was much squeezed, the beam started expanding in the downstream due to its own space charge. Hence the best beam optics, i.e. minimum divergence angle, was achieved when the squeezing of beam was suppressed maintaining substantial diameter. On the contrary, at 90 mm, the beam becomes divergent by the weaker electric field.

Figure 4.9 shows the RMS divergence angle as a function of 2nd acceleration gap distance. The 1st and 3rd acceleration gap distances were kept to 88 mm and 66 mm, respectively. The divergence angle was almost constant within ± 10 mm around the original gap distance of 77 mm. Thus the beam optics is not sensitive to the 2nd acceleration gap distance.

Figure 4.10 shows the RMS divergence angle as a function of 3rd acceleration gap distance. The 1st and 2rd gap distances were kept to 88 mm and 77 mm, respectively. The divergence angle was almost constant within ± 10 mm around the original gap distance of 68 mm.

In the mechanical point of view to modify the accelerator, it is useful if the gap distance in the 500 keV three stage MAMuG accelerator was closer to that in the original 1 MeV five stage MAMuG accelerator. Therefore, it is proposed not to change the gap length even in the 500 keV accelerator, namely, to maintain the 1st, 2nd and 3rd acceleration gap distance as it was, to be 88, 77 and 66 mm, respectively.

4.3.4 Acceleration grid thickness

Figure 4.11 shows the RMS divergence angle as a function of acceleration grid thickness. The acceleration grid thickness was originally 20 mm. To suppress the beam divergence by the fringe field around the aperture edges and the secondary electron emission by ion bombardment to side wall of the grid aperture, the thinner grid is favourable. On the contrary, the beam diverges when the electric field around the thinner grid is weaker. The RMS divergence angle slightly increased at the thickness > 7 mm. Then, the grid thickness can be reduced from 20 mm to around 10 mm.

4.3.5 Beam optics at each current density

Figure 4.12 shows the RMS divergence angle as a function of extraction voltage at each current density of 260, 300 and 335 A/m^2. The extraction gap distance was 5 mm. A diameter of aperture was 14 mm in the extraction grid. The 1st, 2nd and 3rd acceleration gap distance were 88, 77 and 66 mm, respectively. As introduced in Chapter 3, we worry about the very high current density and wonders if it is prudent to prepare for some case with lower current density. The divergence angle shown in Fig.4.12 as a function of current density indicated that the divergence angle was able to be smaller under lower current density by choosing a suitable extraction voltage even in the maximum acceleration voltage of 500 kV.

4.4 Summary of beam optics study

The three stage MAMuG accelerator which accelerate 335 A/m^2 (at the plasma grid, totally 66 A) H^- ion beam up to 500 keV was examined and designed from the viewpoint of beam optics. The items to modify from the original five stage MAMuG accelerator were summarized in Table 4.2. It was found through the analyses utilizing the 2D beam analysis code that the divergence angle was sensitive to the extraction gap, a diameter of aperture in the extraction grid and the 1st acceleration gap distance. On the contrary, the beam divergence angle was not sensitive to the 2 nd and 3 rd acceleration gap distances. In the studies of the gas flow / stripping loss of negative ion (see Chapter 6), the modifications shown here will be included and examined.

Table 4.2. List of modification items from the five stage MAMuG accelerator to the 500 keV H^- accelerator.

Items	The original five stage MAMuG accelerator	500 keV H^- accelerator
Number of acceleration grid	Five	Three
Ion beam energy	1 MeV for D^-, 870 keV for H^-	500 keV for H^-
Extraction ion beam current	59.4 A D^-, 62.8 A H^-	66 A H^-
Ion beam current density	300 A/m^2 D^-, 320 A/m^2 H^-	335 A/m^2 H^-
Extraction gap distance	6 mm	5 mm
Diameter of extraction grid	11 mm	14 mm
1st accel. gap distance and tolerance	86 mm	88 mm ± 2 mm
2^{nd} accel. gap distance and tolerance	77 mm	77 mm ± 10 mm
3^{rd} accel. gap distance and tolerance	68 mm	68 mm ± 10 mm
Thickness of acceleration grid	20 mm	Acceptable to reduce to 10 mm

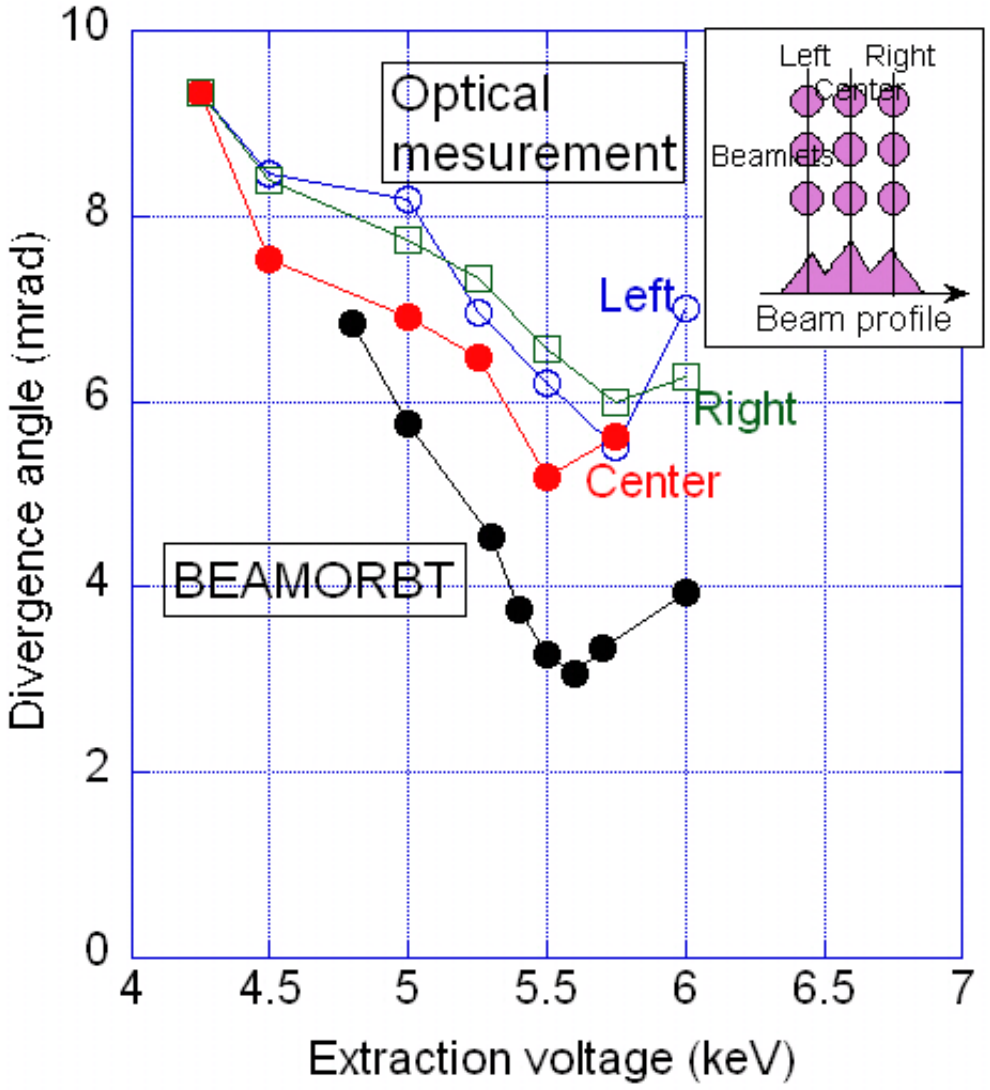

Fig.4.1. Divergence angle of H^- ion beam in a five stage MAMuG accelerator of MTF. The divergence angles were obtained by the optical beam measurement and by 2D beam trajectory analysis code, BEAMORBT.

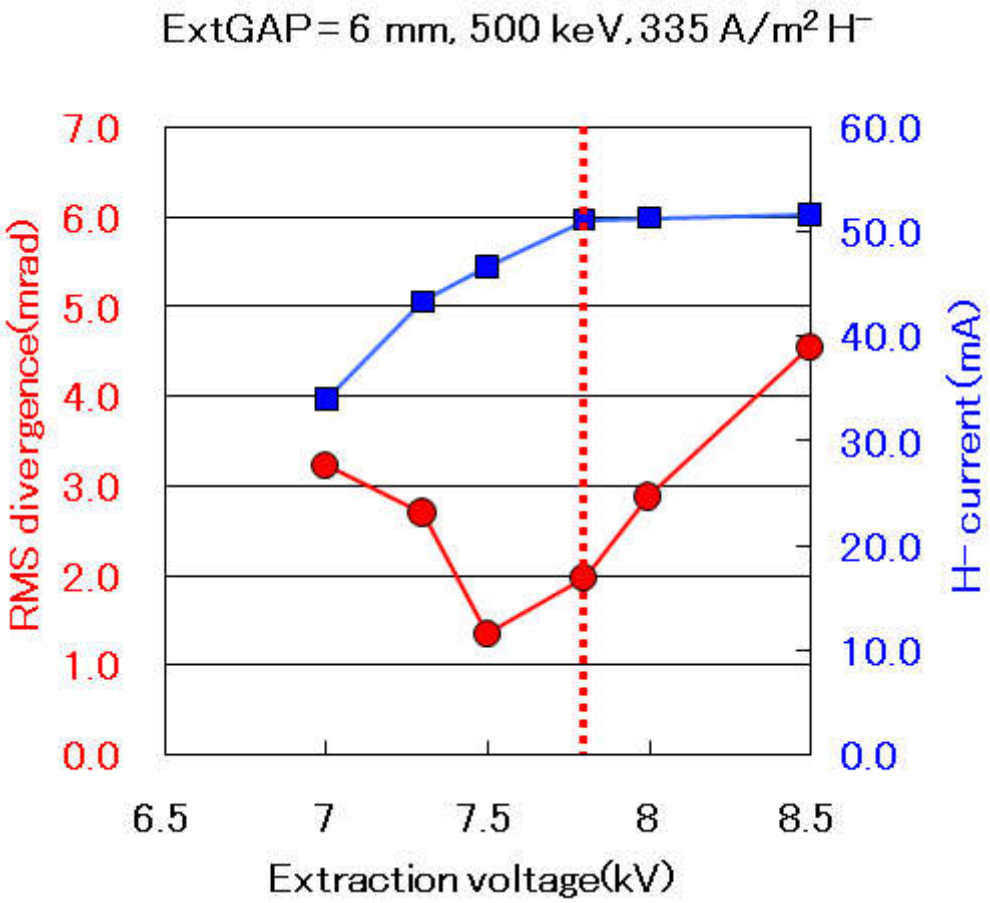

(a)

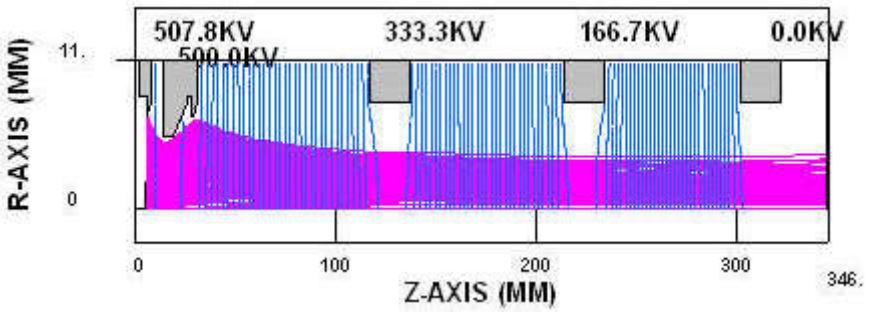

(b)

Fig.4.2. Calculated beam optics in a three stage MAMuG accelerator.
Two accelerator grids in the original five stage MAMuG accelerator were removed.
The extraction gap distance was 6 mm.
(a) RMS divergence angle (left axis, circles) and H^- ion bean current (right axis, squares) from one aperture against extraction voltage.
(b) Beam trajectory at minimum divergence angle when Vext was 7.8 kV.

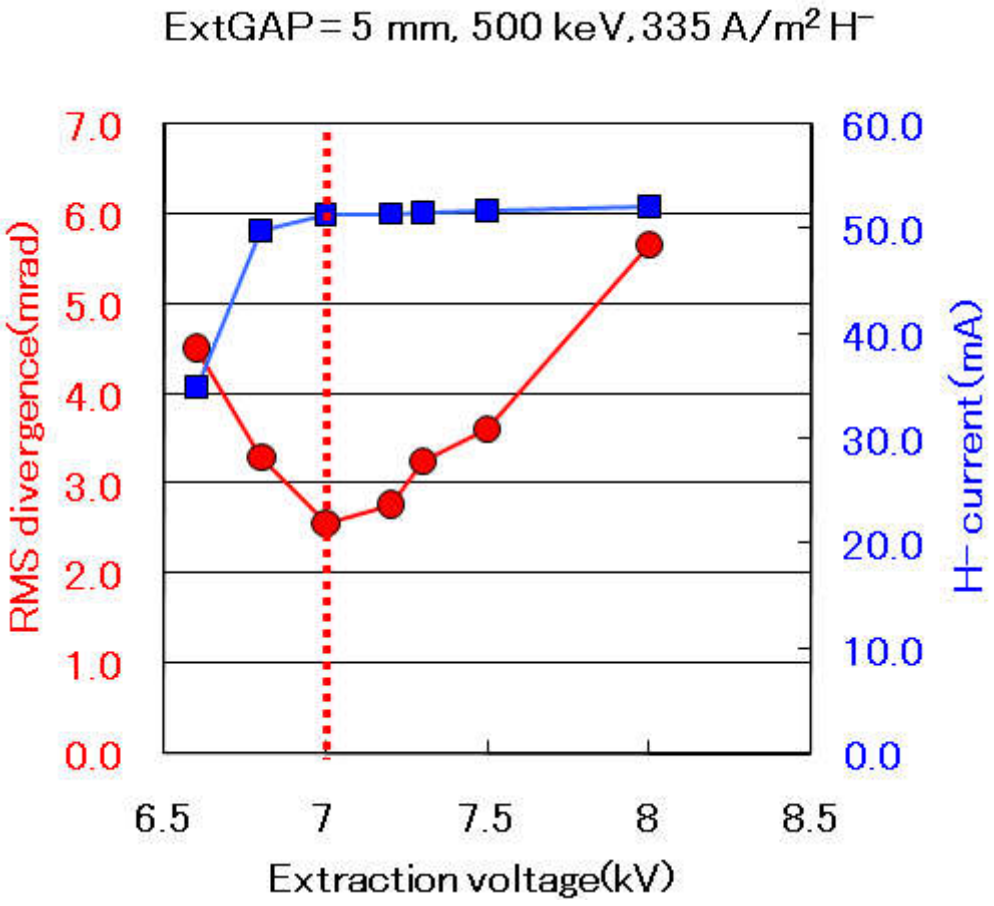

(a)

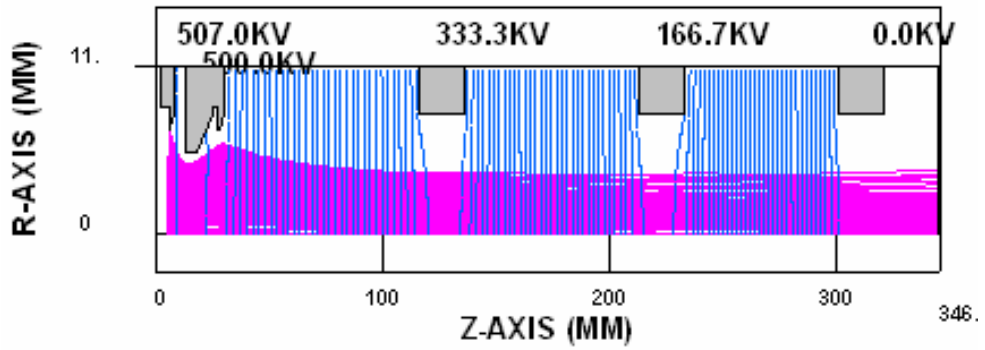

(b)

Fig.4.3. Calculated beam optics at extraction gap distance of 5 mm.

(a) RMS divergence angle (left axis, circles) and H^- ion beam current (right axis, squares) against extraction voltage. (b) Beam trajectory at minimum divergence angle when Vext was 7.0 kV.

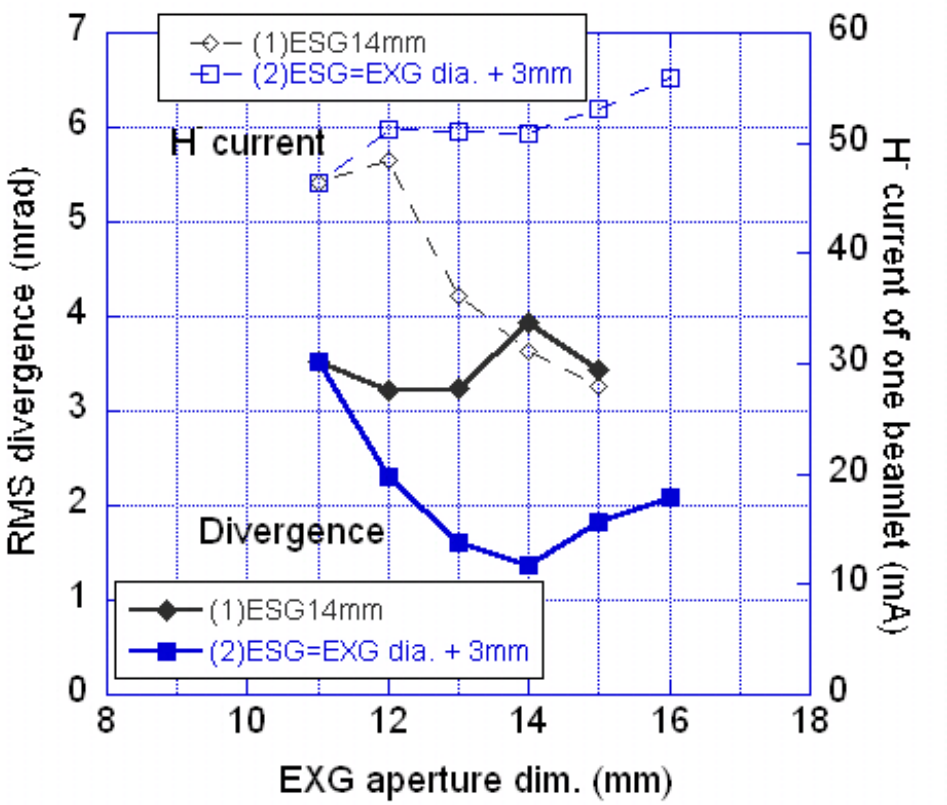

Fig.4.4. Calculated RMS divergence angle against a diameter of aperture in the extraction grid.

The extraction gap distance was 5 mm. The diameter of aperture in the electron suppression grid was (1) maintained to be 14 mm in and (2) 3 mm larger than that of in the extraction grid.

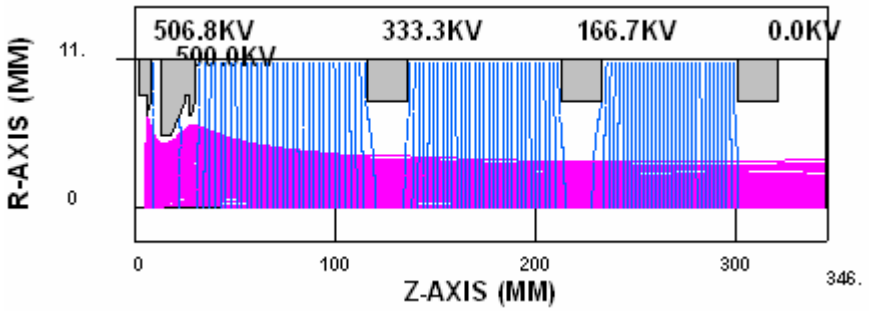

(a)

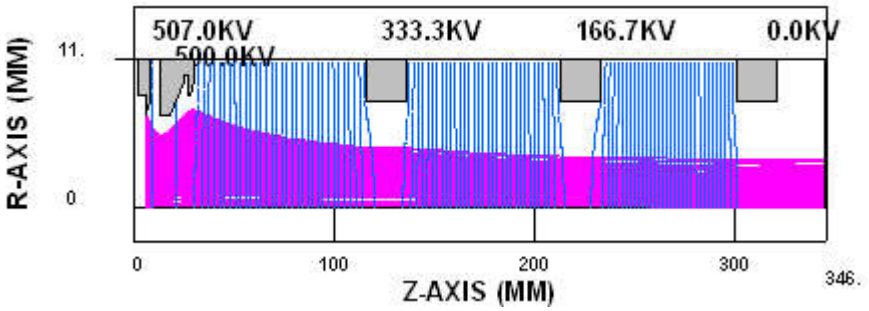

(b)

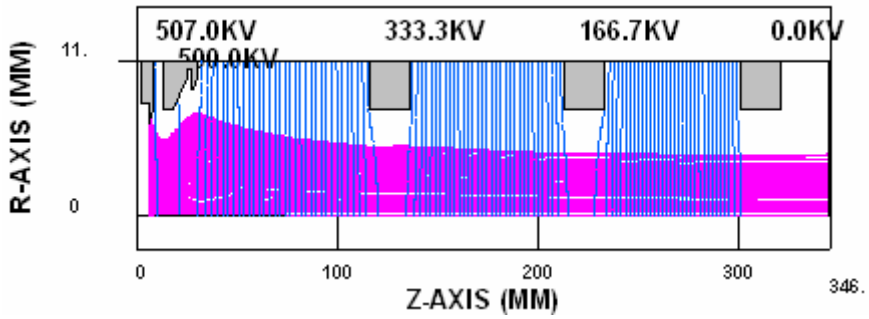

(c)

Fig.4.5. Beam trajectories at each diameter of aperture in the extraction grid.
Diameters of extraction grid were (a) 11 mm, (b)14 mm and (c) 16 mm. Diameter of electron suppression grid was 3 mm larger that of the extraction grid, that is, (a) 14 mm of original, (b) 17 mm and (c) 19 mm.

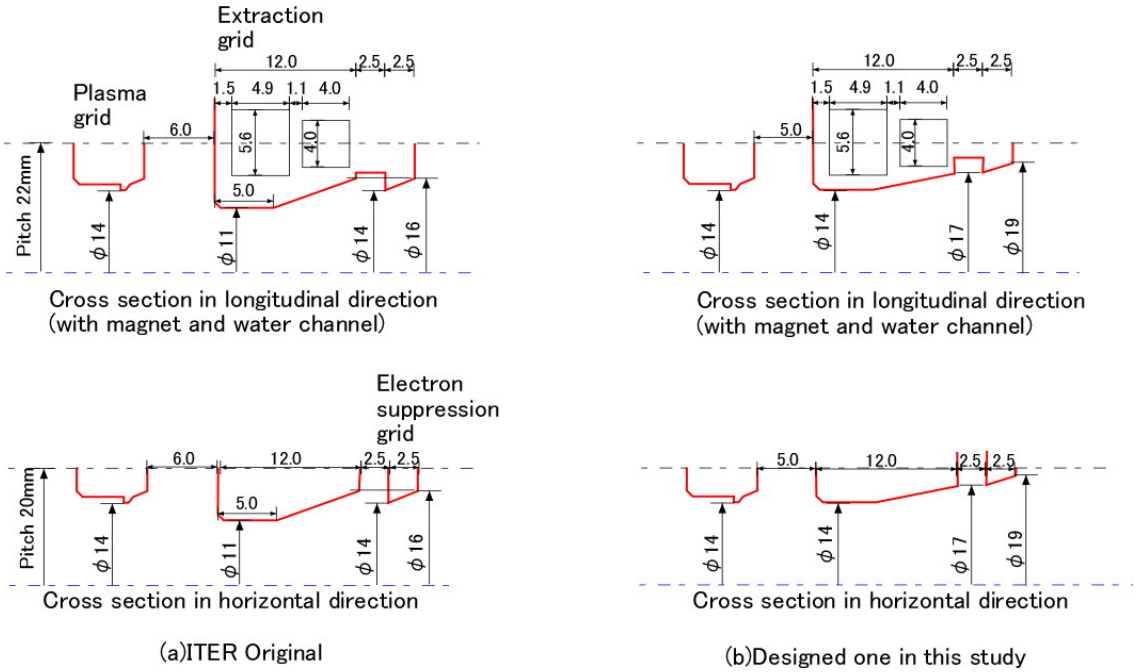

Fig.4.6. Cross section of grids in the extractor.
(a) Original and (b) designed configurations in this study.

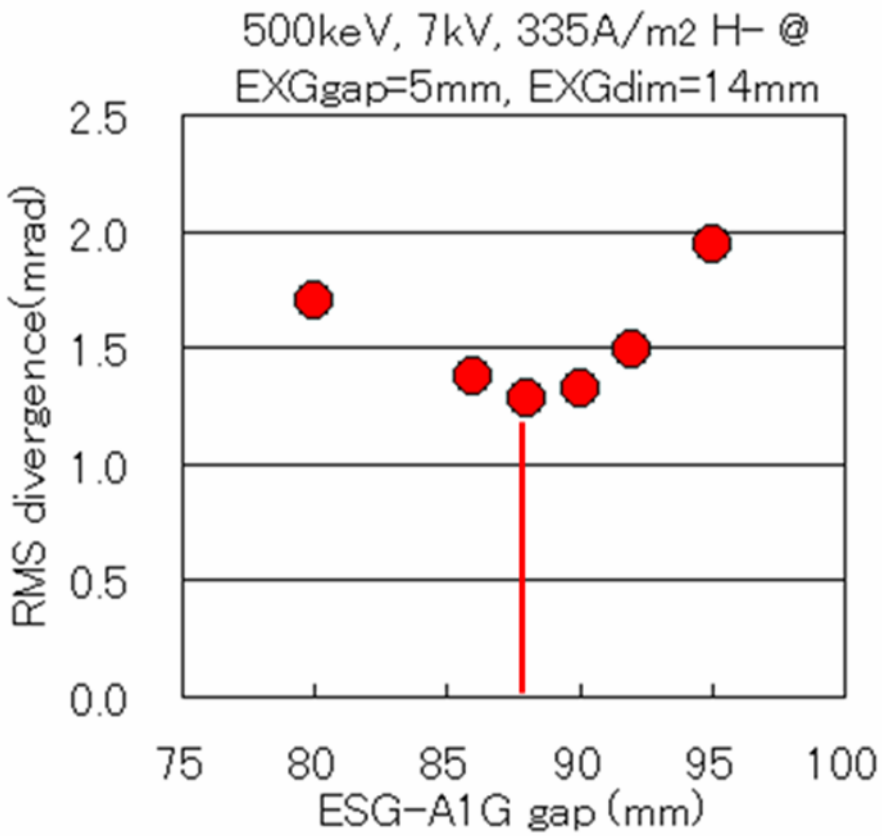

Fig.4.7. Calculated RMS divergence angle against gap distance between ESG and A1G (1st acceleration gap).

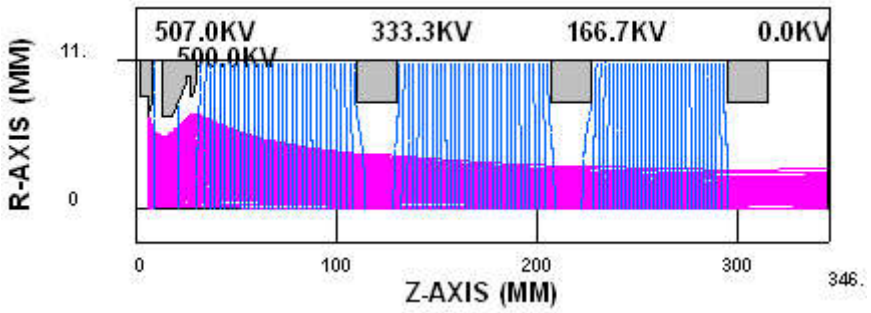

(a)

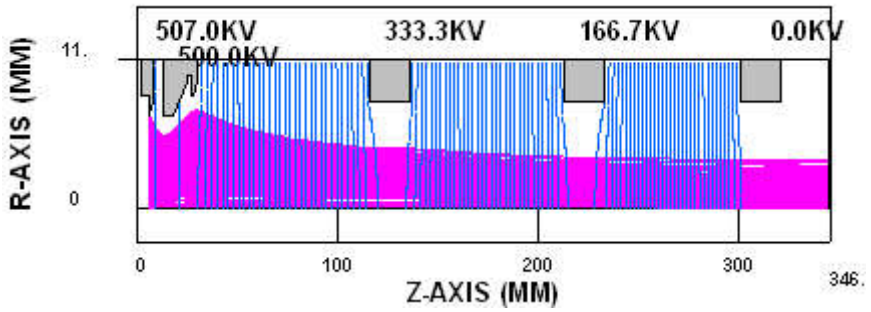

(b)

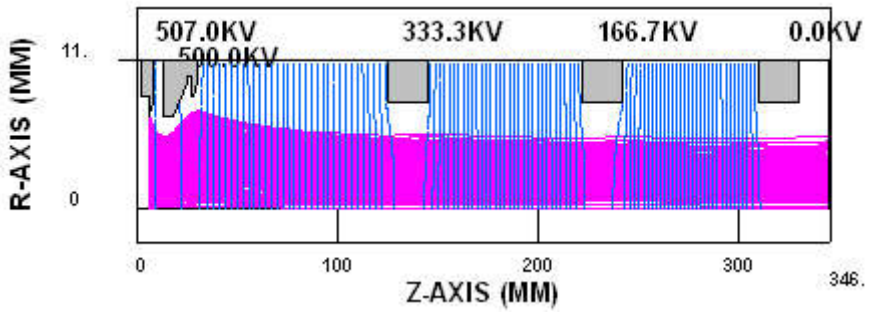

(c)

Fig.4.8. Beam trajectories at each distance of the 1st acceleration gap.

The 1st acceleration gap distance were (a) 80 mm, (b) 86 mm and (c) 90 mm. The divergence angle of each beam trajectory was corresponded with the data of Fig.4.6.

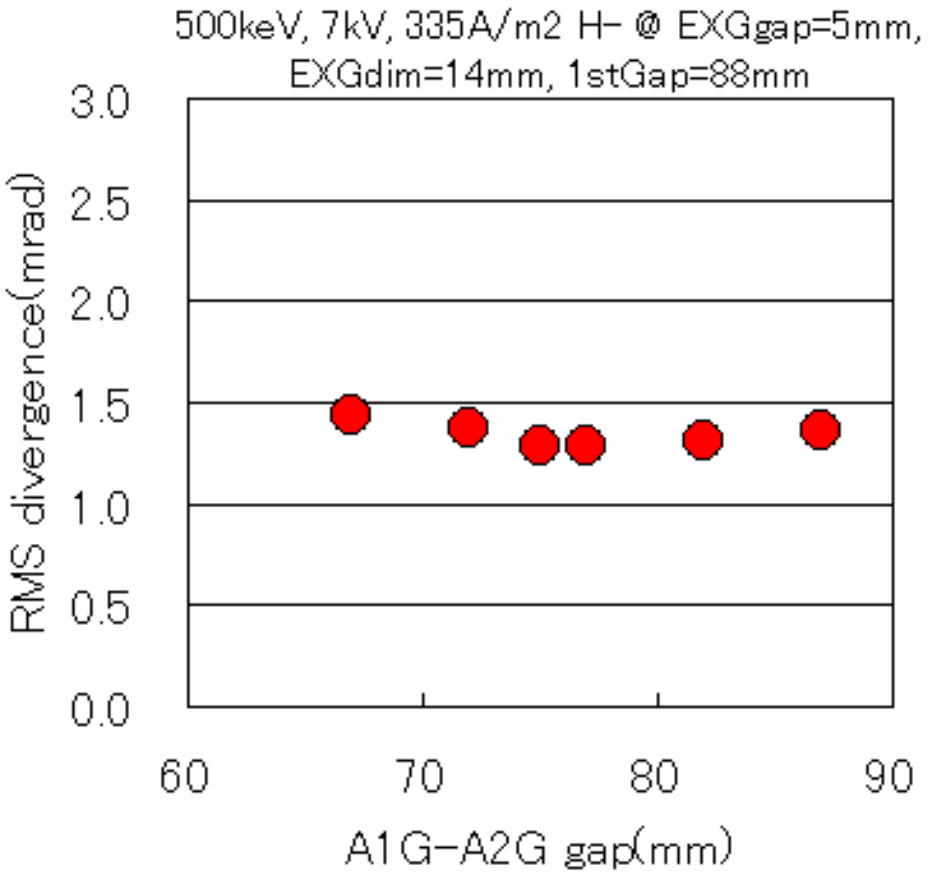

Fig.4.9. Calculated RMS divergence angle against gap distance between A1G and A2G (2nd acceleration gap).

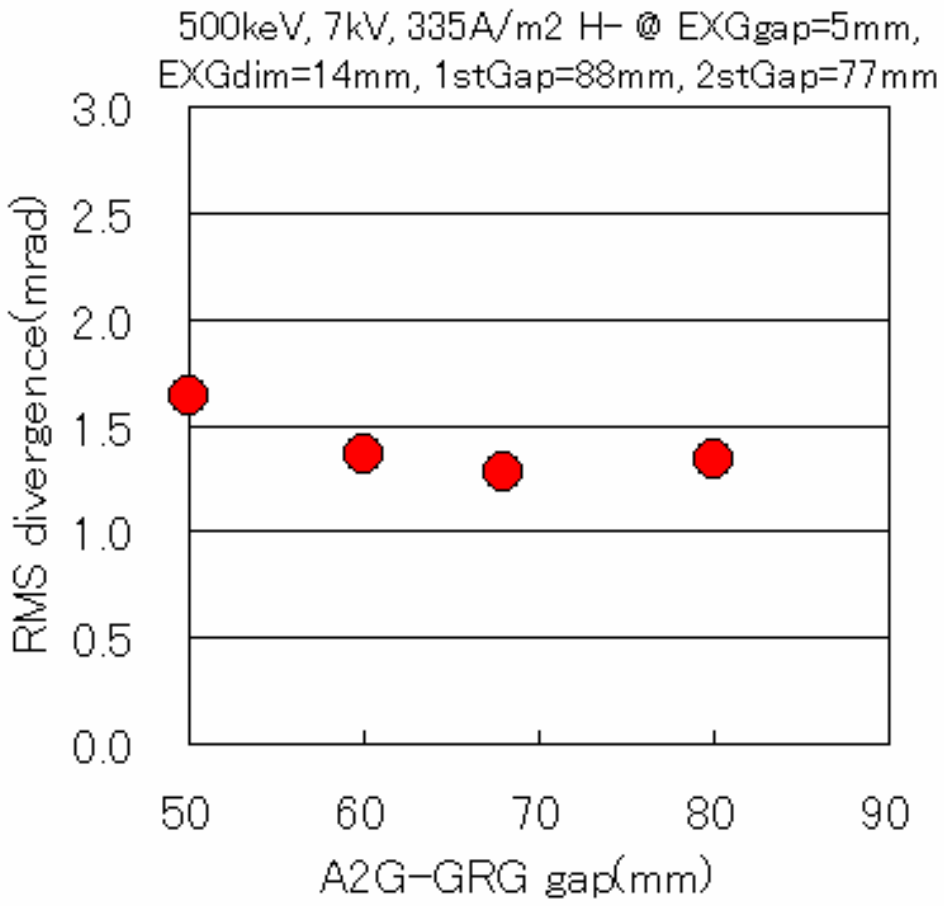

Fig.4.10. Calculated RMS divergence angle against gap distance between A2G and GRG (3rd acceleration gap).

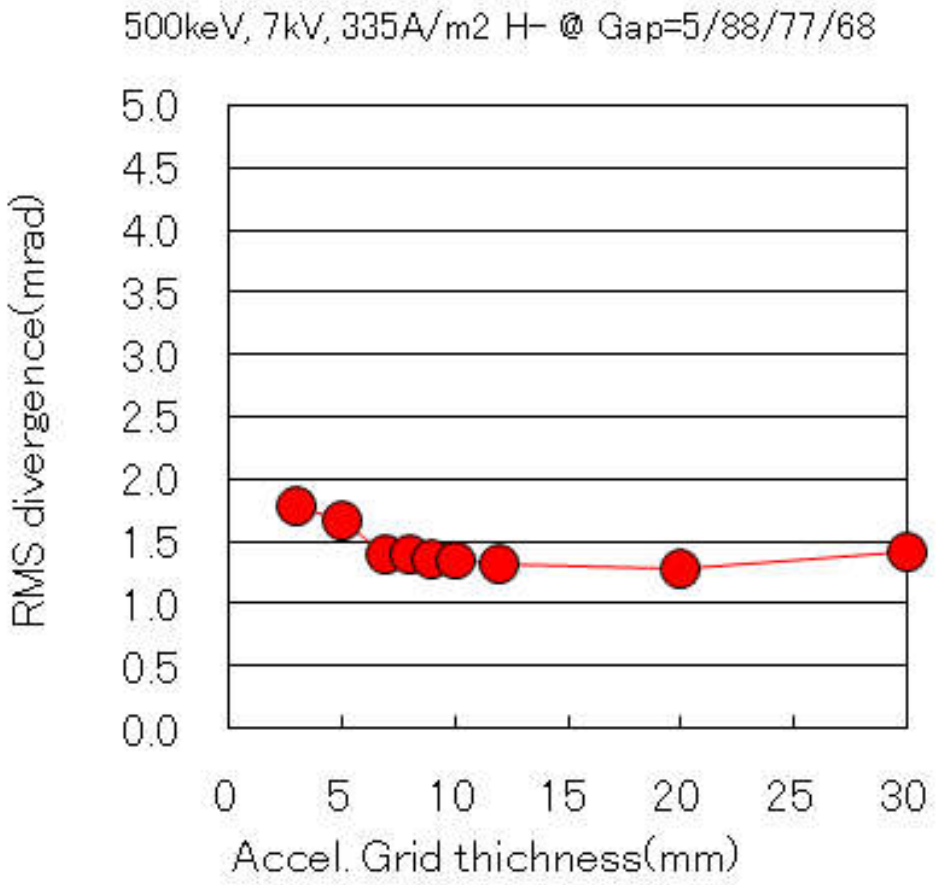

Fig.4.11. Calculated RMS divergence angle against acceleration grid thickness. 20 mm is the original thickness.

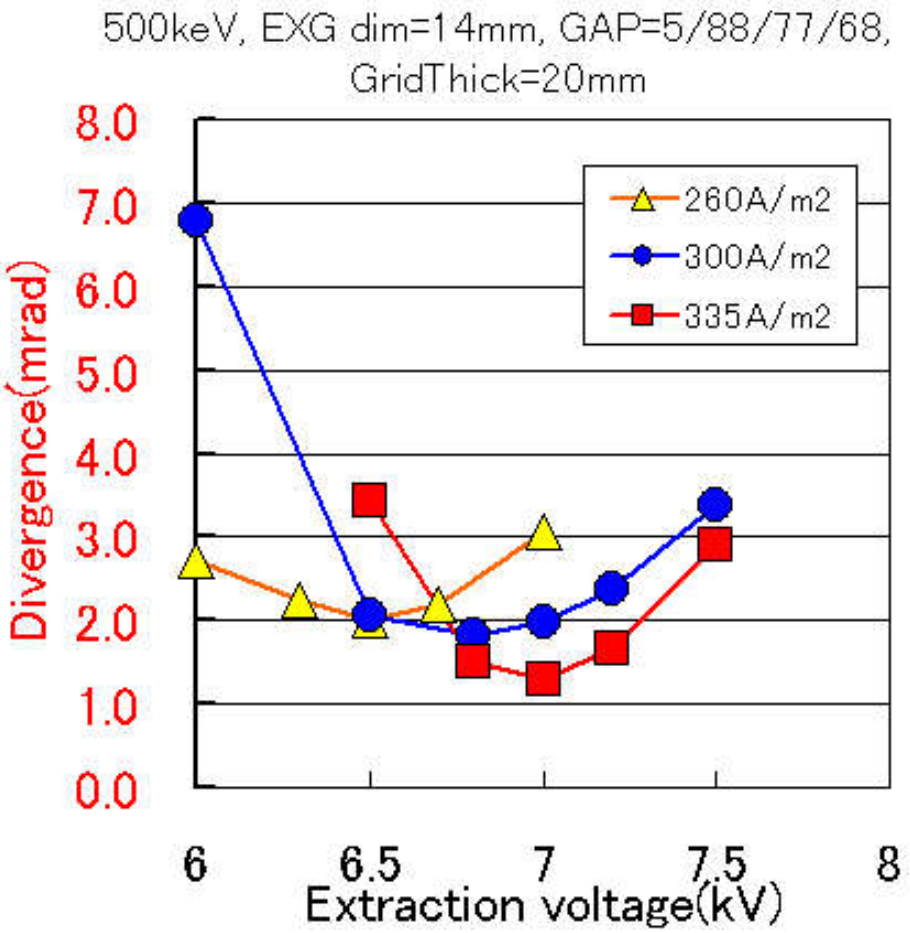

Fig.4.12. Calculated RMS divergence angle in each H^- ion beam current density at acceleration voltage of 500 kV.

5. Physics design for beamlet steering

5.1 Introduction of beamlet steering

In the large negative ion sources in neutral beam (NB) systems of JT-60U and ITER, excess heat loads on the accelerator grids and downstream components are one of issues in an extension of beam pulse length. A part of heat loads is generated by deflected beamlets due to their own space charge repulsion [5.1), 5.2)]. In JT-60U, metal bars were attached around the aperture area at the exit of the final grid in the extractor, namely, electron suppression grid [5-3)]. Formation of the electric field distortion around the metal bars steers the beamlets from outermost apertures to counteract the beamlet deflection, but the field distortion can not propagate to all extraction area.

In order to steer the beamlet for compensation of beamlet deflections, beamlet steering using aperture offset that is estimated according to thin lens theory [5.4), 5.5), 5.6), 5.7), 5.8), 5.9), 5.10), 5.11), 5.12), 5.13), 5.14)] is examined in this study utilizing three dimensional beam calculation code, OPERA-3d. In Sections 5.4.1, 5.4.2 and 5.4.3, the existing three stage negative ion accelerator of JT-60U is applied as the analytical model. In Section 5.4.1, the beamlet deflection by only the space charge repulsion and that compensation by aperture offset in the electron suppression grid are studied. In Section 5.4.2, the beamlet deflection by not only space charge repulsion but also magnetic field is analyzed. In Section 5.4.3, the beamlet steering toward focal point by aperture offset in the grounded grid is studied. Finally, in Section 5.4.4, proper aperture offsets in the three stage 500 keV H^- accelerator for the ITER NB are estimated based on the results in Sections 5.4.1 – 5.4.3.

5.2 Calculation model

Figure 5.1 shows the calculation model of a three stage multi aperture and multi grid (MAMuG) accelerator. In this study, fifty beamlets extracted from the apertures in a lattice pattern of 10 x 5 were analyzed. The apertures were located every 19 mm in X and 21 mm in Y directions. The accelerator grid structure was modelled on the JT-60U three stage D^- ion beam accelerator [5.14)]. The negative ions were emitted by the voltage difference (extraction voltage, Vext) applied between a plasma grid (PG) and an extraction grid (EXG). The permanent magnets for suppression of co-extracted electron were embedded into the EXG. This vertical magnetic field was generated around the EXG as shown in Fig.5-1. The beamlets are deflected in ±X directions alternatively in each aperture line by this vertical magnetic field. An electron suppression grid (ESG) was attached at the bottom of the EXG. The accelerator consisted of three grids, namely, 1 st and 2 nd acceleration grids (A1G, A2G) and grounded grid (GRG). One-thirds of the acceleration voltage (Vacc) was applied to each grid. Vacc was 500 keV at the maximum. This accelerator was designed so that the optimum beam optics was obtained at D^- current density (J_{D^-}) of 200 A/m^2, Vext = 8 kV and Vacc = 500 kV [5.12)]. In a typical operation condition of Vacc = 340 kV, it was obtained under maintaining the optimum perveance ($P = J_{D^-}/Vacc^{1.5}$) that J_{D^-} = 110 A/m^2 and Vext = 5.4 kV.

Multi beamlets analysis was carried out by utilizing the three dimensional beam calculation code, OPERA-3d on PC with the operating system of Windows [5.15)]. The beam trajectories started from the fixed beam emitter position. The iterative calculation of beam trajectory and electric potential generated by the space charge of beams were continued till obtaining the convergence. The beam emitter surface as the plasma boundary was able to be obtained from the Child-Langmuir law. To decide the beam emitter required for OPERA-3d, two dimensional beam calculation code, BEAMORBT [4.1)], was used. The BEAMORBT calculates the beam trajectory extracted from the beam emitter surface, which was decided by the Child-Langmuir law. Figure 5.2 shows the beam trajectory in BEAMORBT at Vacc = 500 kV, 200 A/m^2 D^- ion beam.

Figure 5.3 shows a beam trajectory and meshes around an beam emitter in OPERA-3d. When the emitter surface in BEAMORBT was directly transferred to OPERA-3d as shown in Fig.5-3 (a), the emitter surface was close to the PG surface. Then the mesh size around PG had to be subdivided into 0.1 mm to maintain high accurate electric field calculation, and subsequently, huge amount of memory was required. The number of beamlets was limited to only five because of the memory limitation (3 GB) for one application program in Windows OS. As a solution to increase number of beamlets, the beam emitter was changed to PG exit maintaining the particle position in BEAMORBT as shown in Fig.5-3 (b). At PG exit, the beamlets were far from the grid and the mesh size could be made relatively rough, 0.5 mm. Finally, the number of beamlets could be increased from five to fifty. Each beamlet consisted of 400 particles.

5.3 Beamlet steering by aperture offset

Figure 5.4 shows a schematic illustration of beamlet steering by the aperture offset in the ESG in the three stage negative ion accelerator. When aperture offset δ_0 is applied to the ESG, steering angle θ_0 at the ESG is expressed as,

$$\theta_0 = \frac{\delta_0}{F} = C_0\delta_0 . \quad \text{--- (1)}$$

Where F is a focal length, $F = \frac{4V_{BE}}{E_2 - E_1}$. $V_{BE}, E_2, and E_1$ is beam energy (keV) and electric field strength after and before the grid with aperture offset.

This deflected beamlet at the ESG is displaced from the axis of aperture in the acceleration grid even without aperture offset. The steering angle by these substantial aperture offsets at A1G, A2G and GRG, $\theta_1, \theta_2, \theta_3$, can be expressed as follows.

$$\theta_1 = C_1\theta_0, \qquad \theta_2 = C_2\theta_1, \qquad \theta_3 = C_3\theta_2 = C_0C_1C_2C_3\delta_0 = C(\alpha)\delta_0 . \text{ --- (2)}$$

Where C_0, C_1, C_2, C_3 are,

$$C_0 = \frac{1}{4d_1\alpha},$$

$$C_1 = \left[\left(\frac{\alpha}{\alpha+1}\right)^{1/2} - \frac{1}{2}\cdot\frac{d_1-d_2}{d_2}\cdot\frac{\left\{\alpha^{1/2}\cdot(\alpha+1)^{1/2}-\alpha\right\}}{\alpha+1}\right],$$

$$C_2 = \left[\left(\frac{\alpha+1}{\alpha+2}\right)^{1/2} - \frac{1}{2}\frac{d_2-d_3}{d_3}\cdot\frac{\left\{(\alpha+1)^{1/2}(\alpha+2)^{1/2}-(\alpha+1)\right\}}{\alpha+2}\right],$$

$$C_3 = \left[\left(\frac{\alpha+2}{\alpha+3}\right)^{1/2} + \frac{1}{2}\frac{(\alpha+2)^{1/2}(\alpha+3)^{1/2}-(\alpha+2)}{\alpha+3}\right] \quad \text{---(3)}$$

$$\alpha = \frac{V_0(=Vext)}{Vacc/3}. \quad \text{---(4)}$$

Then, the steering angle θ_3 at accelerator exit is defined by α, which is the ratio of extraction voltage and acceleration voltage. In this accelerator, θ_3 can be expressed as follows.

$$\theta_3 = C(\alpha)\delta_0 = 8.73\delta_0 \quad \text{--- (5)} \quad \text{(See Appendix 1)}$$

Eq.(5) shows that the steering angle by aperture offset is proportional to the distance of aperture offset and does not vary with the beam energy when the ratio of extraction voltage and acceleration voltage is maintained [5.11)].

In the ITER NB accelerator, it was designed that beamlets are steered to a focal point by the aperture offset in the GRG. It has been verified experimentally that the aperture offset in the GRG steered the beamlets according to the thin lens theory [5.12)]. The focal point is the exit of residual ion beam dump (RID). Focal length by the aperture offset in the GRG, $F_{GRG\text{-}RID}$, is expressed as $F_{GRG-RID} = -\frac{4V_{BE}}{E_1}$ [5.11)]. E_1 is the electric field strength before the GRG, that is $E_1 = \frac{V_{acc}}{3} / gap_{A2G-GRG}$. Then, steering angle ($\vartheta_{GRG}$) by the aperture offset in the GRG (δ_{GRG}) can be expressed as follows.

$$\theta_{GRG} = \frac{\delta_{GRG}}{F_{GRG-RID}} = -\frac{V_{acc}}{12V_{BE}\cdot gap_{A2G-GRG}} \quad \text{---(6)}$$

5.4 Results

5.4.1 Aperture offset in ESG to compensation of beamlet deflection by space charge repulsion

Figure 5.5 shows the bird's-eye view of the fifty beamlets in the accelerator. Vacc, Vext and J_{D^-} were set to 340 kV, 5.4 kV and 110 A/m^2, respectively. The magnetic field was not taken into account in this section to clarify the beamlet deflection by only space charge repulsion.

Figure 5.6 shows the calculated beam footprints before the aperture offset at 3.5 m downstream from the GRG, which corresponds to the position of the beam footprint measurement in the JT-60U experiment. The beamlet deflections were different in each aperture position. The center beamlets from peripheral apertures were most deflected outward, 6 mrad. The deflection angle of beamlets on the corner was 4 mrad. The beamlets in inside were deflected with the angle of 2 – 3 mrad.

Figure 5.7 shows the change of beamlet deflection angle from peripheral apertures of the aperture area, L3, L4 and L5 on column 10 in Fig.5-6. The beamlet deflection was not significant in extraction gap and increases gradually in the 1 st acceleration gap between the ESG and the A1G. It can be considered that the aperture offset according thin lens theory is useful at the ESG because the center of beamlets are still close to center of aperture.

Figure 5.8 shows (a) the distance of aperture offset in the ESG and (b) calculated beam footprint after aperture offset. To compensate the beamlet deflection of 6 mrad, the necessary aperture offset is 0.7 mm from Eq.(5). In Fig.5.8 (a), proper aperture offset to steer the beamlet and compensate the beamlet deflection shown in Fig. 5-6 were calculated from Eq.(5) and applied to all apertures in the ESG. These offsets were also applied to symmetrical region with respect to X and Y axes. In Fig.5.8 (b), it is shown that the beamlets flied straight from the GRG to downstream and were still within the projected position of each aperture even at 3.5 m downstream from the GRG. It was shown that proper aperture offset can compensate the space charge repulsion of all beamlets.

In Refs.5.8) and 5.9), it was indicated that the beamlet deflection angle by the space charge repulsion does not vary with the beam energy when the perveance ($=J_{D^-}/V_{BE}^{1.5}$) is maintained. To confirm this in this 3D numerical analysis, the beamlet deflection angle was examined when the beam energy was changed under the same perveance. Figure 5.9 shows the beamlet deflection angles of 340 keV, 110 A/m^2 D^- ion beam shown in Fig.5.7 and of the 500 keV, 200 A/m^2 D^- ion beam. The perveance and the ratio of extraction and acceleration voltage were the same in both beam conditions. It is clear in Fig.5.9 that the beamlet deflection angles were almost same in each aperture position. It was shown that the beamlet deflection angle by the space charge repulsion was the same maintaining the beam optics even if the beam energy was varied.

In real operation of NB accelerator, the extraction voltage is scanned to tune the beam optics. To investigate how sensitive is the steering angle of beamlet to extraction voltage, beam steering angle at aperture offset of 1.0 mm was calculated from Eq. 3 - 5 in each extraction voltage. Figure 5-10 shows the beam steering angle as a function of extraction voltage. The acceleration voltage was 340 kV and 500 kV. The optimum extraction voltage was 5.4 kV and 8.0 kV, respectively. When the extraction voltage was

scanned ±1 kV around the optimum extraction voltage, the steering angle changed about ±1.0 mrad at Vacc=340 keV and ±0.5 mrad at Vacc=500 kV.

5.4.2 Aperture offset in ESG to compensation of beamlet deflection by magnetic field

Figure 5.11 shows the calculated beam footprint at 340 keV, 110 A/m^2 by not only space charge repulsion but also magnetic field. The beamlets deflected in ±X alternatively at each line due to the dipole magnetic field around extraction grid.

In Fig.5.12, deflection angles in X direction are shown. The deflection angle in +X and –X under magnetic field is shown as ② and ③, respectively. As a reference, deflection angle without magnetic field in Fig.5-9 (a) is put as ①. The differences between before and after including magnetic field are shown as ④(=②-①) and ⑤(=③-①). These different, that is, deflection by only magnetic field, was about 5.4 mrad and was constant in each aperture column. When the beam energy was 500 keV, the deflection angle by magnetic field was 4.6 mrad. The deflection angle by magnetic field is proportional to 1/√(beam energy). Proper aperture offset to compensate these, about 0.65 mm for 340 keV beam and 0.5 mm for 500 keV. This was consistent with the previous experimental results [5.12)], and original design [5.11)].

Figure 5.13 shows deflection angles as a function of beam energy when the magnetic field was applied. When the aperture offset was set to 0.5 mm, which was proper aperture offset for compensation of 500 keV beamlet deflection by magnetic field, the deflection angle at 340 keV beam was suppressed to within 1 mrad.

5.4.3 Aperture offset in GRG for beamlet focussing

In the ITER NB design, the beamlets are focused at the exit of RID as shown in Fig. 5.14. In the aperture arrangement of 5 x 16 in one segment of the ITER accelerator, the beamlets from five aperture columns in X are focused horizontally toward the center aperture columns as shown in Fig.5.14 (a). In this calculation model with 10 x 5 apertures, beamlets from five aperture lines in Y were steered to the same focal length of ITER by the aperture offset in the GRG as shown in Fig.5.14 (b). The distance between the accelerator exit to the RID exit is 7200 mm in the original five stage 1 MeV D^- accelerator. That would be 7259 mm in the three stage 500 keV H^- accelerator. In this study, this distance of 7259 mm was defined as the focal length. The aperture offset in the ESG to compensate the beamlet repulsion was applied as shown in Fig.5.8. Then, all beamlets reached in the center of the original aperture position in the GRG.

In this calculation model as shown in Fig.5.14 (b), required steering angles of beamlets toward the exit of the RID were 5.6 mrad in L1 and L5 and 2.8 mrad in L2 and L4. The aperture offsets in the GRG calculated from eq.(6) were -3.7 mm in L1, -1.8 mm in L2, 0 mm in L3, +1.8 mm in L4 and +3.7 mm in L5. The beamlets which were compensated the beamlet deflections by ESG aperture offset and flied straight, were steered to the focal point by these GRG aperture offsets. Fig.5.15 shows the calculated beam footprint at the focal point, that was the exit of RID, utilizing the aperture offset in the GRG. It was confirmed that all beamlets were collected at the center aperture line and focused at the target position. Numerically, it was shown that the aperture offset in the GRG steer the beamlets according to thin lens theory.

5.4.4 Estimation of proper aperture offset in the three stage 500 keV H^- accelerator for the ITER NB

The deflection angle of beamlets and the proper aperture offset in the three stage 500 keV H^- accelerator for the ITER NB are estimated from the calculation results shown in previous sections.

5.4.4-1 Compensation of beamlet deflection

In Fig.5.16 (a) and (b), the aperture arrangement of this calculation model and the 500 keV H^- accelerator for the ITER NB are shown, respectively. The magnets for electron suppression were embedded horizontally between lines of aperture in both Fig.5.16 (a) and (b). The beamlet are deflected in ± X alternatively at each line due to the dipole magnetic field in Y direction. In the 500 keV H^- accelerator for the ITER NB, there are sixteen groups of apertures. In each group of aperture, the apertures are arranged in the lattice pattern of 5 x 16 as shown in Fig.5.16 (b). In quarter region of one group, the aperture positions were numbered as lines 1-8 (L1-8) and as columns 3-5 (C3-5).

The electric fields in each aperture position, which were generated by the all beamlets' space charge, are also shown in Fig.5.16. As a simple approximation, it is assumed that the distance between beamlets is a pitch of apertures, X_0 in X and Y_0 in Y. The electric field generated by all beamlets' space charge, E_X and E_Y, were normalized by electric field from next beamlet's space charge in X and Y, E_{X0} and E_{Y0}. These are expressed as follows.

$$E_{X0} = \frac{q}{4\pi\varepsilon_0 X_0^{\,2}} = C_0 \frac{1}{X_0^{\,2}}, E_{Y0} = \frac{q}{4\pi\varepsilon_0 Y_0^{\,2}} = C_0 \frac{1}{Y_0^{\,2}} \quad \text{--- (6)}$$

The maximum E_X and E_Y are obtained at the center beamlets in peripheral column and line. In this calculation model shown in Fig.5.16 (a), the maximum *Ex* and *Ey* are $3.7E_{X0}$ at C10-L3 and $4.2E_{Y0}$ at C6-L5, respectively. In the 500 keV H^- accelerator for the ITER NB, the maximum *Ex* and *Ey* are $3.4E_{X0}$ at C5-L1 and $3.9E_{Y0}$ at C3-L8, respectively.

In figure 5.17, the deflection angles δ by a space charge repulsion of (1) 500 keV, 200 A/m^2 D^- and (2) 340 keV 110 A/m^2 D^- as shown in Fig.5.9 and (3) 340 keV 130 A/m^2 D^- in this calculation model were plotted as function of electric field as shown in Fig.5.16 (a). In the approximate straight lines against E_X *and* E_Y, the proportional constants were (1) 1.49, (2) 1.43 and (3) 1.67 in deflection angle in X and (1) 1.38, (2) 1.35 and (3) 1.61 in deflection angle in Y. The deflection angles under the same perveance as (1) and (2) showed the same linearity. The ratio of proportional constant between (2) and (3) was the same as the ratio of current density, 1.18. That is, the deflection angle by the space charge repulsion was a proportional to beam current at the same beam energy.

The effect of mass of beam species to beamlet's space charge repulsion could be considered as follows [5.9), 5.10)]. The electric field generated by one beamlet's space charge, *Er*, is proportional to beam current and $\sqrt{m}$ (m is mass of beam species). Extracted beam current is proportional to $V^{1.5}/\sqrt{m}$ (V is acceleration

voltage) according to Child-Langmuir law. From these, the electric field generated by H^- ion beam and D^- ion beam can be expressed as follows.

$$\begin{aligned} & Er(H^-) : Er(D^-) \\ & = I_{H-}\sqrt{m_{H-}} : I_{D-}\sqrt{m_{D-}} \\ & = V^{1.5} / \sqrt{m_{H-}} \cdot \sqrt{m_{H-}} : V^{1.5} / \sqrt{m_{D-}} \cdot \sqrt{m_{D-}} \\ & = 1 : 1 \end{aligned} \quad \text{--- (7)}$$

This shows that the *Er* does not change due to the mass when the extracted beam current is decided by the Child-Langmuir law. In the 500 keV H^- accelerator for the ITER NB, the design value of H^- current density is 335 A/m^2. From Eq. (7), the deflection angle by space charge repulsion and proper aperture offset can be estimated by using the converted current density from H^- to D^-, 236 A/m^2 (=335 A/m^2 × $\sqrt{m_{H-} / m_{D-}}$).

Then, the proportional constant for the 500 keV H^- accelerator for the ITER NB can be estimated as the product of the proportional constant of (1) and ratio of current density, 1.28 (= 236 A/m^2 / 200 A/m^2). At results, the proportional constant of the 500 keV H^- accelerator for the ITER NB were 1.9 in X and 1.7 in Y as shown as (4) in Fig.5.17. The maximum deflection angle was estimated to 6.4 mrad ($E_X = 3.4E_{X0}$) in X at C3-L1 and 6.7 mrad ($E_Y = 3.9E_{Y0}$) in Y at C1-L8. To compensate these beamlet deflections, the proper aperture offsets could be obtained as to be 0.73 and 0.77 mm from Eq. (5). In Fig.5.18 (a), the aperture offsets in the ESG to compensate only beamlet deflection due to space charge repulsion are shown.

The deflection angle by the magnetic field is proportional to $1/\sqrt{m}$. Then, deflection angle by magnetic field for 500 keV H^- ion beam can be estimated as the production of the deflection angle of D^- ion beam shown in Section 5.4.2 and $\sqrt{m_{D-} / m_{H-}}$. That is 4.6 mrad x 1.414 = 6.5 mrad in X direction. To compensate this beamlet deflection, proper aperture offset was 0.75 mm from Eq. (5).

Finally, aperture offset for compensation of beamlet deflection by both the space charge repulsion and the magnetic field could be estimated. The maximum aperture offsets in all beamlets were obtained at peripheral apertures. They were about 1.5 mm in X at C3-L1 and about 0.8 mm in Y at C1-L8. Fig.5.18 (b) shows the aperture offsets in the ESG to compensate the beamlet deflections due to both space charge repulsion and dipole magnetic field.

As indicated in Chapter4, acceptable distance of aperture offset in the ESG with a diameter of 17 mm could be within 1 mm if the pitch of apertures in X is fixed to be 20 mm. In order to make the aperture offset to be less than 1.0 mm, the field correction plate is useful as the additional compensation technique for peripheral beamlets. Ref.5-3) showed that the field correction plate with 1 mm in thickness could steer the beamlet to 4 mrad. When the field correction plate with thickness of 1 mm was attached at the backside of the ESG, the aperture offset at peripheral aperture can be suppressed to be 1.0 mm. Fig.5.18 (c) shows the aperture offsets in the ESG with the field correction plate (thickness of 1 mm).

Fig.5-19 shows the aperture offsets in the ESG in Y direction.

5.4.4-2 Beamlet focussing to RID exit

As shown in Fig.5.20, aperture offset in GRG in the three stage 500 keV H^- ITER accelerator was estimated from eq.(6). As shown in 5.4.3, the focal length from GRG to the exit of RID is 7259 mm. When the gap between the A2G and the GRG was 68 mm, $\delta x1$ = 4.5 mm and $\delta x2$ = 2.2 mm. When this gap between A2G and GRG was set to the same gap length to that between A4G and GRG in the original five stage D^- accelerator, 50 mm, $\delta x1$ = 3.3 mm and $\delta x2$ =1.7 mm. It seems that aperture offset $\delta x1$ of more than 3 mm is relatively large against the aperture diameter of 16 mm. This may require further study to shorten the aperture offset, for example, by combination of smaller aperture offset at the ESG and the GRG.

5.5 Summary of beamlet steering

In the three stage 500 keV D^- accelerator model, the beamlet deflection were studied in detail and aperture offset in the ESG was examined utilizing 3D beam calculation code. Then, the aperture offset to compensate the beamlet deflection and to steer the beamlet to focal point in the three stage 500 keV H^- accelerator for the ITER NB was extrapolated and estimated. The exact aperture offsets in the three stage 500 keV H^- ITER NB accelerator was clarified. The results are summarized as follows.

- Aperture offset in the ESG is effective to compensate all beamlet deflections by space charge repulsion.
- Beamlet deflection by space charge is independent of the beam energy when the perveance is maintained.
- When magnetic field in the extraction region was applied, it was confirmed by the present analysis that the aperture offset of 0.5 mm is enough to compensate the beamlet deflection of 500 keV D^- ion beam. This is consistent with the previous experimental results, and original design. Even in beam with lower energy like 340 keV, the beamlet deflection angles can be suppressed to < 1 mrad with the aperture offset of 0.5 mm.
- The deflection angle and the aperture offset in 500 keV H^- three stage accelerator for the ITER NB were estimated. The deflection angles by space charge repulsion are about 6.5 mrad at the maximum, and the required aperture offset to compensate this beamlet deflection is 0.75 mm. The deflection angle by the magnetic field is 6.5 mrad. Proper aperture offset is also 0.75 mm. Totally, aperture offset of 1.5 mm is required at the maximum.
- To suppress the distance of aperture offset to be less than 1.0 mm, it is necessary to use both of aperture offset and field correction plate for the beamlets in the peripheral apertures.
- Required aperture offset in the GRG to focus the beamlets to the RID exit is estimated to be more than 3 mm from thin lens theory. This seems relatively large against the diameter of apertures in the GRG. This may require further study to shorten the aperture offset, for example, by combination of smaller aperture offset at the ESG and the GRG.

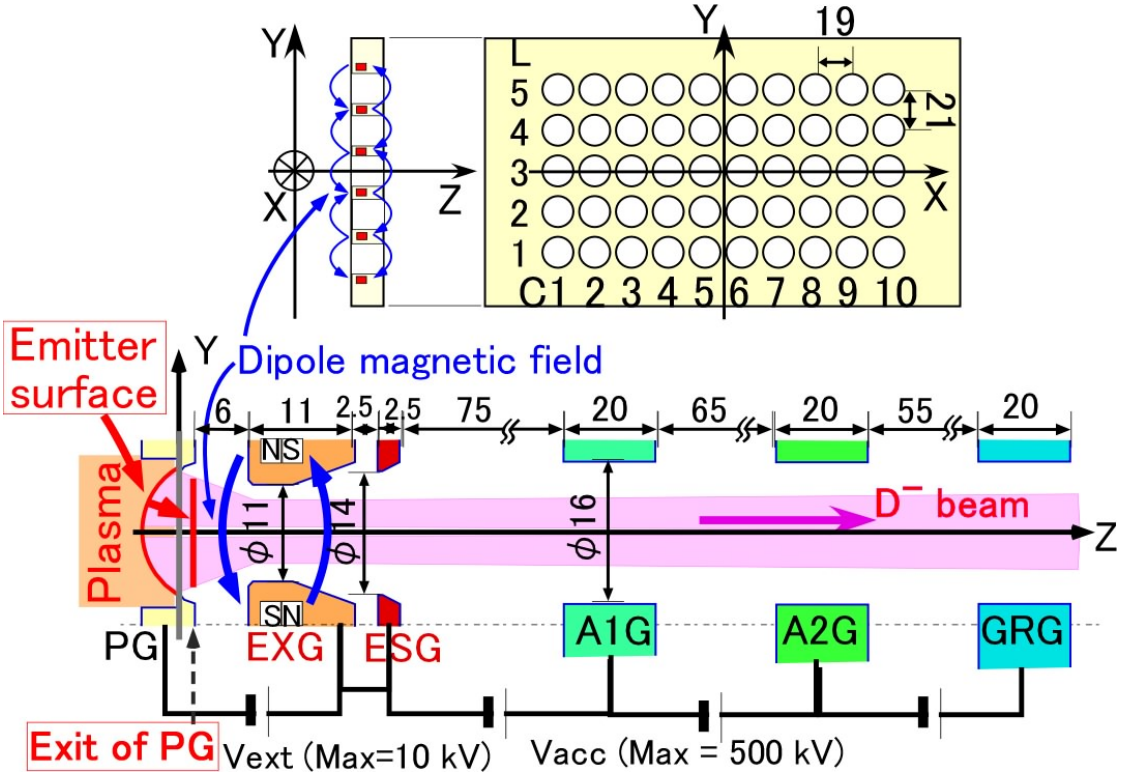

Fig.5.1. Calculation model of multi apertures and three stage accelerator.

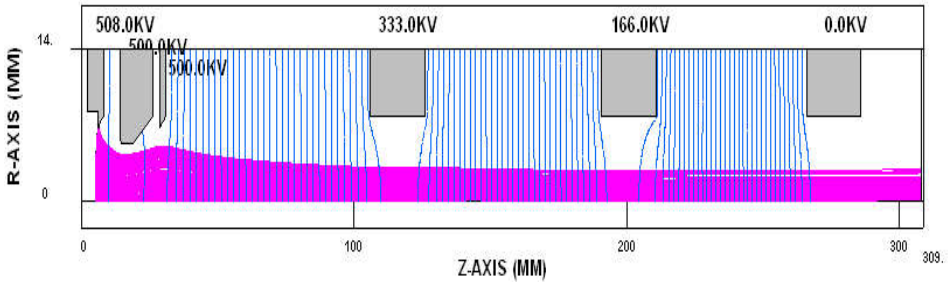

Fig.5.2. Beam trajectory in 2D beam code, BEAMORBT.
Vacc = 500 kV, Vext = 8 kV and J_{D-} = 200 A/m^2.

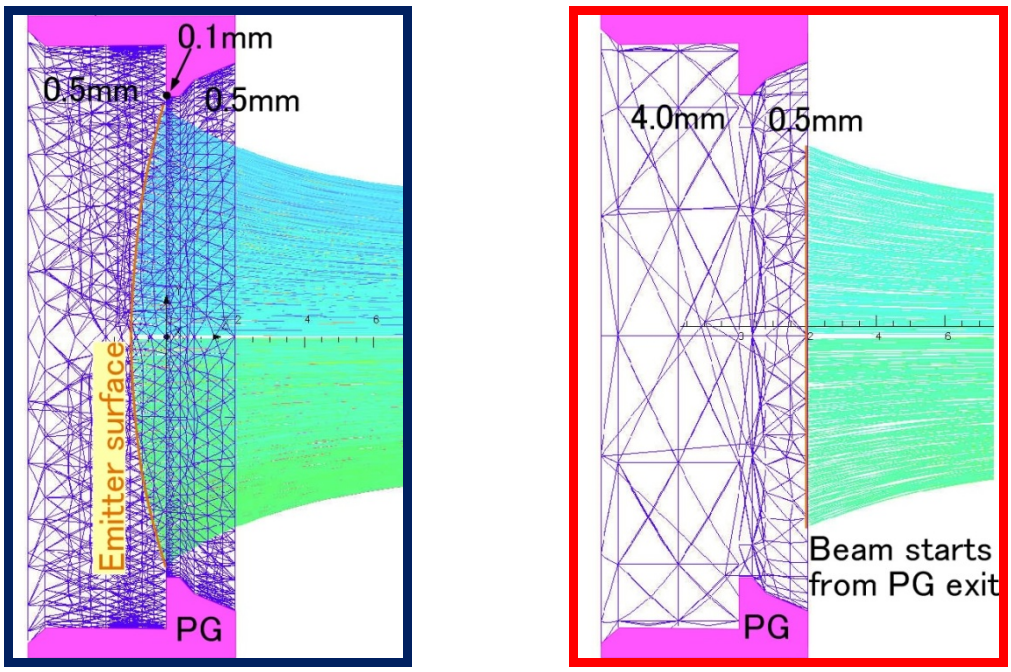

(a) (b)

Fig.5.3. Beam trajectories and mesh near PG in OPERA-3d.
Beam particles start from (a) emitter surface and (b) plasma grid exit,
where initial particle position and velocity are transferred from Fig.2.

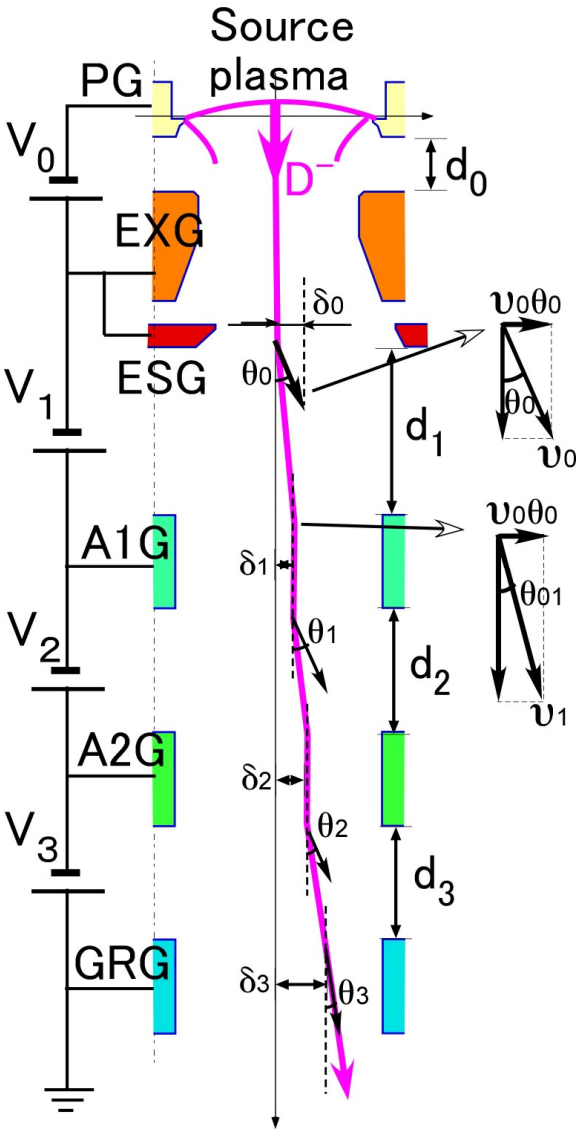

Fig.5.4. Steering angle in three stage negative ion accelerator when the aperture offset is applied in ESG.

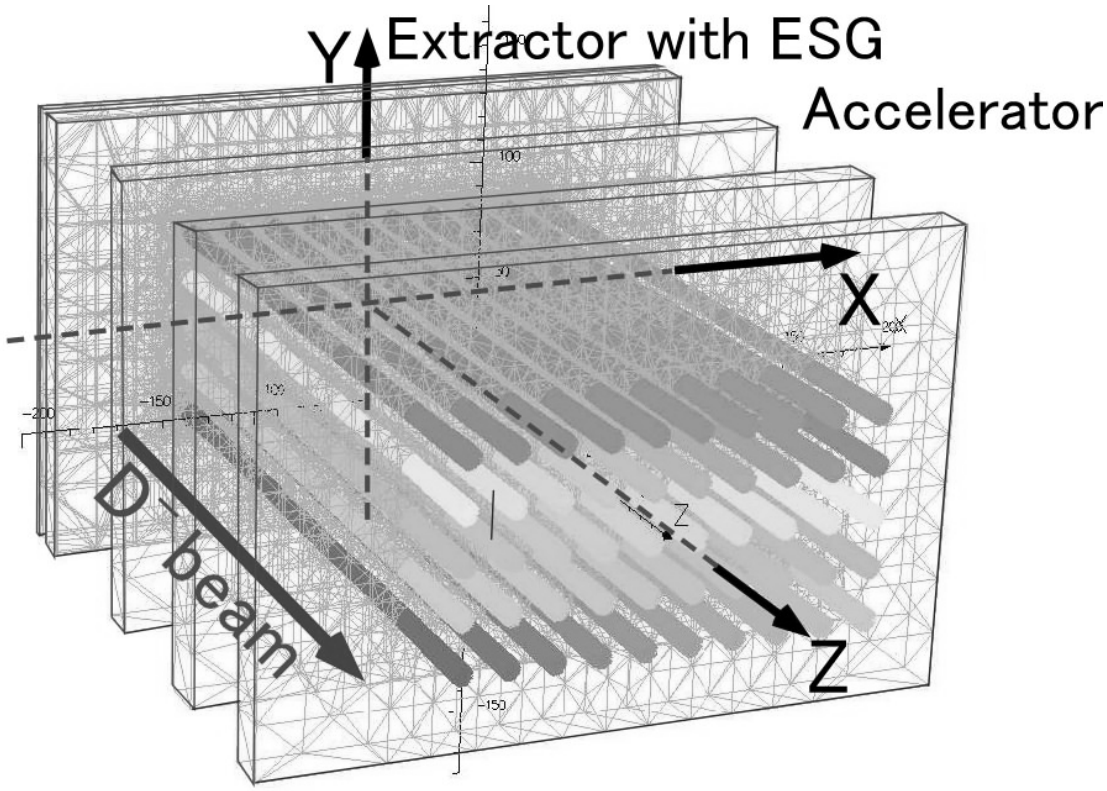

Fig.5.5. Fifty beamlets in the three stage accelerator without aperture offset.

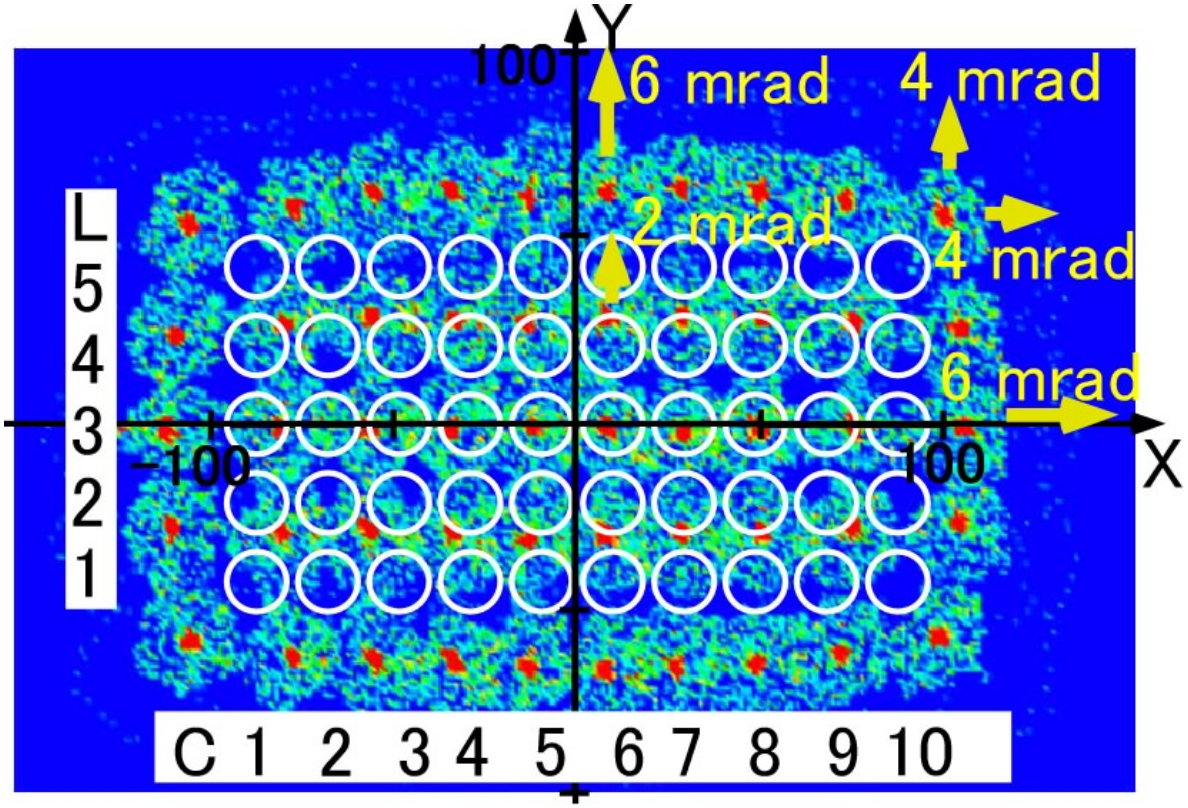

Fig.5.6. Calculated beam footprint at 3.5 m downstream from GRG before setting aperture offset. Red points indicate the center of each beamlet at the downstream, whilst the white circles represent the original position of the apertures. The beamlets are deflected outward.

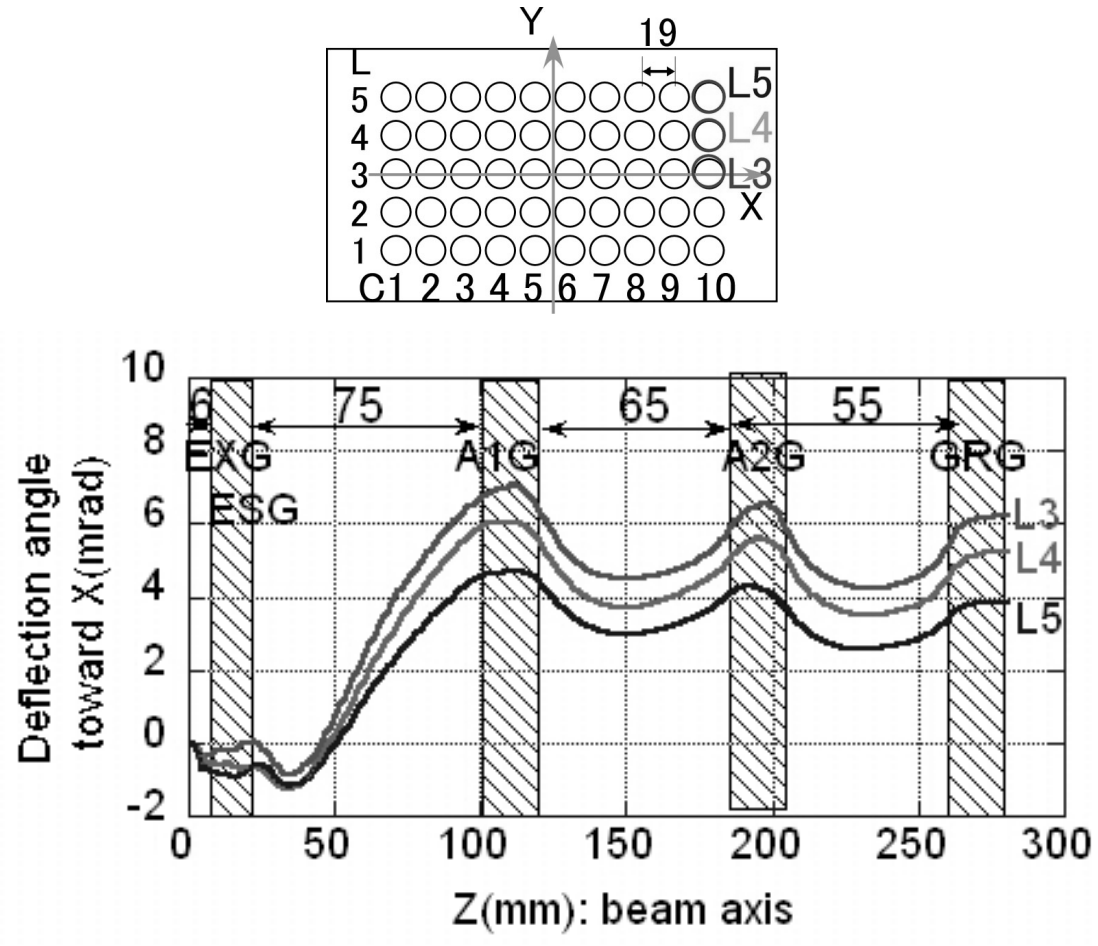

Fig.5.7. Change of deflection angle of beamlet center in the accelerator.

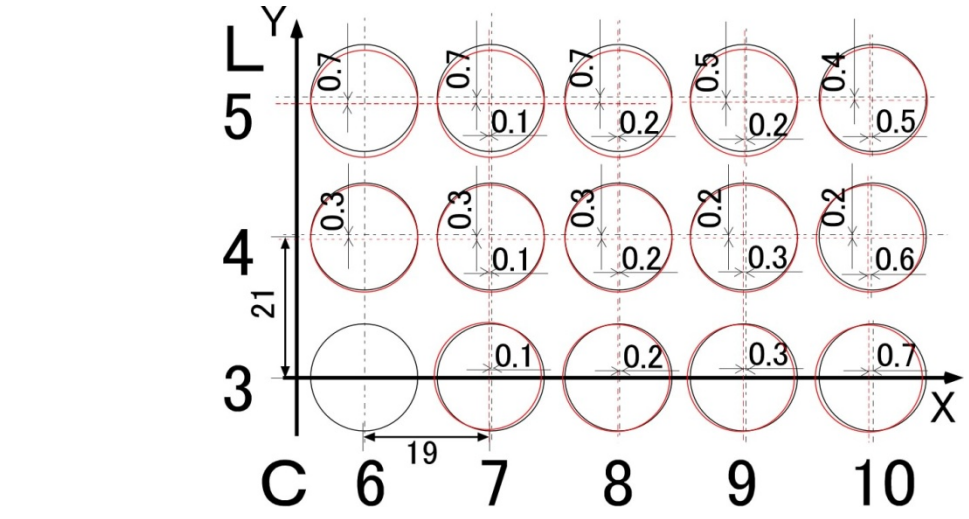

(a)

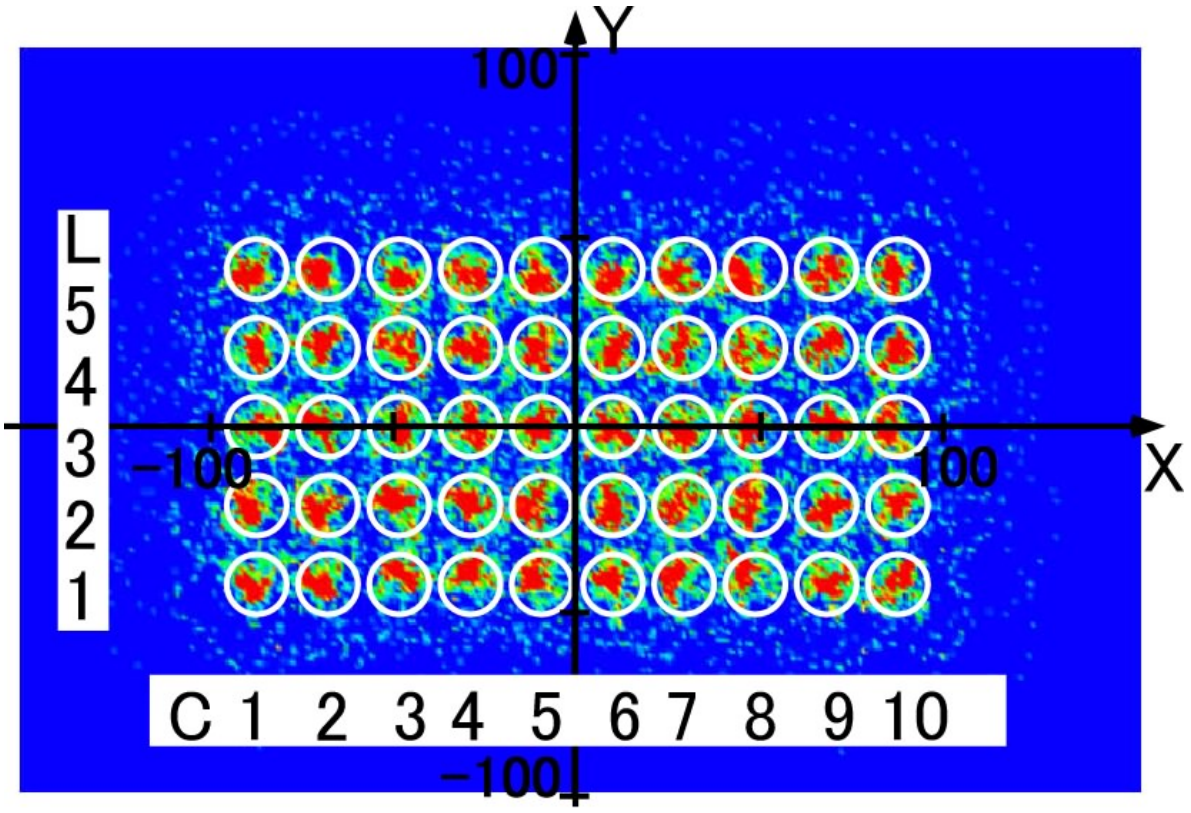

(b)

Fig.5.8. Calculated beam footprint after proper aperture offset.

(a) Proper aperture offset. (b) Calculated beam footprint after proper aperture offset.

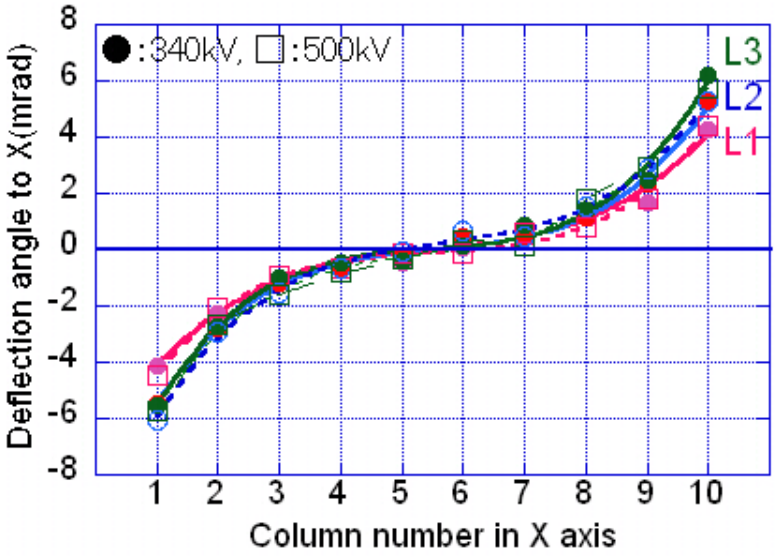

(a)

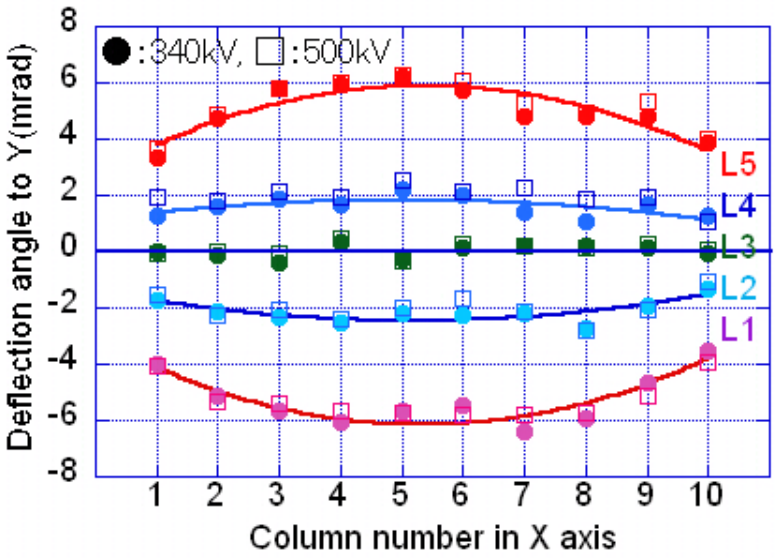

(b)

Fig.5.9. Deflection angle of 340 keV, 110 A/m^2 D$^-$ ion beam shown in Fig.7 and 500 keV, 200 A/m^2 D$^-$ ion beam. The perveance is maintained in these two beam conditions. Deflection angle in (a) X and (b) Y.

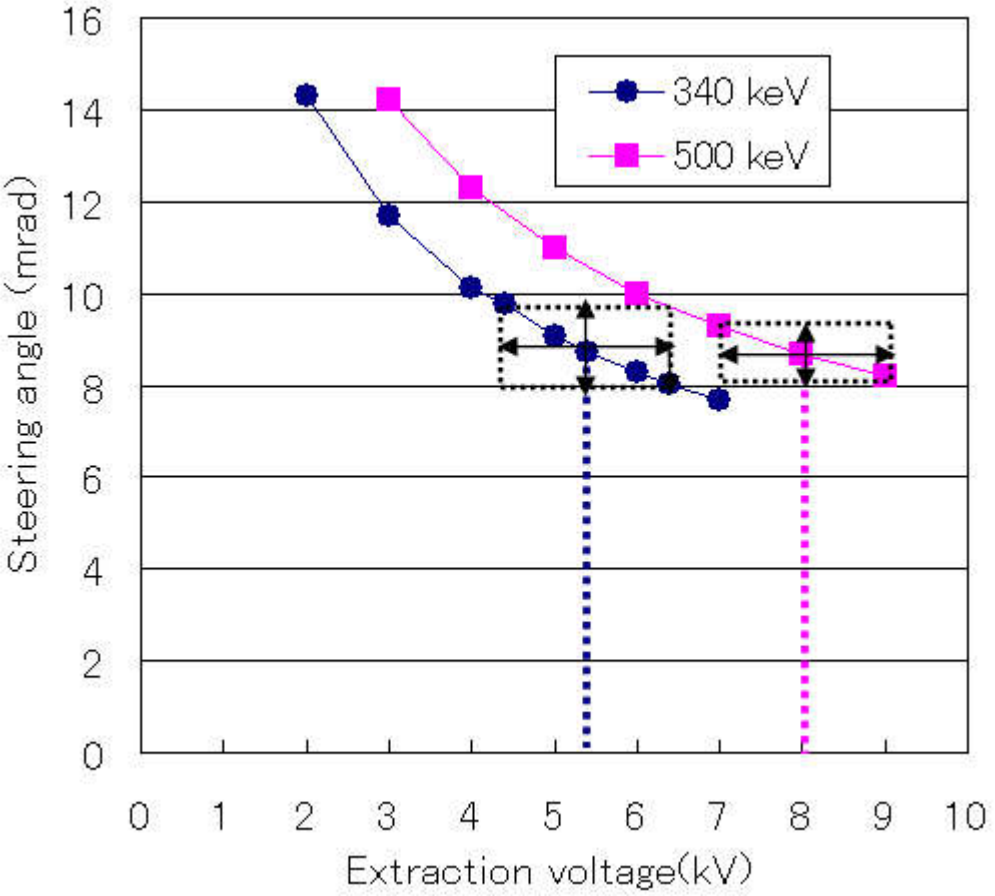

Fig.5.10. Steering angle due to aperture offset v.s. extraction voltage.

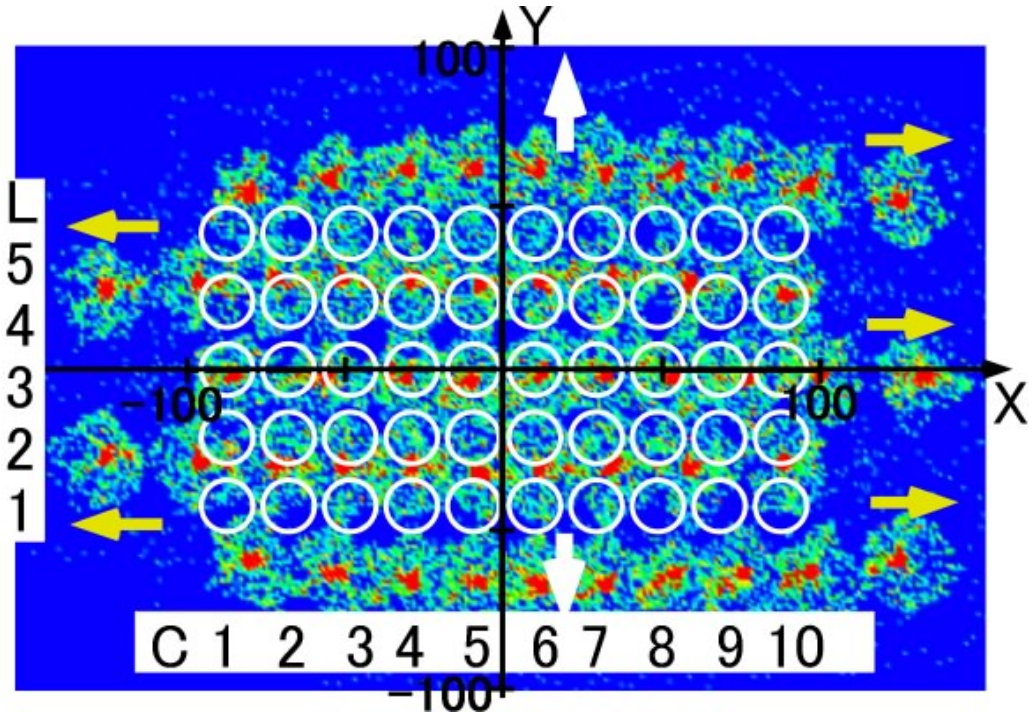

Fig.5.11. Calculated beam footprint without aperture offset.
Beamlet is deflected by not only space charge repulsion
but also magnetic field in the extractor.

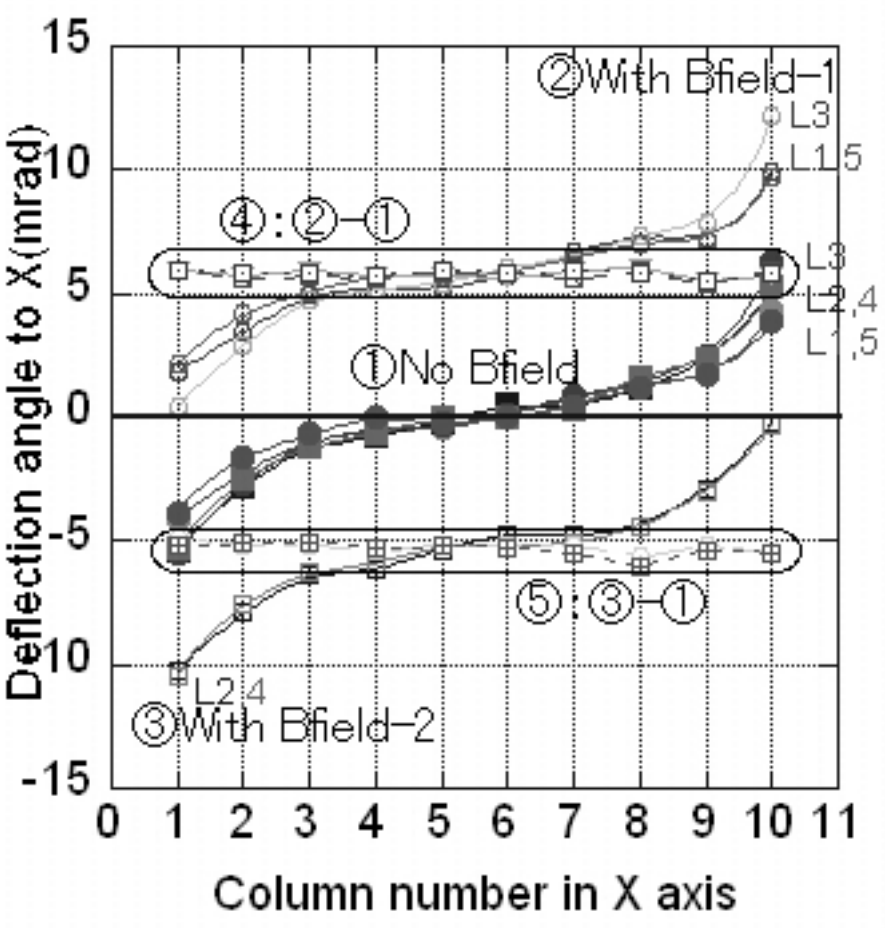

Fig.5.12. Deflection angle in X direction.

Difference of deflection angle between ①without and ②③with magnetic field is about 5.4 mrad (④⑤) in all beamlets.

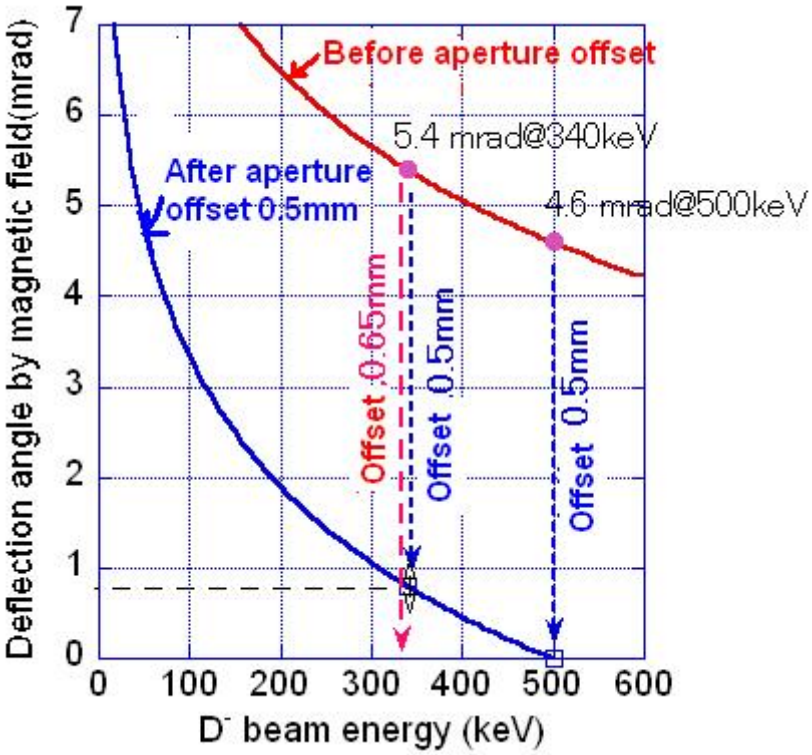

Fig.5.13. Deflection angle before and after the aperture offset of 0.5 mm under magnetic field. This aperture offset is properly to 500 keV beam.

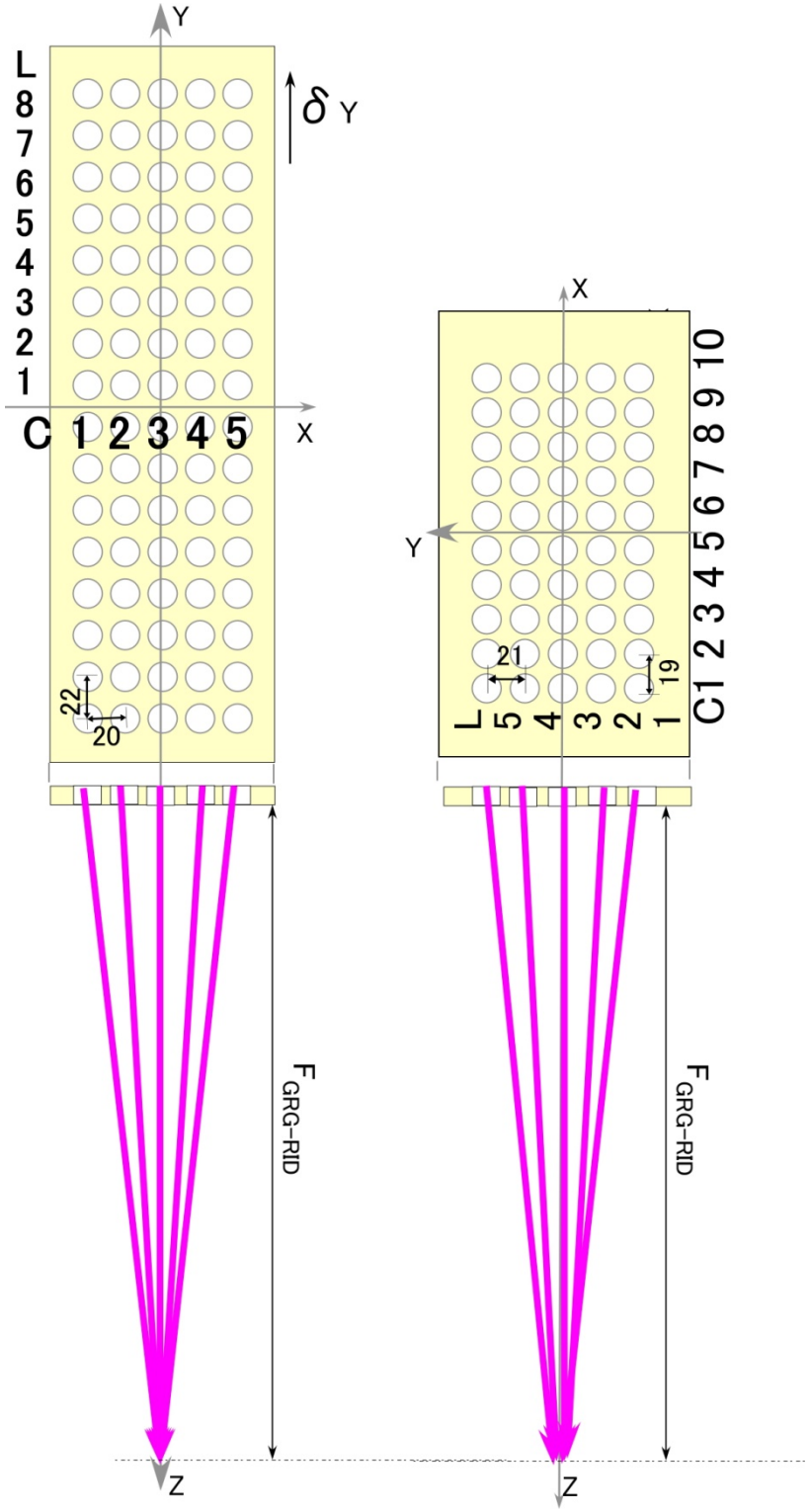

(a) (b)

Fig.5.14. Beam focusing to an exit of RID.

(a) in 500 keV H^- ITER NB accelerator and (b) in this calculation model.

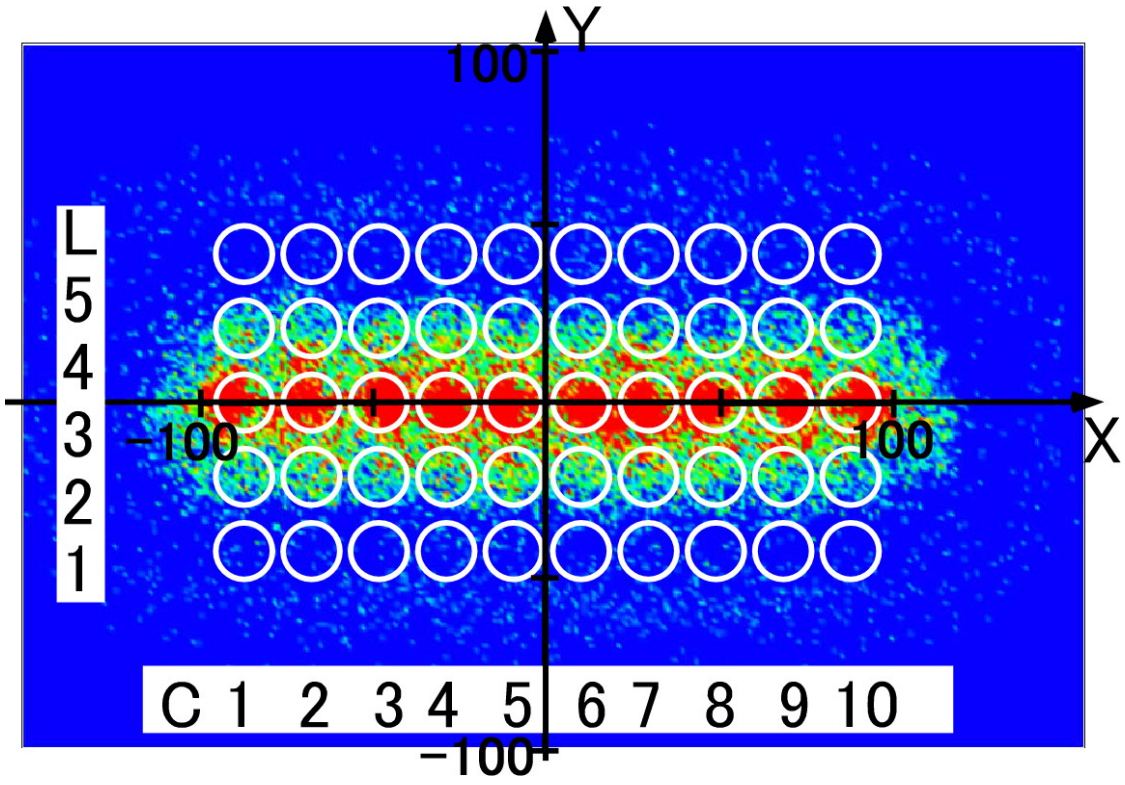

Fig.5.15. Calculated beam footprint at focal point, the exit of RID.
Beamlet deflections in the accelerator were compensated by aperture offsets in the ESG.
Then, aperture offsets in the GRG were applied to steer the beamlets toward the focal point.
White circles shows the original aperture positions in the GRG before aperture offset.

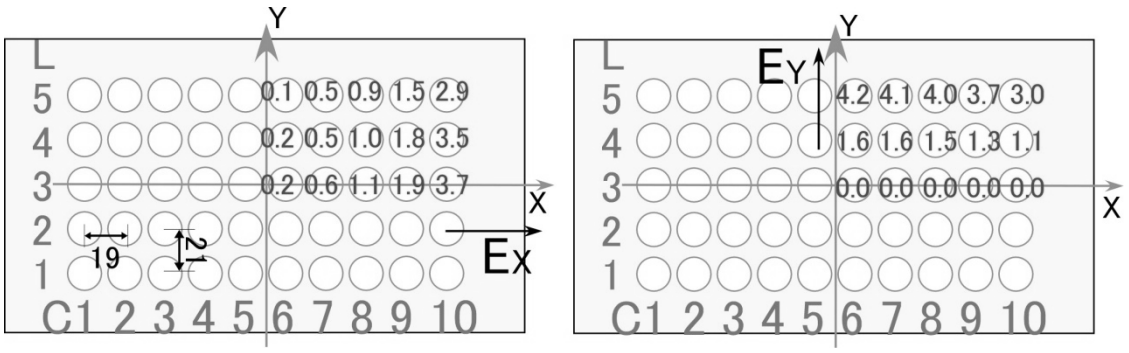

(a)

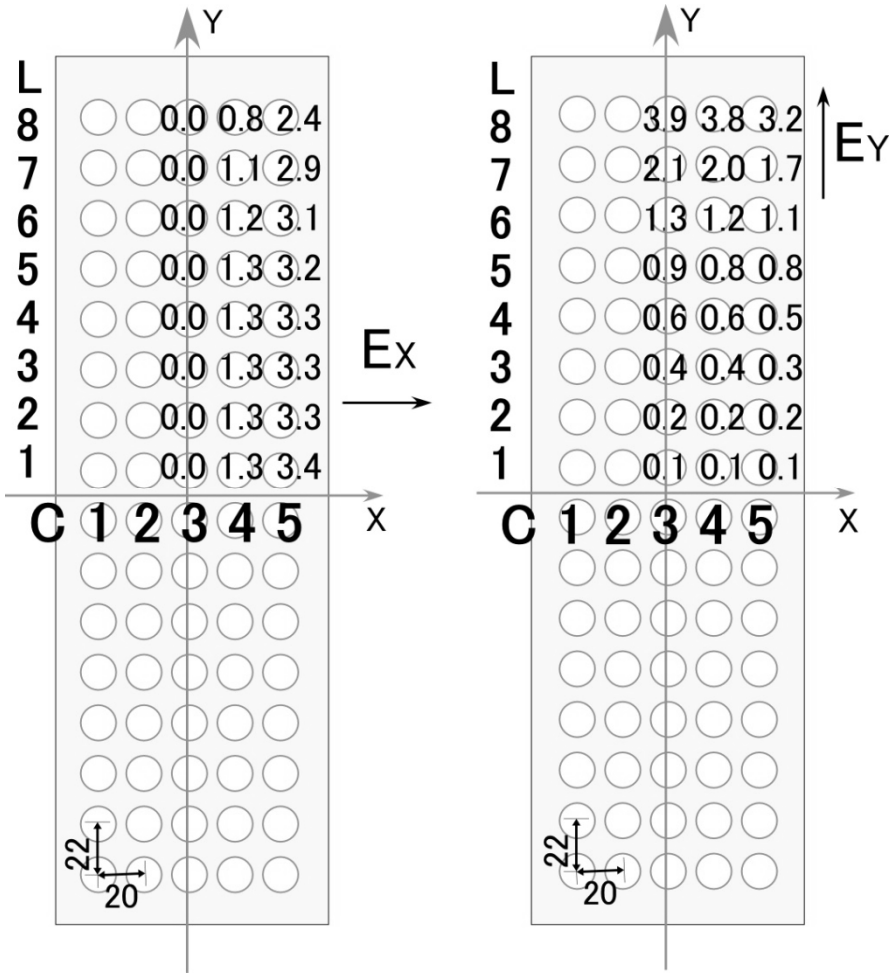

(b)

Fig.5.16. Electric field from all beamlets' space charge, E_X and E_Y, are normalized by electric field from next beamlet, E_{X0} and E_{Y0}.

Electric field (a) in this calculation model and (b) 500 keV H^- ITER NB accelerator.

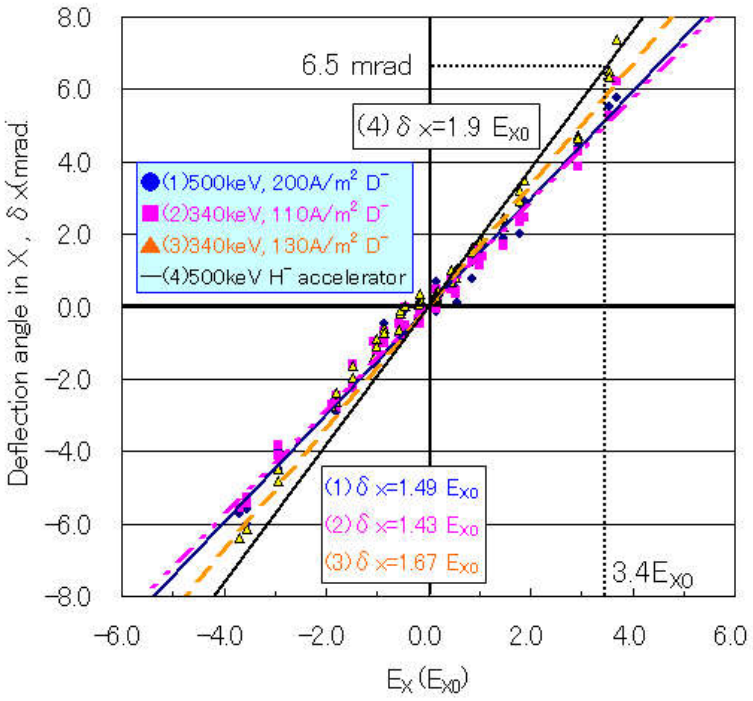

(a)

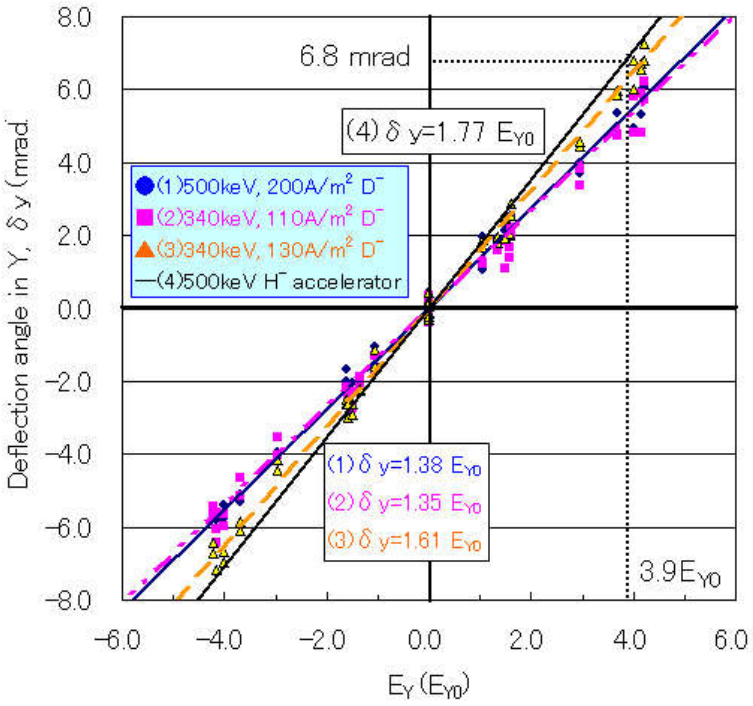

(b)

Fig.5.17. Deflection angles as a function of electric field from all beamlets' space charge.

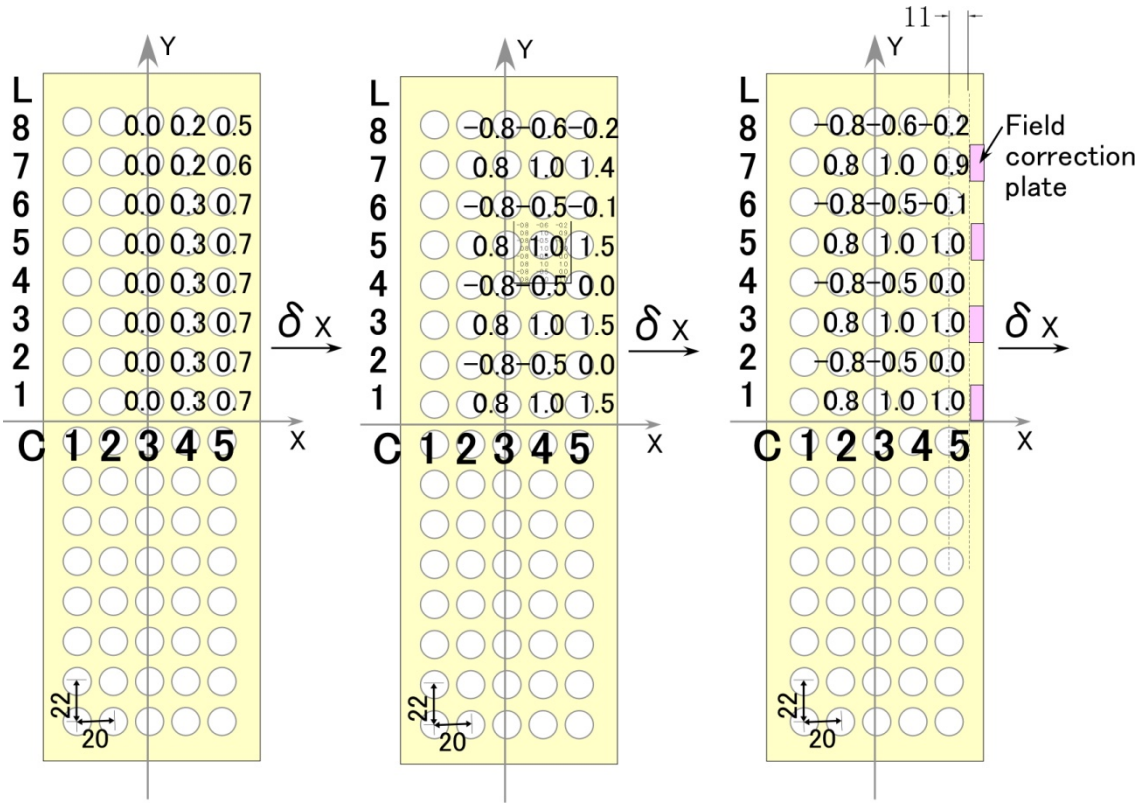

(a) (b) (c)

Fig.5.18. Aperture offset in X in the ESG in 500 keV H^- ITER NB accelerator.

(a) Aperture offsets for only compensation of beamlet repulsion, (b) aperture offset for compensation of beamlet deflection by space charge repulsion and the dipole magnetic field, and (c) aperture offset when field correction plate of 1 mm thickness is used.

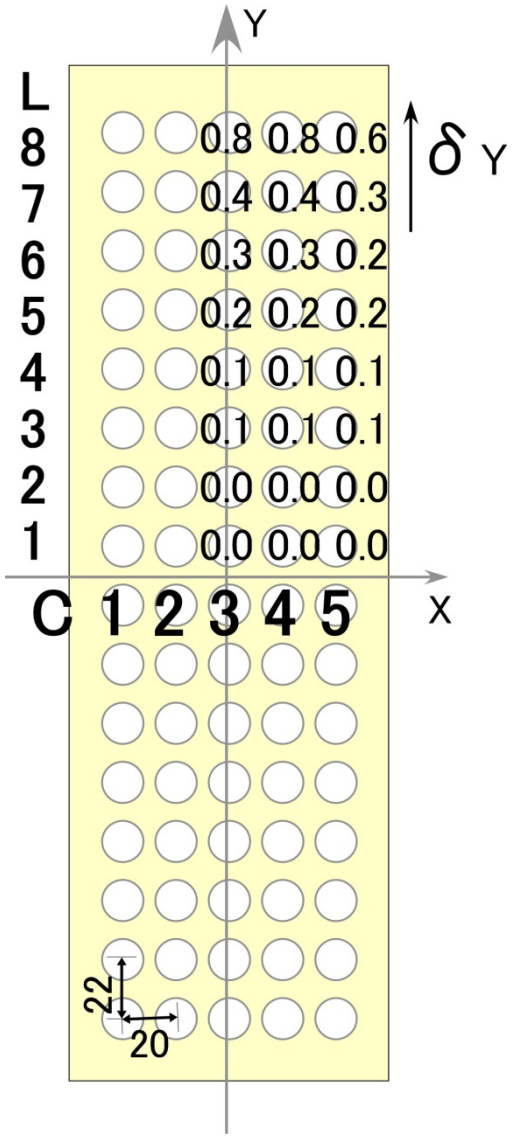

Fig.5.19. Aperture offsets in Y in the ESG.

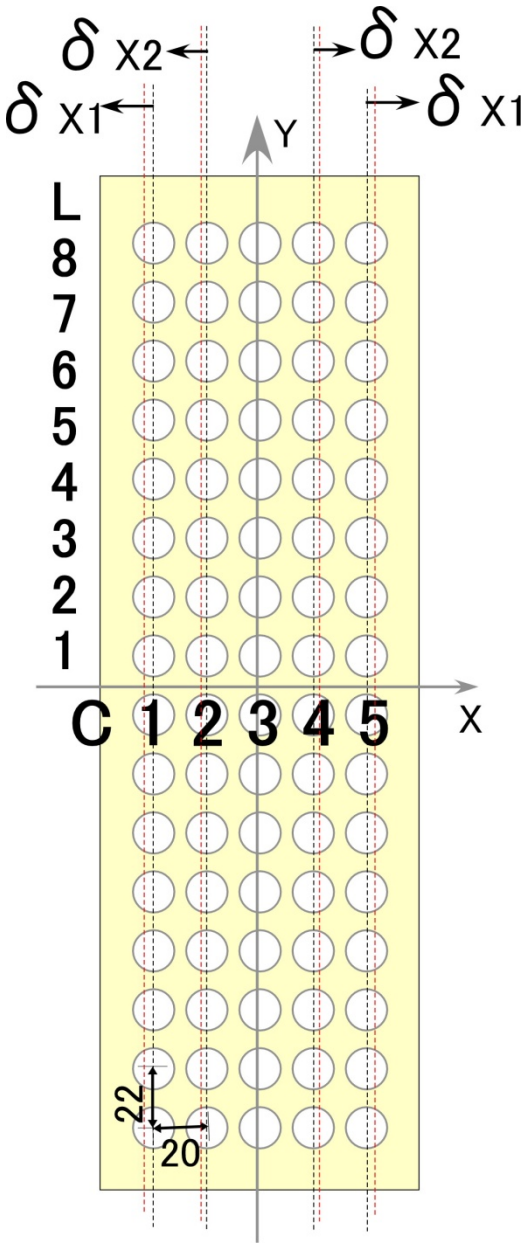

Fig.5.20: Aperture offset in the GRG to focus the beamlets at the exit of RID.
When gap length between A2G and GRG is 68 mm, $\delta x1$ = 4.5 mm and $\delta x2$ = 2.2 mm.
When gap length between A2G and GRG is 50 mm, $\delta x1$ = 3.3 mm and $\delta x2$ =1.7 mm.

6. Studies of gas density distribution and stripping loss of negative ions

6.1 Background

In the basic physics design study of 3 stage 500 keV H^- accelerator utilizing 2D beam analyses code, some modifications from the original accelerator configuration were proposed from viewpoints of beam optics. Main difference from the original configuration is a diameter of aperture in the extraction grid. That diameter is changed from 11 mm in the original to 14 mm. The issue due to the expansion of aperture diameter could be increase of stripping loss of negative ions because it was expected the gas flow increases in the accelerator with the larger apertures. In JAEA gas flow code [6.1, 6.2], gas distribution along beam path and around the vacuum insulation beam source (VIBS), and stripping loss of negative ions were analyzed in original accelerator configurations and the proposed one.

6.2 Calculation model

Figure 6.1 shows an outline view of the calculation model. In the beam source vessel, the constructions from a beam source (BS) to a midway of a gas neutralizer (GN) were included.

Figure 6.2 shows the calculation model of beam source. The beam source consisted of the plasma chamber, the plasma grid (PG), the extraction grid (EXG), the electron suppression grid (ESG), 1 st and 2 nd acceleration grids (A1G and A2G) and the grounded grid (GRG). Each grid was supported by grid support frames and mounting flanges. Mounting flanges were supported by cylindrical ceramic insulators, namely, post insulators. The gas injected from top of the beam source flows into grid apertures or in gaps between grid supports, and then is absorbed to cryopump. To model the gas temperature inside discharge plasma, the initial temperature of gas and the chamber wall temperature were set to 1000 K. The temperature of plasma grid was assumed to be 593 K. The other wall temperature was adjusted to be 313 K. The accommodation factor was set to 0.3 [6.1, 6.2].

Figure 6.3 shows the apertures arrangement. There were sixteen groups arranged in 4 x 4 square lattice patterns. In each group, 80 apertures were drilled in a lattice pattern of 5 x 16. The total number of apertures was 1280. The gas densities in R11, R12, R21 and R22 in Fig.6.3 were obtained as an average of symmetrical four positions because this VIBS had a symmetrical configuration to X and Y axes. The stripping loss was obtained along the beam path in apertures located at R11, R12, R21 and R22.

Figure 6.4 shows the calculation model of gas neutralizer with 4 channels. Gas was injected from 20 holes of 4 mm in diameter at the midway of neutralizer [6.3]. The mirror boundary was set to slightly (4 mm) downstream from the midway of neutralizer in order to save the number of particles. The initial gas temperature was set to 313 K. The wall temperature was set to 313 K. The gas from the neutralizer flows inside accelerator or around VIBS, and then reached to the cryopump.

The cryopump was positioned along the inner wall of the vacuum vessel (beamline vessel) wall as shown in Fig.6.1. The cryopump was simplified as a simple surface with adsorption probability of 0.2 and 80 K as the surface temperature [6.1)].

In this study, two types of three stage accelerator, namely Model 1 and Model 2, were examined. Model 1 has the same configuration of the extractor and the A1G and the A2G and the A3G in the original five stage accelerator. In Model 2, which is proposed one in the basic physics study in Section 3, diameter of the EXG aperture and gap lengths were modified. Table 6.1 shows the difference between Model 1 and Model 2. The diameter of aperture in the extraction grid was changed from 11 mm to 14 mm to obtain better beam optics. The gap distance between the PG and the EXG was changed from 6 mm to 5 mm to extract much higher dense negative ions. The acceleration grid thickness was changed from 20 mm to 10 mm to decrease secondary electrons as another proposal from the physics design study.

6.3 JAEA 3D gas analyses code

JAEA three dimensional Monte Carlo gas flow analyses code (JAEA gas flow code) [6.4)] can takes into account the following features.

- Three dimensional configuration of device
- Initial gas temperature with the Boltzmann distribution.
- Incident angle at gas injection or reflection angle at wall of gas particle following to the Cosine's law.
- Interaction with wall (accommodation factor, absorption probability)

As the results of the analysis, gas density, gas temperature and stripping loss of negative ions are obtained. In the simple calculation model like a cylinder with orifice and single aperture multi grids accelerator model, it was confirmed that the gas distributions obtained by this gas flow code showed good agreement with ones in theoretical estimation.

This code has been applied to the ITER accelerator design works [6.1, 6.2)]. In these works, the calculation model was made simplified because of limitation in computer resources and much complicated configurations such as multi apertures and grid support structures in the VIBS. For this simplicity, the passing probability through the apertures was assumed instead of constructing detailed model of multi apertures, post insulators and so on.

In order to simulate the gas flow more in details and accurate, the preprocessing was improved when this code was converted from UNIX computer to Windows PC. The new preprocessing made possible to construct much easier the full and detailed 3D configuration of the ITER accelerator.

The cross section of calculation region was able to be confirmed in 3D view as shown in Fig.6.5. Fig.6.5 (a) shows the overview of this calculation model. The complicated grid support such as the support frames and the post insulators were included. The beam source and the neutralizer in the beam source vessel were included. Fig.6.5 (b) shows the apertures in the plasma and extraction grids. All apertures were included in this calculation model.

6.4 Results

6.4.1 Gas flow from the ion source

Figure 6.6 (a) shows a projection in YZ plane of trajectories of 1000 gas particles injected from top of the beam source. To check the gas flow in the beam source, the absorption surface was simply defined at the boundary between the beam source and surrounding vacuum like S1, S2, S3, S4, S5 and S6 as shown in Fig. 6.6 (b). The accelerator was the original five stage one. The numbers of particles, which escaped to S1, S2, S3, S4 and S5, were 443, 284, 118, 55 and 22, respectively. The number of particle, which reached the accelerator exit, S6, was 78. Thus the number of particles escaping between support flange of top and A1G, A1G and A2G, and A2G and A3G, were relatively larger than that through the accelerator exit.

Figure 6.7 shows the particle distribution when the number of particles was increased to 10000, 50000, 100000. When the number was more than 50000, increase of the density distribution was saturated. Therefore, 100000 gas particles were traced from the beam source.

Figure 6.8 shows the projection of trajectories of 100 gas particles from 1 hole in left channel of neutralizer. It is shown that the gases expanded widely in the beam source vessel. In the gas density calculation, 60000 particles from 1 hole, totally, 240000 particles from the neutralizer were injected and traced.

6.4.2 Gas density distribution in the accelerator

The gas density profiles in Model 1 and 2 along four beam paths R11, R12, R21 and R22 are shown in Fig.6.9 (a) and (b), respectively. To clarify the difference due to the diameter of the EXG aperture, the gas was injected only from the beam source. A horizontal axis is a distance from the plasma grid to downstream. In both models, the gas density was different depending on the aperture positions (R11, R12, R21 and R22) in the large beam extraction area. The gas density was highest in the center region (R11) and was lowest in the periphery (R22). The gas density decreased gradually and became about 1.0×10^{12} cm^{-3} after GRG.

6.4.3 Gas density distribution with the 500 keV neutralisation target

Figure 6.10 shows the neutralization efficiency for 500 keV H^- ion beam against the gas line density [6.5, 6.6]. The optimum gas line density to obtain maximum neutralization efficiency was about 1.4×10^{16} cm^{-2}.

Figure 6.11 shows the gas density distribution to achieve this optimum gas line density. It was assumed that the gas profile along the beam path was symmetry to a midway of neutralizer. The gas pressure in midway of gas neutralizer was 0.34 Pa. The gas gradually decreases toward the entrance of neutralizer and became less than 5×10^{12} cm^{-3} between the GRG and the neutralizer entrance.

In order to confirm the Pd (gas pressure x insulation distance), which define voltage holding capability against glow discharge, the gas pressure distribution around the VIBS was calculated as shown in Fig. 6.12. The horizontal axis is a distance from top of the GRG mounting flange. The gas from the beam source decreased gradually as going to the downstream. The gas from the neutralizer was almost constant. Pd was 0.5×10^{-2} from beam source, 1.0×10^{-2} from neutralizer and totally 1.5×10^{-2} Pa m.

Figure 6.13 shows Pd in this calculation, which was indicated in figure 6.6 showing flashover voltage and Paschen curve as a function of Pd. It is confirmed that the Pd in the three stage accelerator was within the scope of the design values in the ITER NB accelerator [6.7)].

6.4.4 Calculation of stripping losses with the expected gas density in the accelerator

Figure 6.14 (a) and (b) shows the stripping losses in Model 1 and 2 under the gas distribution shown in Fig.6.9, respectively. In Model 1, the stripping loss was 21 % in R11 and 17 % in R22. In Model 2, the stripping loss was 21 % at R11 and 17 % at R22. Thus the stripping losses of Model 1 and 2 were almost the same. On the contrary, the difference of stripping loss due to the aperture position was large. The stripping loss in the corner of extraction region showed decrease of 4 % from that in the center.

Figure 6.15 (a) and (b) shows the gas temperature in Model 1 and 2. In Model 1, the gas temperature distributions at R11, R12, R21 and R22 were almost same. In Model 2, it was showed that the gas temperature were different at each position. The absolute value of gas temperature in Model 1 was lower than that in Model 2 in the extraction area. It can be considered that the gas confinement in the extraction region with smaller aperture in the ESG of Model 1 is better than that of Model 2. Then, the gas temperature became uniform in the large extraction area in Model 1. On the contrary, the gases escape easily from the extraction region in Model 2 with larger aperture in the ESG. Therefore, gas temperature shows the position dependence.

Figure 6.16 shows the stripping loss in Model 2 when gas was injected additionally from the neutralizer. The stripping losses showed small increased in all beamline of R11 to R22. However, there was no significant change in stripping loss from Fig.6.14 (b).

One of reasons why there was no significant difference in stripping loss in Model 1 and 2 was a large amount of gas flow to the gaps between grid supports as shown in Fig.6.6. In order to compare between Model 1 and Model 2 in detail, the gas density from center of plasma discharge chamber to the GRG at R11 in both models are shown in Fig.6.17 (a). As expected from larger diameter of the EXG aperture, the gas density in Model 2 was larger than that in Model 1 after the EXG. However, the gas density in Model 1 was larger than in Model 2 before extraction grid. It is considered that the gases were confined before extraction grid because of the smaller aperture. The slope of gas profile in the long acceleration gap were different between Model 1 and 2. It was caused by the difference of gas temperature distribution as explained in Fig.6.15. As the results, the stripping loss in Model 1 was slightly larger than that in Model 2 around the EXG as shown in Fig.6.17 (b). Expectations on the contrary, stripping loss in Model 2 was slightly lower around the EXG because the EXG aperture with larger diameter reduces the gas density before the EXG.

6.5. Summary of gas flow and stripping loss of negative ions analyses

In the design study of three stage 500 keV H^- accelerator, gas flow and stripping loss in two types of accelerator were analyzed. In the accelerator, downstream two grids were simply removed from the original five stage accelerator. In the other one, main modification from the original was to make the diameter of aperture in the EXG larger from 11 mm in the original to 14 mm. The results are summarized as follows.

- There was no significant change in the stripping loss between two accelerators.
- The stripping losses are 22 % in the center and 17 % in the periphery of the extraction region.
- Pd (Pa m) around VIBS, which define the high voltage holding capability of VIBS, satisfies with the design value.

Table 6.1. Difference between Model 1 and Model 2

	Model 1	Model 2
Diameter of aperture in EXG	11 mm	14 mm
Extraction gap length	6 mm	5 mm
Thickness of acceleration grid	20 mm	10 mm
Gap length between ESG and A1G	86 mm	88 mm

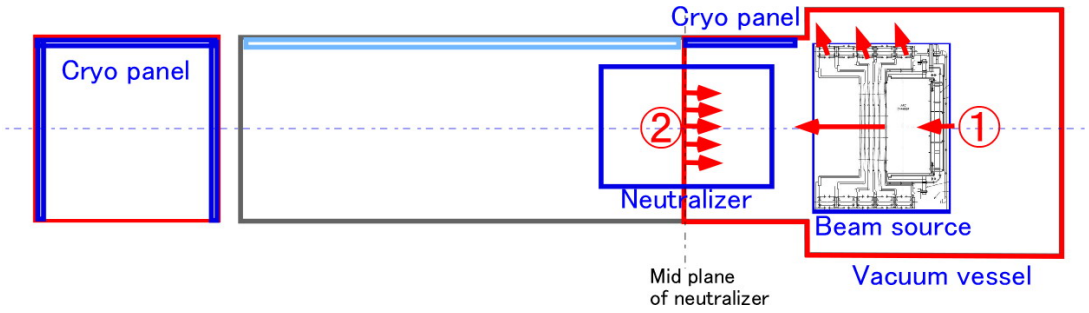

Fig.6.1 Outline of calculation region.

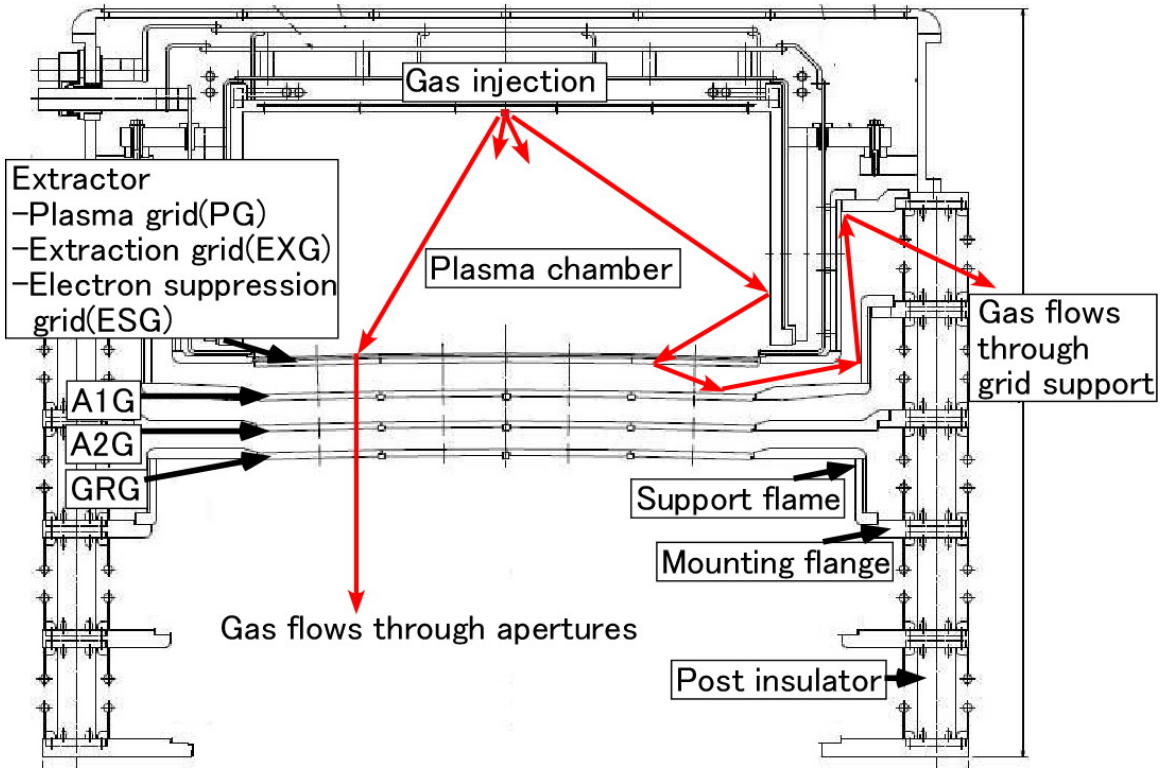

Fig.6.2 Calculation model of beam source.

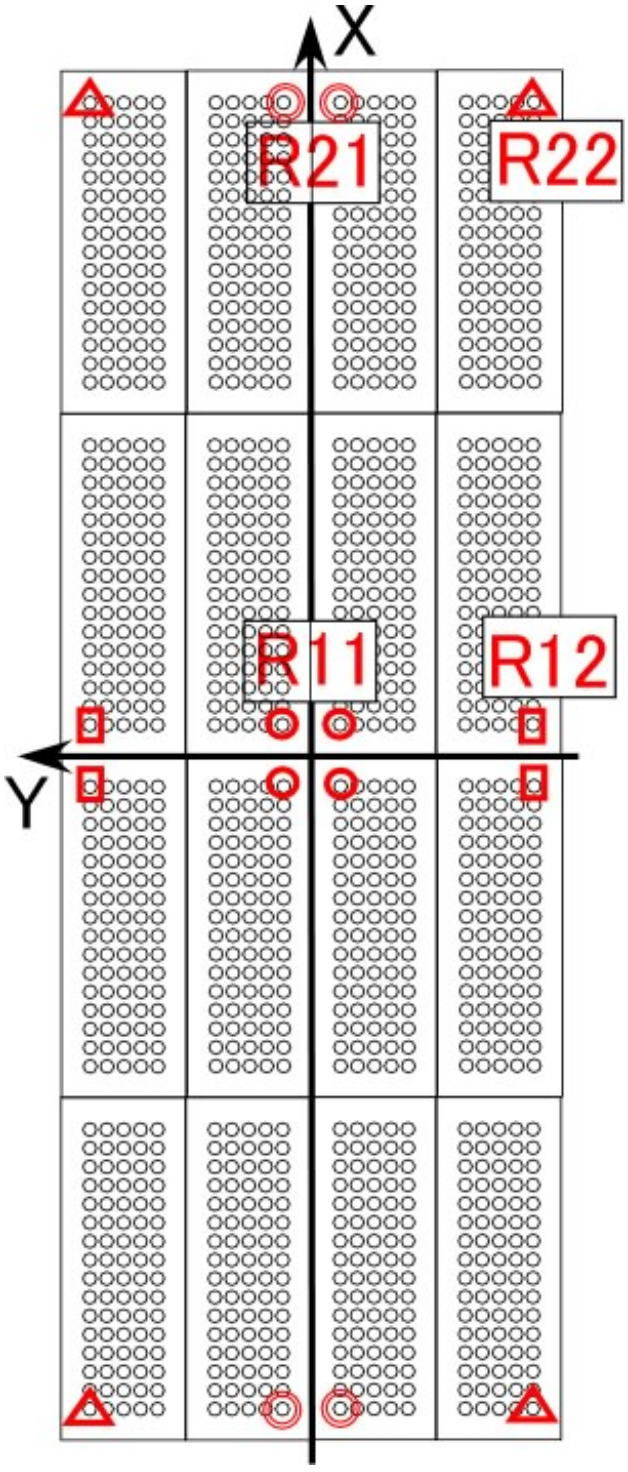

Fig.6.3 Aperture arrangement.

R11, R12, R21 and R22 regions are circled by ○, □,◎,△.

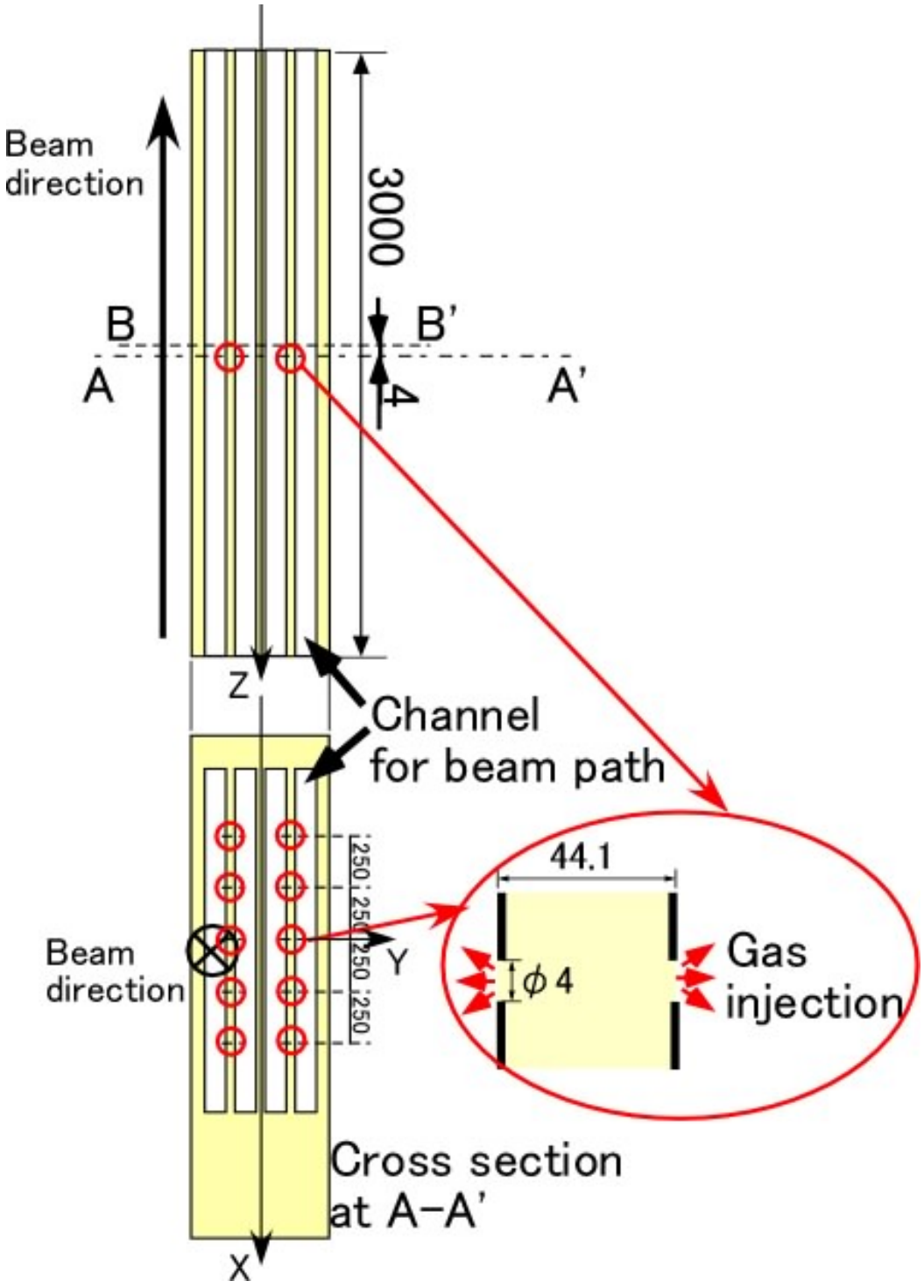

Fig.6.4 Calculation model of neutralizer

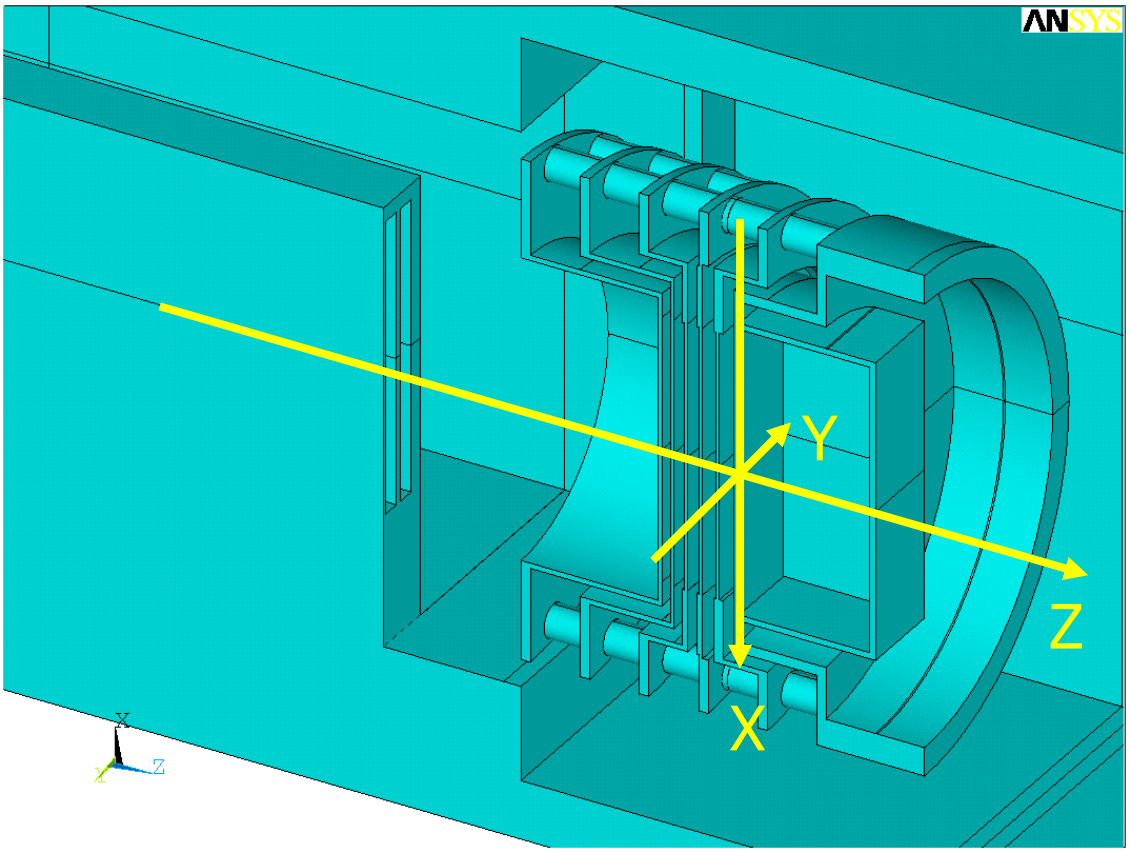

(a)

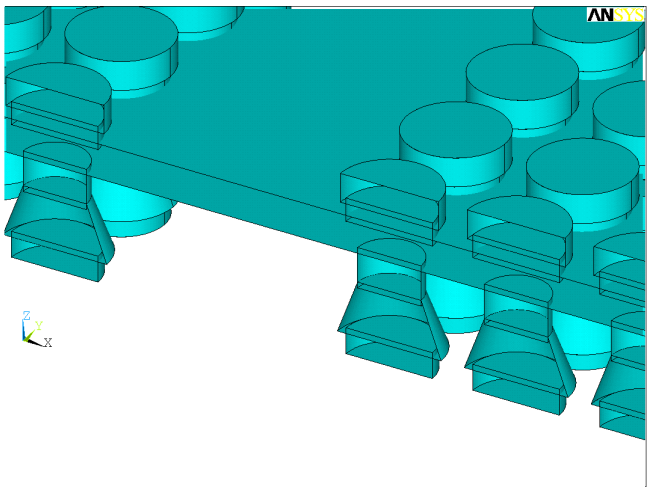

(b)

Fig.6.5. 3D view of calculation region in pre-processing of gas flow code.
(a) Overview of calculation region. (b) Apertures in the extractor.

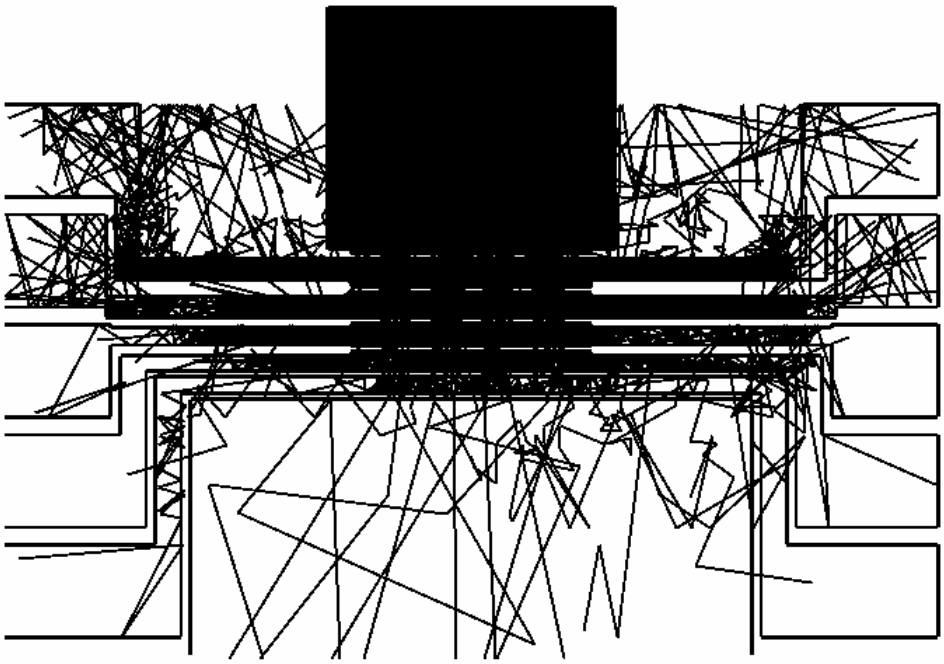

(a)

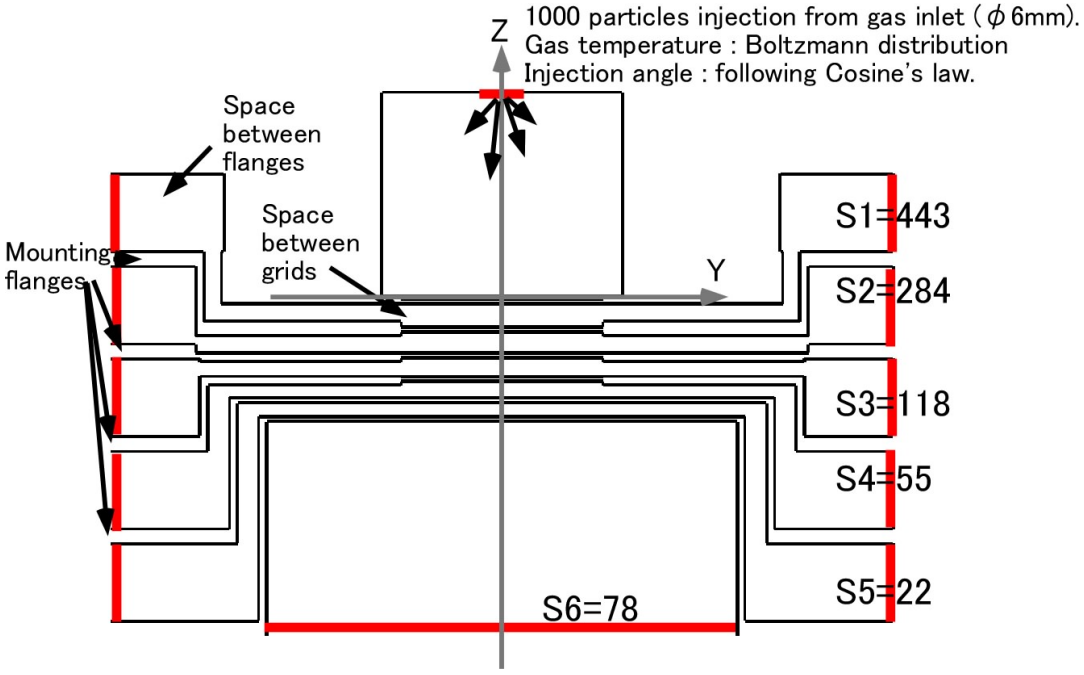

(b)

Fig.6.6 Trajectory of 1000 gas particles from beam source.

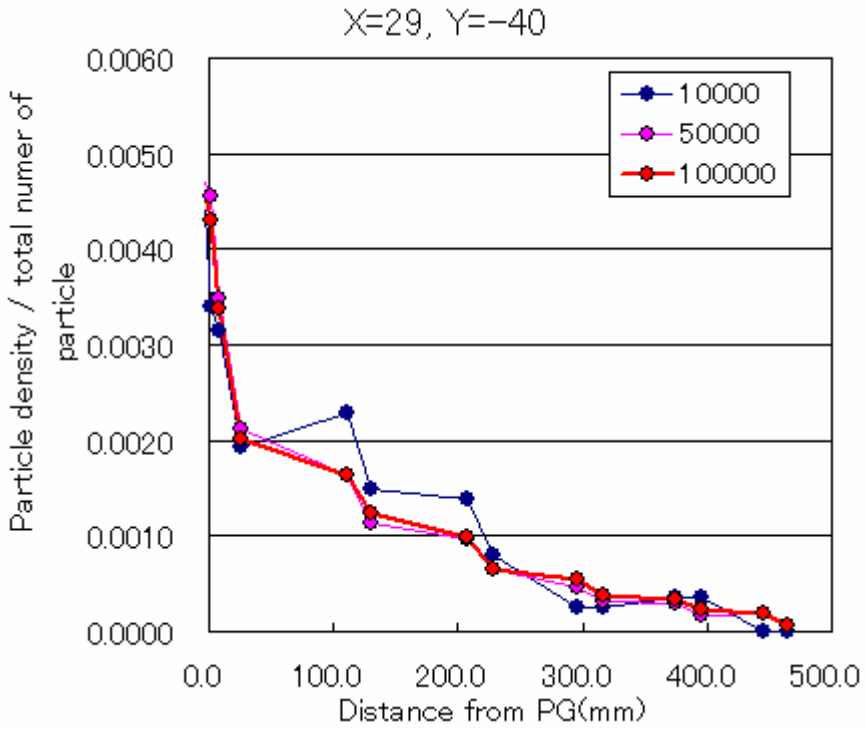

Fig.6.7 Particle profile in 10000, 50000 and 100000 particles.

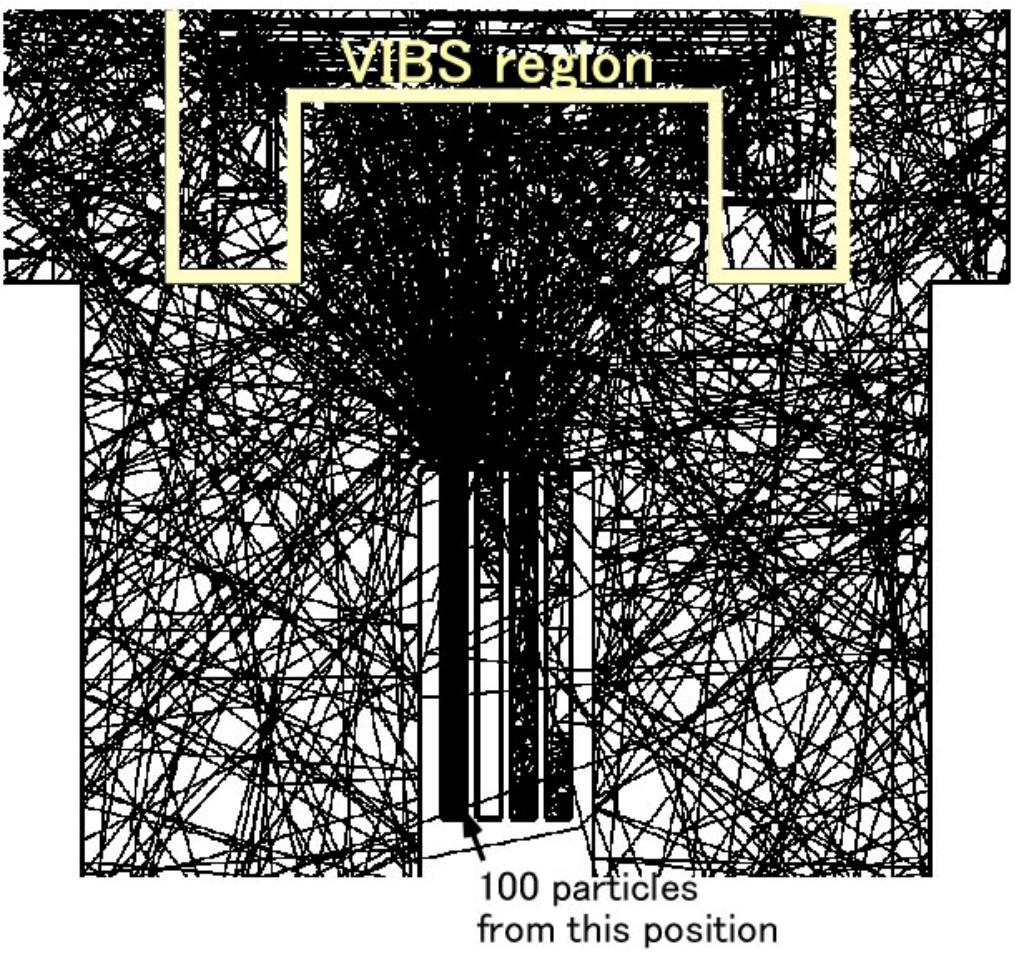

Fig.6.8 Trajectory of gas particle from neutralizer

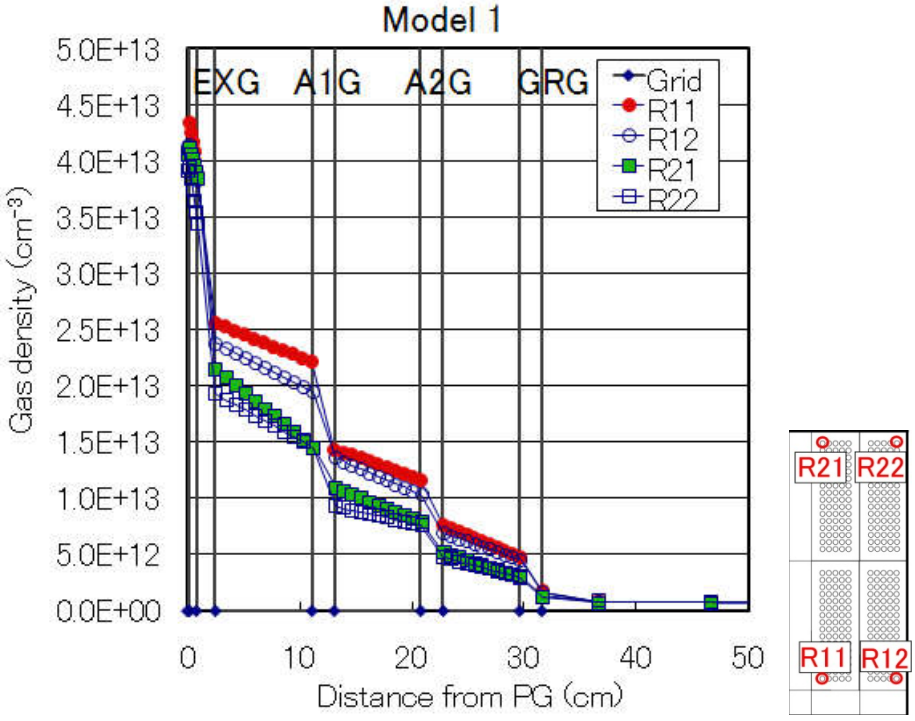

(a)

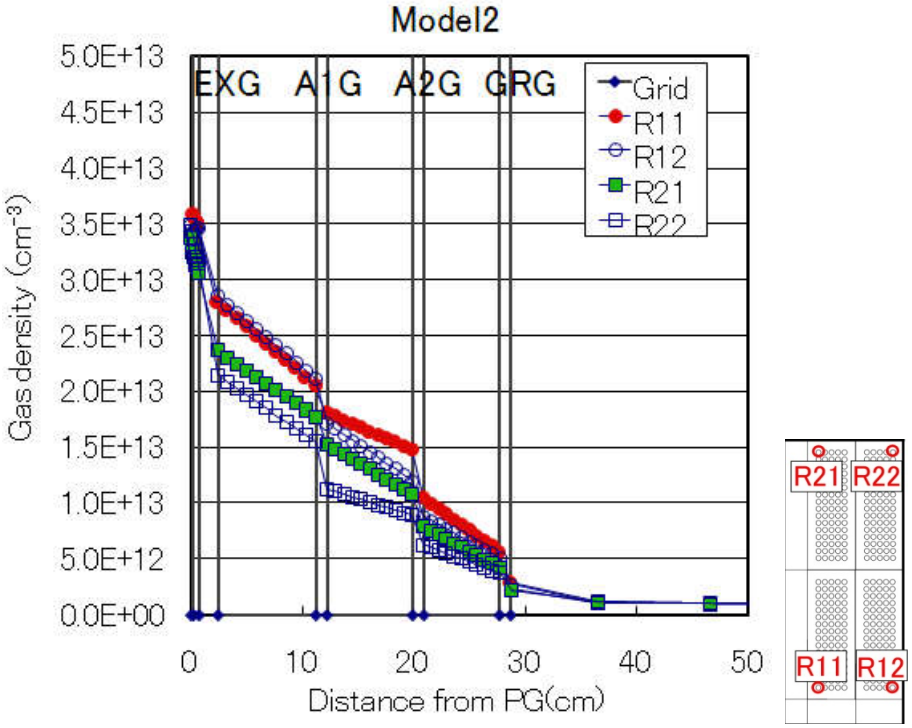

(b)

Fig.6.9 Gas density distribution. In (a)Model 1 and (b) Model 2.

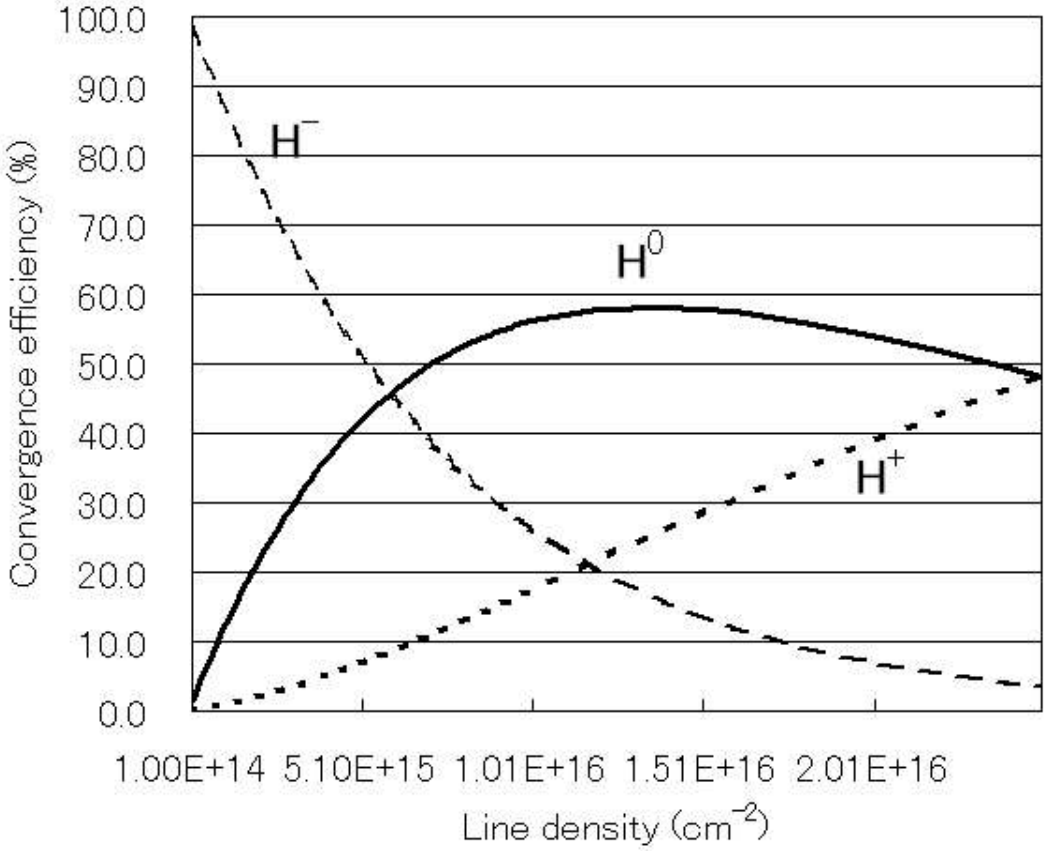

Fig.6.10 Neutralization efficiency of 500 keV H^- ion beam.

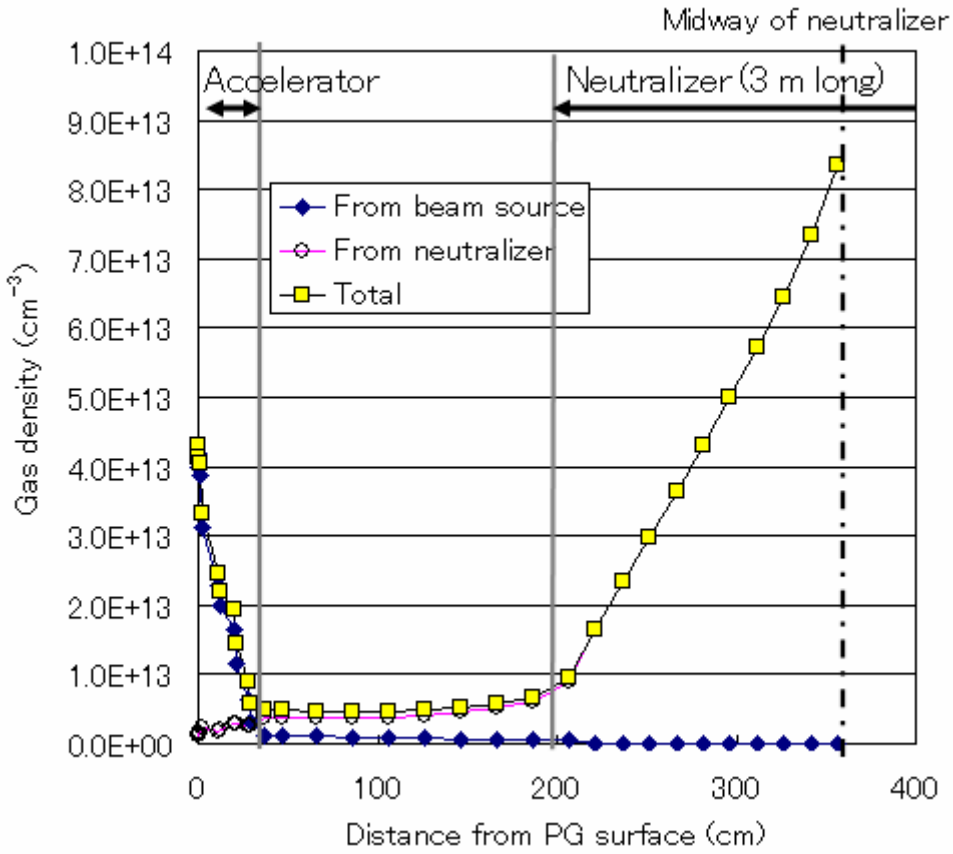

Fig.6.11 Gas density distribution from neutralizer

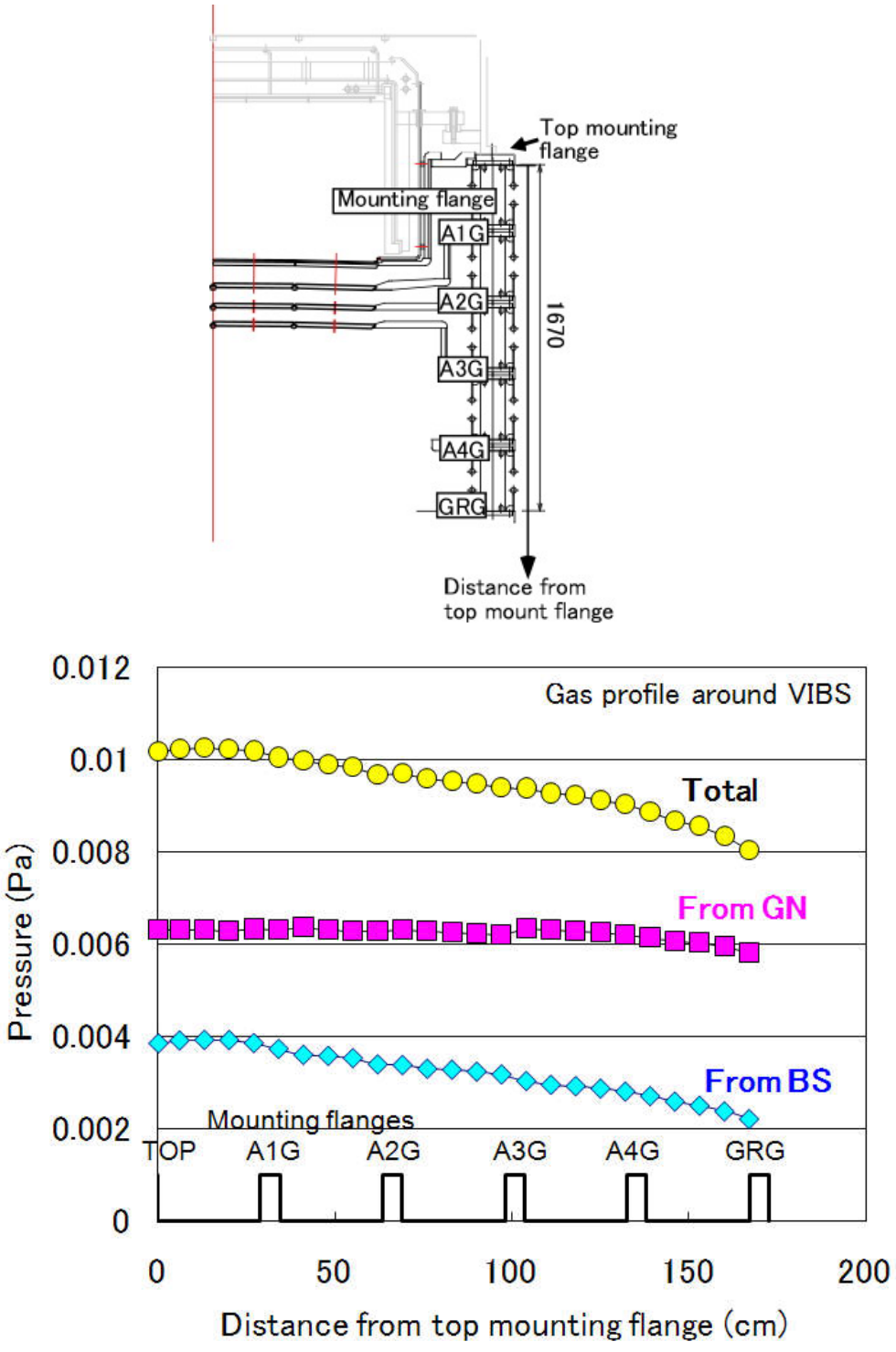

Fig.6.12 Pressure distribution around VIBS

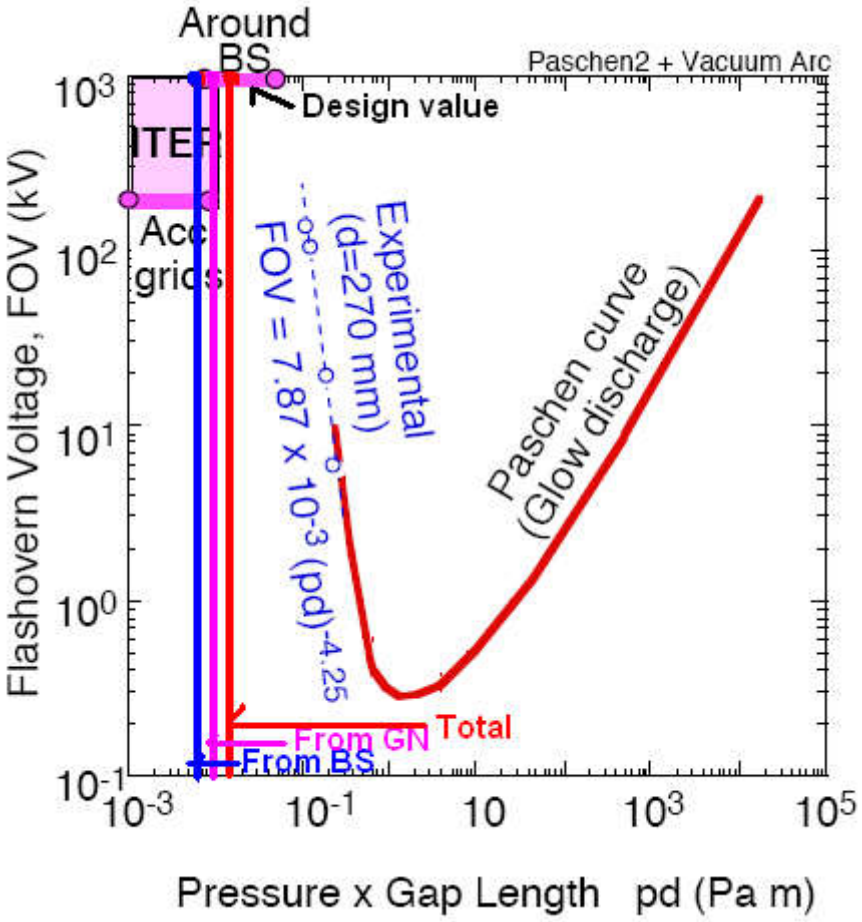

Fig.6.13 Pd around VIBS in Model 2.

Pd (Pa m) of this calculation was added on the figure in Ref.6.6).

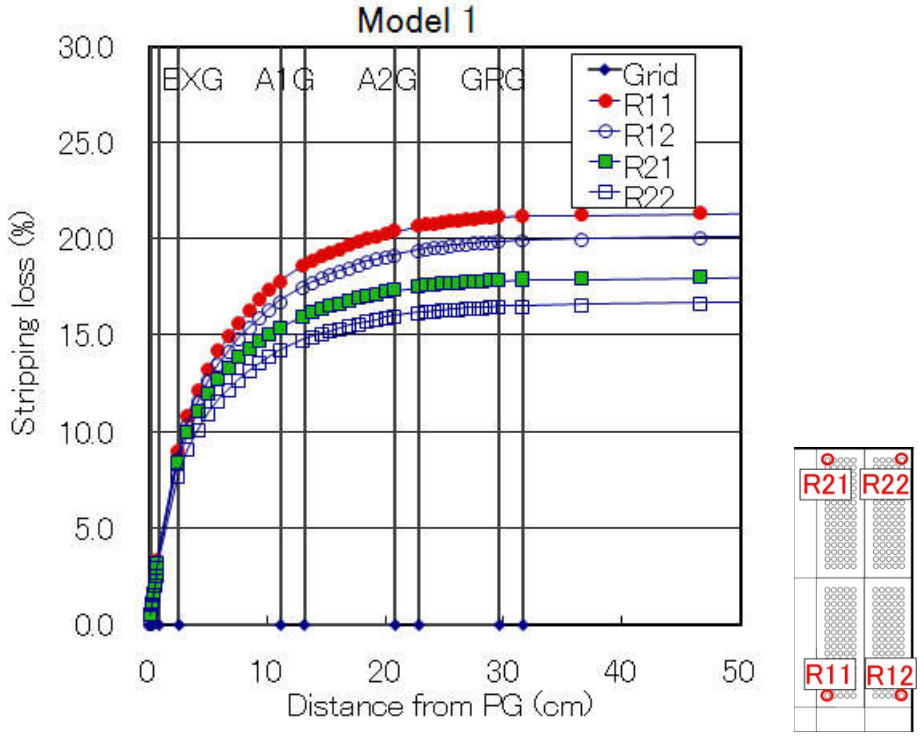

(a)

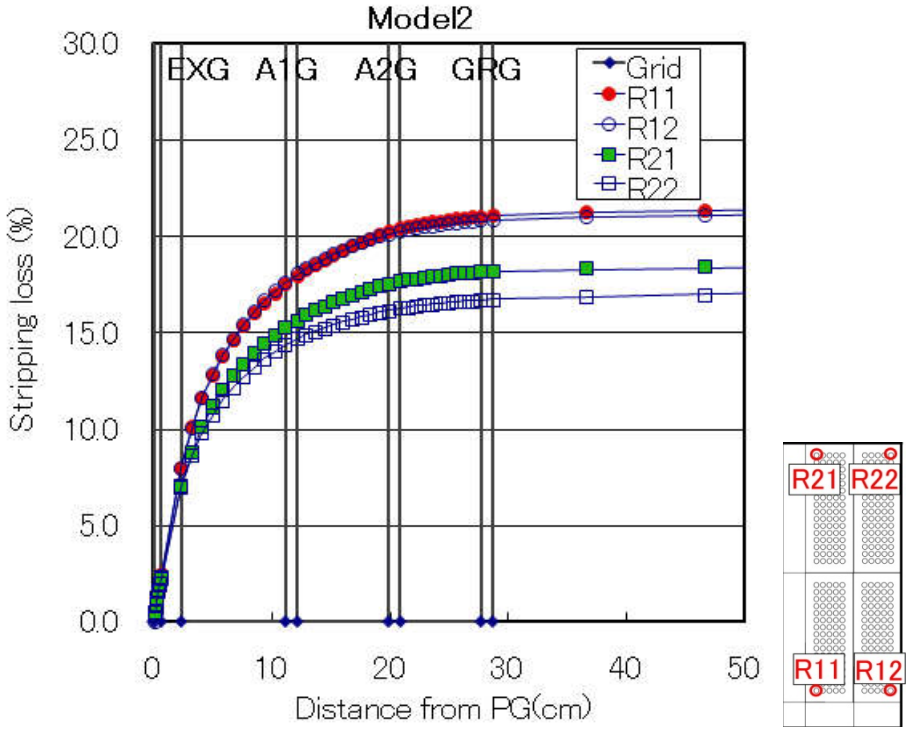

(b)

Fig.6.14. Stripping loss. In (a)Model 1 and (b) Model 2.

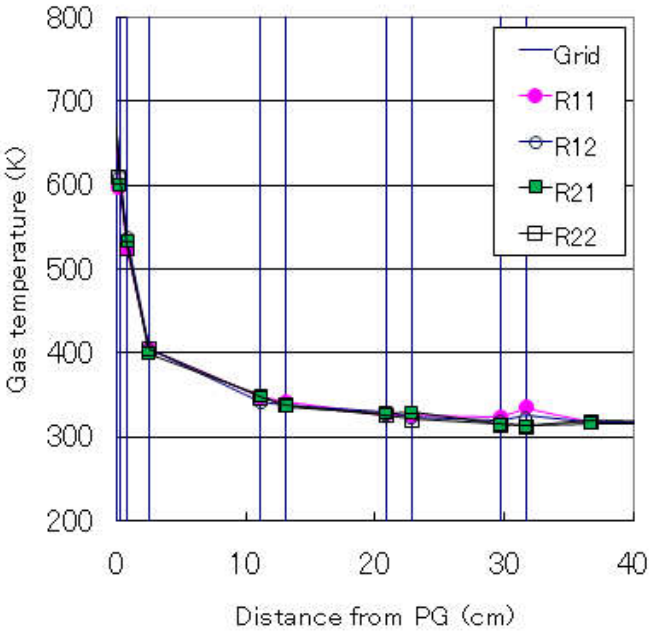

(a)

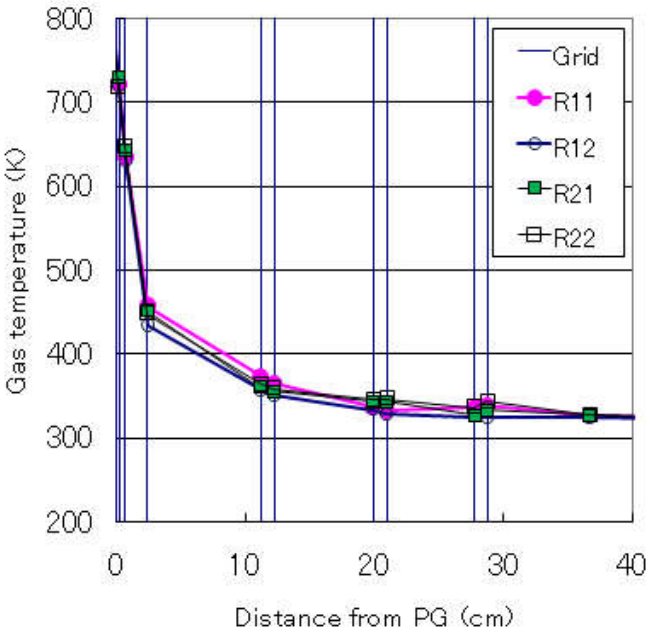

(b)

Fig.6.15. Gas temperature distribution.

In (a)Model 1 and (b) Model 2.

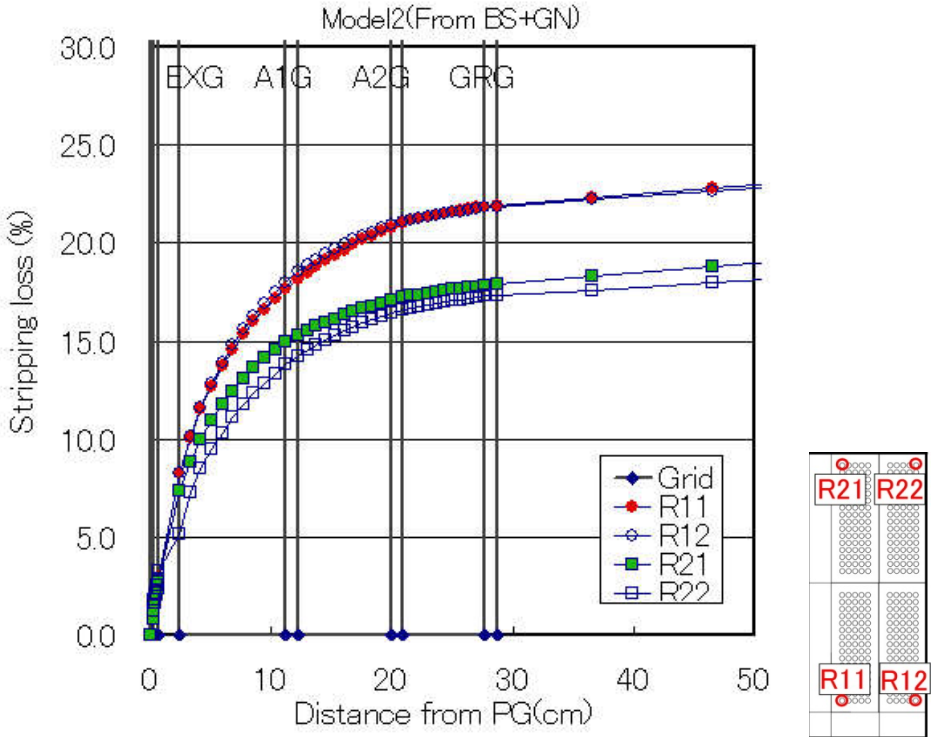

Fig.6.16. Stripping loss when gas is injected from both of beam source and neutralizer.

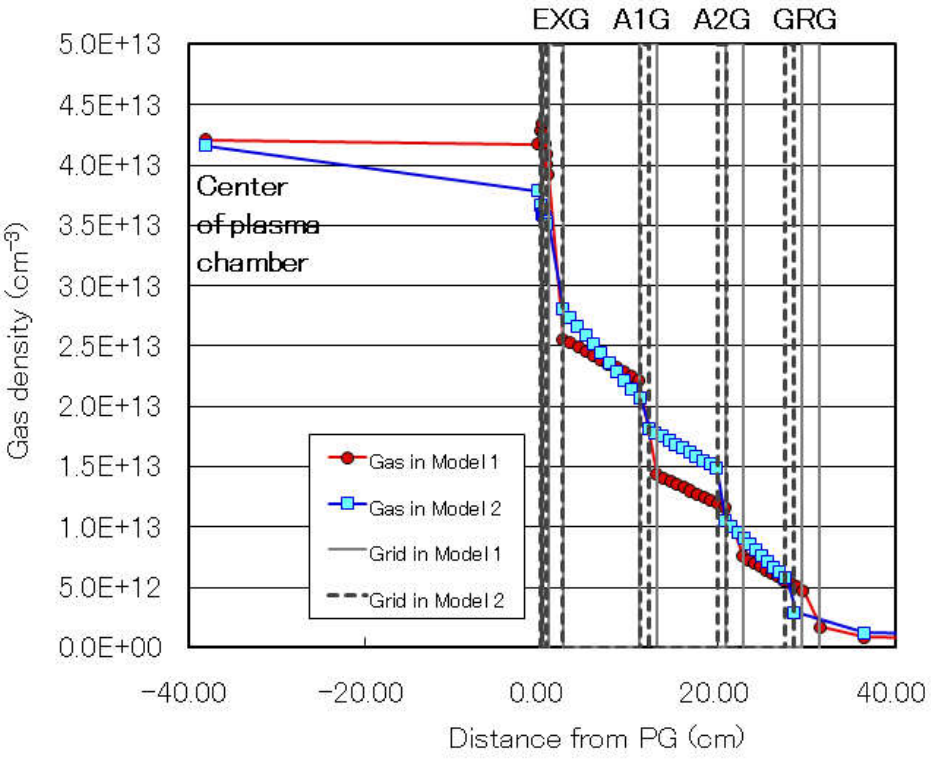

(a)

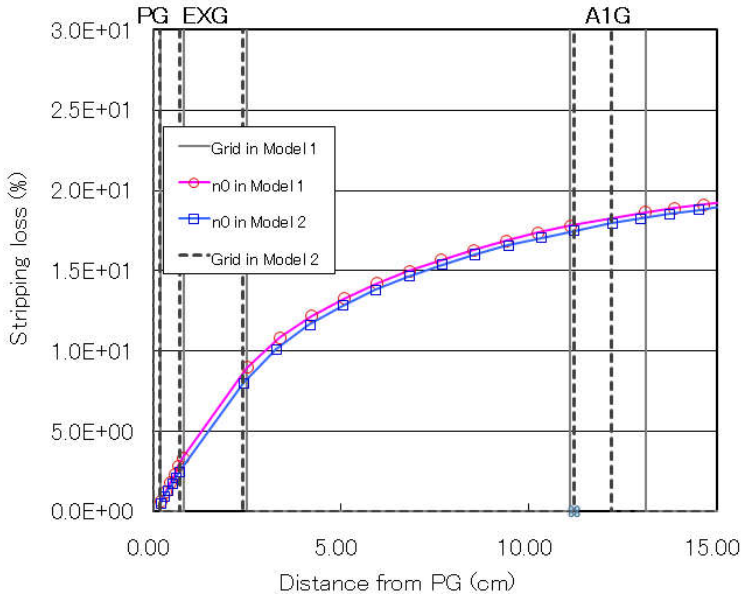

(b)

Fig.6.17 Gas density and stripping loss.

(a) Gas density from plasma discharge chamber to the GRG.

(b) Stripping loss from the PG to the A1G.

7. Summary

The objective of this study is to identify necessary modifications from the original five stage MAMuG accelerator to the 500 keV H^- accelerator through the physics design. In the basic design of the accelerator, the target beam energy and beam current at the emitter were defined as 500 keV and 66 A for H^- ions. The new accelerator structure was proposed from the results of the beam optics analyses utilizing a two dimensional beam analysis code and the stripping loss of negative ions utilizing the JAEA gas flow code. In the three dimensional beam analysis, the ESG with the aperture offset within the displacement distance of 1 mm at the maximum and the kerb to compensate the beamlet deflection and the GRG with the aperture offset for focussing the beamlets were designed. The items for modification are summarized in Table 9-1.

Table 9-1. List of modification items from the five stage MAMuG accelerator to the 500 keV H^- accelerator.

Items	**The original five stage MAMuG accelerator**	**500 keV H^- accelerator**
Number of acceleration grid	Five	Three
Beam energy	1 MeV for D^-, 870 keV for H^-	500 keV
Extraction beam current	59.4 A D^-, 62.8 A H^-	66 A H^-
Beam current density	300 A/m^2 D^-, 320 A/m^2 H^-	335 A/m^2 H^-
Extraction gap distance	6 mm	5 mm
Dim. of extraction grid	11 mm	14 mm
1st accel. gap distance and tolerance	86 mm	88 mm ± 2 mm
2nd accel. gap distance and tolerance	77 mm	77 mm ± 10 mm
3rd accel. gap distance and tolerance	68 mm	68 mm ± 10 mm
Thickness of acceleration grid	20 mm	Acceptable to reduce to 10 mm

Acknowledgments

The authors would like to thank Drs. R. S. Hemsworth in the ITER organization and H. P. L. de Esch in the CEA Cadarache, France for fruitful discussions and comments. They are also express thanks Drs. M. Kamada and M. Hanada in NBI group in JT-60U for their discussion and information. They are grateful to Dr. K. Sakamoto and members of plasma heating technology laboratory for their support and encouragement.

References

2.1) “Neutral beam heating and current drive(H&CD) system”, ITER DDD.5.3.

2.2) “Integrated design of the neutral beam power supply system (IDD)” , 2008. Feb.

3.1) Private communication with Ronald Hemsworth in the ITER organization.

3.2) T. Inoue, M. Hanada, S. Maeno and et al., “Design study of prototype accelerator and MeV test facility for demonstration of 1 MeV, 1 A negative ion beam production”, JAERI-Tech 94-007.

3.3) “Design study of a negative-ion based NBI system for JT-60U”, JAERI-M 94-072.

4.1) Y. Ohara, “Simulation code for beam trajectories in an ion source ‘IONORB’”, JAERI-M 6757, 1976.

4.2) T. Inoue, M. Hanada, Shuichi Maeno and et al., “Design study of prototype accelerator and MeV test Facility for demonstration of 1 MeV, 1 A negative ion beam production”, JAERI-Tech 94-007.

4.3) “Design study of a negative-ion based NBI system for JT-60U”, JAERI-M 94-072.

4.4) “Neutral beam heating and current drive(H&CD) system”, ITER DDD.5.3.

4.5) Y. Okumura, M. Hanada, T. Inoue and et al., “Cesium mixing in the multi-ampere volume H- ion source”, Proceedings of 50th International Symposium, 169-183. Brookhaven, NY, 1990.

4.6) T. Inoue, M. Kashiwagi, M. Taniguchi and et al., “1 MeV, ampere class accelerator R&D for ITER”, Nucl. Fusion 46 (2006) pp.S379-S385.

5.1) N. Umeda et al., “Improvement of beam performance in the negative-ion based NBI system for JT-60U”, Nucl., Fusion 43, pp.522-526 (2003).

5.2) Y. Ikeda et al., “Present status of the negative ion based NBI system for long pulse operation on JT-60U”, Nucl. Fusion 46, pp.S211-S219 (2006).

5.3) M. Kamada et al., “Beamlet deflection due to beamlet-beamlet interaction in a large-area multiaperture negative ion source for JT-60U”, Rev. Sci. Instrum., 79(2008) 02C114—02C113.

5.4) J. H. Whealton, “Linear optics theory of beamlet steering”, Rev. Sci. Instrum., 48(11), pp.1428-1429 (1977).

5.5) W. L. Gardner et al., “Ion beamlet steering by aperture displacement for a tetrode accelerating structure”, Rev. Sci. Instrum., 49-8, pp.1214-1215 (1978).

5.6) Y. Ohara: “Beam Focusing by Aperture Displacement in Two-stage acceleration system”, Japan. J. Appli. Physics., 18-2, pp.351-356 (1979).

5.7) Y. Okumura et al., “Experimental study of ion beamlet steering by aperture displacement in two stage-accelerator”, Rev. Sci. Instrum., 51(4), pp.471-473 (1980).

5.8) T. Inoue, M. Hanada, M. Mizuno and et al., “Steering of H^- beamlet by aperture displacement”, Proceeding of IAEA Technical Committee Meeting on Negative Ion Based Neutral Beam Injectors”, Japan, pp.189-194 (1991), Nov.

5.9) Y. Fujiwara and et al., “Beamlet interaction in multi-aperture negative ion source”, JAERI-Research 99-013(1999).

5.10) Y. Fujiwara and et al., “Beamlet-beamlet interaction in a multi-aperture negative ion source”, Rev. Sci. Instrum., 71 (8), pp. 3059-3064 (2000).

5.11) T. Inoue and et al., “Steering of high energy negative ion beam and design of beam forcing/deflection compensation for JT-60U large negative ion source”, JAERI-Tech 2000-023 (2000).

5.12) T. Inoue et al., “Steering of H^- ion beamlet by aperture displacement”, JAERI-Tech 2000-051 (2000).

5.13) T. Takayanagi et al., “Optimization of negative ion extractor in a JAERI 400 keV H^- ion source”, Rec. Sci. Instrum., 73(2), pp.1061-1063 (2002).

5.14) NBI facility division and NBI heating group, “Design study of a negative-ion Based NBI system for JT-60U”, JAERI-M 94-072 (1994).

5.15) Vector Fields Co. Ltd., http://www.vectorfields.com/.

6.1) Design Description Document 6.3 (DDD 6.3). “NEUTRAL BEAM HEATING & CURRENT DRIVE (NB H&CD) SYSTEM”.

6.2) M. Hanada, M. Kashiwagi, T. Morishita and et al., “Development of negative ion source for the ITER neutral beam injector”, Fusion Eng. and Design 56-57, pp.506-509 (2001).

6.3) https://www.iter.org/cad/53.0004.0010.2D.0400.R --N.FEAT.010526.DLY.EDO.GAS CHANNEL DETAILS HNB NEUTRALISER.

6.4) Y. Okumura, M. Araki, M. Hanada and et al., ”Negative ion based neutral beam injector for JT-60U”, Proceeding of Sixth International Sumposium on the Production and Neutralization of Negative Ions and Beams”, Brookhaven, 1992. Nov.

6.5) Atomic Data for Fusion. Volume 1: Collisions of H, H_2, He, and Li Atoms and Ions with Atoms and Molecules (C. F. Barnett ed.), ORNL-6086 (1990). F-8.

6.6) Atomic Data for Fusion. Volume 1: Collisions of H, H_2, He, and Li Atoms and Ions with Atoms and Molecules (C. F. Barnett ed.), ORNL-6086 (1990). F-10.

6.7) Fig.2.8.2-2 in Ref. 6.1).

(Appendix 1)

Derivation of beamlet steering angle by aperture offset in the ESG in three stage negative ion accelerator

Refer Fig.5-3 in Chapter5.

-- Thin lens theory--

Focal length of beamlet passing though an aperture in one grid is shown as follows according to a thin lens theory.

$$F = \frac{4V_{BE}}{E_2 - E_1} \qquad \text{--- (1)}$$

Here, V_{BE} is a beam energy, and E_1 *and* E_2 are electric field strength before and after the grid.

When the aperture is displaced to δ from the beam axis, steering angle of beamlet θ is,

$$\theta = \frac{\delta}{F}. \text{ --- (2)}$$

-- Steering angle of beamlet in three stage negative ion accelerator --

From eq.(1) and (2), the beamlet steering angle by aperture offset in the ESG is derivate in the three stage accelerator. Each parameters are expressed as follows.

- d_0, d_1, d_2, d_3 : Length of extraction gap, first, second and third acceleration gaps
  V_0, V_1, V_2, V_3 : Applied voltage to extractor, A1G, A2G and GRG.
  Here, acceleration voltage is applied equally to each acceleration grid.
  Then $V_1 = V_2 = V_3 = V_a$.
- E_0, E_1, E_2, E_3 : Electric field strength in extraction, first, second and third acceleration gaps.
  These shows as $\frac{V_0}{d_0} = \frac{V_a}{d_0}$, $\frac{V_1}{d_1} = \frac{V_a}{d_1}$, $\frac{V_2}{d_2} = \frac{V_a}{d_2}$, $\frac{V_3}{d_3} = \frac{V_a}{d_3}$. respectively.
- $V_{B0}, V_{B1}, V_{B2}, V_{B3}$: Beam energy at extractor, A1G, A2G and GRG.
  These are shows as $V_0, V_0, +V_a, V_0, +2V_a, V_0, +3V_a$, respectively.

--- (3)

(I) At ESG

When the aperture offset of δ_0 is applied to the aperture in the ESG, the focal length F_0 and steering angle θ_0 are shown as follows from eq.(1) and (2).

$$F_0 = \frac{4V_{B0}}{E_1} = \frac{4V_0}{\frac{V_a}{d_1}} = 4d_1\frac{V_0}{V_a} = 4d_1\alpha \quad \text{--- (4)}$$

$$\theta_0 = \frac{\delta_0}{F_0} = \frac{\delta_0}{4d_1\alpha} = c_0\delta_0 \circ \quad \text{--- (5)}$$

$$\text{Here, } \frac{V_0}{V_a} = \alpha \quad \text{--- (6).}$$

(II) At A1G

The steering angle caused in the ESG aperture offset θ_0 is changed to θ_{10} at the A1G due to the increase of beam energy between the ESG and the A1G.

$$\theta_{10} = \left(\frac{V_{B0}}{V_{B1}}\right)^{1/2}\theta_0 \quad \text{--- (7)}$$

The geometrical aperture offsets are not applied to the A1G, A2G and GRG. However substantial aperture offsets are occurred because the beamlet axis is displaced from the aperture axis due to the deflection by the aperture offset in the ESG. Then steering angle θ_{11} due to this substantial aperture offset δ_1 in the A1G is expressed as follows.

$$\theta_{11} = \frac{\delta_1}{F_1}$$

Here,

$$\delta_1 = -\upsilon_0\theta_0 \cdot \Delta t_{ESG-A1G}$$
$$= -2\frac{(V_{B0}V_{B1})^{1/2} - V_{B0}}{V_{B1}}\theta_0 \cdot$$
$$F_1 = \frac{4V_{B1}}{E_2 - E_1}$$

Then total steering angle at A1G θ_1 is,

$$\therefore \theta_1 = \theta_{10} + \theta_{11}$$
$$= \left[\left(\frac{V_{B0}}{V_{B1}}\right)^{1/2} - \frac{2(E_2 - E_1)\left\{(V_{BO}\cdot V_{B1})^{1/2} - V_{B0}\right\}}{4E_1V_{B1}}\right]\times\theta_0 \cdot$$

From eq.(3)(6),

$$\theta_1 = \left[\left(\frac{V_0}{V_0 + Va}\right)^{1/2} - \frac{2\left(\frac{V_a}{d_2} - \frac{V_a}{d_1}\right)\left\{V_0^{1/2}\cdot(V_0 + V_a)^{1/2} - V_0\right\}}{4\frac{V_a}{d_1}(V_0 + V_a)}\right]\times\theta_0$$

$$= \left[\left(\frac{\alpha}{\alpha+1} \right)^{1/2} - \frac{1}{2} \cdot \frac{d_1 - d_2}{d_2} \cdot \frac{\left\{ \alpha^{1/2} \cdot (\alpha+1)^{1/2} - \alpha \right\}}{\alpha+1} \right] \theta_0 . \quad \text{--- (8)}$$

$$= C_1 \theta_0 \quad \text{--- (9)}$$

(III) At A2G

As same as (II) , the steering angle at A1G θ_1 is varied to θ_{20} at the A2G due to the increase of beam energy.

$$\theta_{20} = \left(\frac{V_{B1}}{V_{B2}} \right)^{1/2} \theta_1$$

The steering angle θ_{21} by substantial aperture offset δ_2 is expressed as follows.

$$\theta_{21} = \frac{\delta_2}{F_2}$$

Here,

$$\delta_2 = -\upsilon_1 \cdot \theta_1 \cdot \Delta t_{A1a-A2a}$$

$$= -2 \frac{\left(V_{B1} \cdot V_{B2} \right)^{1/2} - V_{B1}}{E_2} \cdot \theta_1 .$$

$$F = \frac{4 V_{B2}}{E_3 - E_2}$$

Then, the steering angle at A2G θ_2 is as follows.

$$\therefore \theta_2 = \theta_{20} + \theta_{21}$$

$$= \left[\left(\frac{V_{B1}}{V_{B2}} \right)^{1/2} - \frac{2(E_3 - E_2)\left\{ \left(V_{B1} \cdot V_{B2} \right)^{1/2} - V_{B1} \right\}}{4 E_2 V_{B2}} \right] \theta_1$$

$$= \left[\left(\frac{\alpha+1}{\alpha+2} \right)^{1/2} - \frac{2\left(\frac{V_a}{d_3} - \frac{V_a}{d_2} \right)\left\{ \left(V_0 + V_a \right)^{1/2} \left(V_0 + 2V_a \right)^{1/2} - \left(V_0 + V_a \right) \right\}}{4 \frac{V_a}{d_2} \left(V_0 + 2V_a \right)} \right] \theta_1$$

$$= \left[\left(\frac{\alpha+1}{\alpha+2} \right)^{1/2} - \frac{1}{2} \frac{d_2 - d_3}{d_3} \cdot \frac{\left\{ (\alpha+1)^{1/2} (\alpha+2)^{1/2} - (\alpha+1) \right\}}{\alpha+2} \right] \theta_1 \quad \text{--- (10)}$$

$$= C_2 \theta_1 \quad \text{--- (11)}$$

(IV)

As same as (II), t the steering angle at A1G θ_2 is varied to θ_{30} at the A23 due to the increase of beam energy.

$$\theta_{30} = \left(\frac{V_{B2}}{V_{B3}} \right)^{1/2} \theta_2$$

The steering angle θ_{31} by substantial aperture offset δ_3 is expressed as follows.

$$\theta_{31} = \frac{\delta_3}{F_3}$$

Here,

$$\begin{aligned} \delta_3 &= -\upsilon_1 \theta_2 \cdot \Delta t_{A2a \to A3a} \\ &= -2 \frac{\left(V_{B2} \cdot V_{B3} \right)^{1/2} - V_{B2}}{E_3} \theta_2 \end{aligned}$$

$$F_3 = -\frac{4V_{B3}}{E_3}$$

Then, the steering angle at GRG θ_3 is as follows.

$$\begin{aligned} \theta_3 &= \theta_{30} + \theta_{31} \\ &= \theta_{30} + \frac{\delta_3}{F_3} \end{aligned}$$

$$\theta_3 = \left[\left(\frac{V_{B2}}{V_{B3}} \right)^{1/2} + \frac{2E_3 \left\{ \left(V_{B2} \cdot V_{B3} \right)^{1/2} - V_{B2} \right\}}{4E_2 V_{B3}} \right] \theta_2$$

$$= \left[\left(\frac{\alpha + 2}{\alpha + 3} \right)^{1/2} + \frac{1}{2} \frac{\left(\alpha + 2 \right)^{1/2} \left(\alpha + 3 \right)^{1/2} - \left(\alpha + 2 \right)}{\alpha + 3} \right] \theta_3 \quad \text{--- (12)}$$

$$\theta_3 \quad = C_3 \theta_2 \quad \text{--- (13)}$$

Then, From Eqs. (5)(9)(11)(13),

$$\begin{aligned} \therefore \theta_3 &= C_0 \cdot C_1 \cdot C_2 \cdot C_3 \cdot \delta_0 \\ &= C(\alpha) \cdot \delta_0 \end{aligned} \quad \text{. --- (14)}$$

Here, $\alpha = \frac{V_0}{V_a}$ and V_a is 1/3 of acceleration voltage. α is the ratio of extraction voltage and acceleration voltage.

Finally, Each coefficients are shown as follows from Eqs.(4)(8)(10)(12).

$$C_0 = \frac{1}{4d_1 \alpha}$$

$$C_1 = \left[\left(\frac{\alpha}{\alpha+1} \right)^{1/2} - \frac{1}{2} \cdot \frac{d_1 - d_2}{d_2} \cdot \frac{\left\{ \alpha^{1/2} \cdot (\alpha+1)^{1/2} - \alpha \right\}}{\alpha+1} \right]$$

$$C_2 = \left[\left(\frac{\alpha+1}{\alpha+2} \right)^{1/2} - \frac{1}{2} \frac{d_2 - d_3}{d_3} \cdot \frac{\left\{ (\alpha+1)^{1/2} (\alpha+2)^{1/2} - (\alpha+1) \right\}}{\alpha+2} \right]$$

$$C_3 = \left[\left(\frac{\alpha+2}{\alpha+3} \right)^{1/2} + \frac{1}{2} \frac{(\alpha+2)^{1/2} (\alpha+3)^{1/2} - (\alpha+2)}{\alpha+3} \right]$$

Steering angle in the accelerator exit θ_3 is independent to the beam energy when the ratio of extraction and acceleration voltage is maintained.

国際単位系（SI）

表１．SI 基本単位

基本量	SI 基本単位	
	名称	記号
長さ	メートル	m
質量	キログラム	kg
時間	秒	s
電流	アンペア	A
熱力学温度	ケルビン	K
物質量	モル	mol
光度	カンデラ	cd

表２．基本単位を用いて表されるSI組立単位の例

組立量	SI 基本単位	
	名称	記号
面積	平方メートル	m^2
体積	立法メートル	m^3
速さ，速度	メートル毎秒	m/s
加速度	メートル毎秒毎秒	m/s^2
波数	毎メートル	m^{-1}
密度，質量密度	キログラム毎立方メートル	kg/m^3
面積密度	キログラム毎平方メートル	kg/m^2
比体積	立方メートル毎キログラム	m^3/kg
電流密度	アンペア毎平方メートル	A/m^2
磁界の強さ	アンペア毎メートル	A/m
量濃度(a)，濃度	モル毎立方メートル	mol/m^3
質量濃度	キログラム毎立法メートル	kg/m^3
輝度	カンデラ毎平方メートル	cd/m^2
屈折率(b)	（数字の） 1	1
比透磁率(b)	（数字の） 1	1

(a) 量濃度（amount concentration）は臨床化学の分野では物質濃度（substance concentration）ともよばれる。
(b) これらは無次元量あるいは次元１をもつ量であるが、そのことを表す単位記号である数字の１は通常は表記しない。

表３．固有の名称と記号で表されるSI組立単位

組立量	SI 組立単位			
	名称	記号	他のSI単位による表し方	SI基本単位による表し方
平面角	ラジアン(b)	rad	1(b)	m/m
立体角	ステラジアン(b)	sr(c)	1(b)	m^2/m^2
周波数	ヘルツ(d)	Hz		s^{-1}
力	ニュートン	N		m kg s^{-2}
圧力，応力	パスカル	Pa	N/m^2	m^{-1} kg s^{-2}
エネルギー，仕事，熱量	ジュール	J	N m	m^2 kg s^{-2}
仕事率，工率，放射束	ワット	W	J/s	m^2 kg s^{-3}
電荷，電気量	クーロン	C		s A
電位差（電圧），起電力	ボルト	V	W/A	m^2 kg s^{-3} A^{-1}
静電容量	ファラド	F	C/V	m^{-2} kg^{-1} s^4 A^2
電気抵抗	オーム	Ω	V/A	m^2 kg s^{-3} A^{-2}
コンダクタンス	ジーメンス	S	A/V	m^{-2} kg^{-1} s^3 A^2
磁束	ウエーバ	Wb	Vs	m^2 kg s^{-2} A^{-1}
磁束密度	テスラ	T	Wb/m^2	kg s^{-2} A^{-1}
インダクタンス	ヘンリー	H	Wb/A	m^2 kg s^{-2} A^{-2}
セルシウス温度	セルシウス度(e)	℃		K
光束	ルーメン	lm	cd sr(c)	cd
照度	ルクス	lx	lm/m^2	m^{-2} cd
放射性核種の放射能（f）	ベクレル(d)	Bq		s^{-1}
吸収線量，比エネルギー分与，カーマ	グレイ	Gy	J/kg	m^2 s^{-2}
線量当量，周辺線量当量，方向性線量当量，個人線量当量	シーベルト(g)	Sv	J/kg	m^2 s^{-2}
酸素活性	カタール	kat		s^{-1} mol

(a)SI接頭語は固有の名称と記号を持つ組立単位と組み合わせても使用できる。しかし接頭語を付した単位はもはやコヒーレントではない。
(b)ラジアンとステラジアンは数字の１に対する単位の特別な名称で、量についての情報をつたえるために使われる。実際には、使用する時には記号radおよびsrが用いられるが、習慣として組立単位としての記号である数字の１は明示されない。
(c)測光学ではステラジアンという名称と記号srを単位の表し方の中に、そのまま維持している。
(d)ヘルツは周期現象についてのみ、ベクレルは放射性核種の統計的過程についてのみ使用される。
(e)セルシウス度はケルビンの特別な名称で、セルシウス温度を表すために使用される。セルシウス度とケルビンの単位の大きさは同一である。したがって、温度差や温度間隔を表す数値はどちらの単位で表しても同じである。
(f)放射性核種の放射能（activity referred to a radionuclide）は、しばしば誤った用語で"radioactivity"と記される。
(g)単位シーベルト（PV,2002,70,205）についてはCIPM勧告2（CI-2002）を参照。

表４．単位の中に固有の名称と記号を含むSI組立単位の例

組立量	SI 組立単位		
	名称	記号	SI 基本単位による表し方
粘度	パスカル秒	Pa s	m^{-1} kg s^{-1}
力のモーメント	ニュートンメートル	N m	m^2 kg s^{-2}
表面張力	ニュートン毎メートル	N/m	kg s^{-2}
角速度	ラジアン毎秒	rad/s	m m^{-1} s^{-1}=s^{-1}
角加速度	ラジアン毎秒毎秒	rad/s^2	m m^{-1} s^{-2}=s^{-2}
熱流密度，放射照度	ワット毎平方メートル	W/m^2	kg s^{-3}
熱容量，エントロピー	ジュール毎ケルビン	J/K	m^2 kg s^{-2} K^{-1}
比熱容量，比エントロピー	ジュール毎キログラム毎ケルビン	J/(kg K)	m^2 s^{-2} K^{-1}
比エネルギー	ジュール毎キログラム	J/kg	m^2 s^{-2}
熱伝導率	ワット毎メートル毎ケルビン	W/(m K)	m kg s^{-3} K^{-1}
体積エネルギー	ジュール毎立方メートル	J/m^3	m^{-1} kg s^{-2}
電界の強さ	ボルト毎メートル	V/m	m kg s^{-3} A^{-1}
電荷密度	クーロン毎立方メートル	C/m^3	m^{-3} sA
表面電荷	クーロン毎平方メートル	C/m^2	m^{-2} sA
電束密度，電気変位	クーロン毎平方メートル	C/m^2	m^{-2} sA
誘電率	ファラド毎メートル	F/m	m^{-3} kg^{-1} s^4 A^2
透磁率	ヘンリー毎メートル	H/m	m kg s^{-2} A^{-2}
モルエネルギー	ジュール毎モル	J/mol	m^2 kg s^{-2} mol^{-1}
モルエントロピー，モル熱容量	ジュール毎モル毎ケルビン	J/(mol K)	m^2 kg s^{-2} K^{-1} mol^{-1}
照射線量（X線及びγ線）	クーロン毎キログラム	C/kg	kg^{-1} sA
吸収線量率	グレイ毎秒	Gy/s	m^2 s^{-3}
放射強度	ワット毎ステラジアン	W/sr	m^4 m^{-2} kg s^{-3}=m^2 kg s^{-3}
放射輝度	ワット毎平方メートル毎ステラジアン	$W/(m^2 sr)$	m^2 m^{-2} kg s^{-3}=kg s^{-3}
酵素活性濃度	カタール毎立方メートル	kat/m^3	m^{-3} s^{-1} mol

表５．SI 接頭語

乗数	接頭語	記号	乗数	接頭語	記号
10^{24}	ヨタ	Y	10^{-1}	デシ	d
10^{21}	ゼタ	Z	10^{-2}	センチ	c
10^{18}	エクサ	E	10^{-3}	ミリ	m
10^{15}	ペタ	P	10^{-6}	マイクロ	μ
10^{12}	テラ	T	10^{-9}	ナノ	n
10^{9}	ギガ	G	10^{-12}	ピコ	p
10^{6}	メガ	M	10^{-15}	フェムト	f
10^{3}	キロ	k	10^{-18}	アト	a
10^{2}	ヘクト	h	10^{-21}	ゼプト	z
10^{1}	デカ	da	10^{-24}	ヨクト	y

表６．SIに属さないが、SIと併用される単位

名称	記号	SI 単位による値
分	min	1 min=60s
時	h	1h =60 min=3600 s
日	d	1 d=24 h=86 400 s
度	°	1°=(π/180) rad
分	’	1’=(1/60)°=(π/10800) rad
秒	”	1”=(1/60)’=(π/648000) rad
ヘクタール	ha	$1ha=1hm^2=10^4m^2$
リットル	L，l	$1L=11=1dm^3=10^3cm^3=10^{-3}m^3$
トン	t	$1t=10^3$ kg

表７．SIに属さないが、SIと併用される単位で、SI単位で表される数値が実験的に得られるもの

名称	記号	SI 単位で表される数値
電子ボルト	eV	$1eV=1.602\ 176\ 53(14)\times10^{-19}J$
ダルトン	Da	$1Da=1.660\ 538\ 86(28)\times10^{-27}kg$
統一原子質量単位	u	1u=1 Da
天文単位	ua	$1ua=1.495\ 978\ 706\ 91(6)\times10^{11}m$

表８．SIに属さないが、SIと併用されるその他の単位

名称	記号	SI 単位で表される数値
バール	bar	1 bar=0.1MPa=100kPa=10^5Pa
水銀柱ミリメートル	mmHg	1mmHg=133.322Pa
オングストローム	Å	1 Å=0.1nm=100pm=10^{-10}m
海里	M	1 M=1852m
バーン	b	$1\ b=100fm^2=(10^{-12}cm)2=10^{-28}m^2$
ノット	kn	1 kn=(1852/3600)m/s
ネーパ	Np	SI単位との数値的な関係は、対数量の定義に依存。
ベル	B	
デジベル	dB	

表９．固有の名称をもつCGS組立単位

名称	記号	SI 単位で表される数値
エルグ	erg	$1\ erg=10^{-7}$ J
ダイン	dyn	$1\ dyn=10^{-5}$N
ポアズ	P	$1\ P=1\ dyn\ s\ cm^{-2}=0.1Pa\ s$
ストークス	St	$1\ St=1cm^2\ s^{-1}=10^{-4}m^2\ s^{-1}$
スチルブ	sb	$1\ sb=1cd\ cm^{-2}=10^4cd\ m^{-2}$
フォト	ph	$1\ ph=1cd\ sr\ cm^{-2}\ 10^4lx$
ガル	Gal	$1\ Gal=1cm\ s^{-2}=10^{-2}ms^{-2}$
マクスウェル	Mx	$1\ Mx = 1G\ cm^2=10^{-8}Wb$
ガウス	G	$1\ G=1Mx\ cm^{-2}=10^{-4}T$
エルステッド（c）	Oe	1 Oe ≙ $(10^3/4\pi)A\ m^{-1}$

(c) ３元系のCGS単位系とSIでは直接比較できないため、等号「 ≙ 」は対応関係を示すものである。

表10．SIに属さないその他の単位の例

名称	記号	SI 単位で表される数値
キュリー	Ci	$1\ Ci=3.7\times10^{10}Bq$
レントゲン	R	$1\ R = 2.58\times10^{-4}C/kg$
ラド	rad	$1\ rad=1cGy=10^{-2}Gy$
レム	rem	$1\ rem=1\ cSv=10^{-2}Sv$
ガンマ	γ	1γ=1 nT=10-9T
フェルミ		1フェルミ=1 fm=10-15m
メートル系カラット		1メートル系カラット = 200 mg = 2×10-4kg
トル	Torr	1 Torr = (101 325/760) Pa
標準大気圧	atm	1 atm = 101 325 Pa
カロリー	cal	1cal=4.1858J（「15℃」カロリー），4.1868J（「IT」カロリー）4.184J（「熱化学」カロリー）
ミクロン	μ	1 μ =1μm=10^{-6}m

（第8版，2006年改訂）